Swansea University
Prifysgol Abertawe

Production and Electron Microscopy Investigations of Nanoscale Structures

Sean Lethbridge, MEng

Submitted to Swansea University in fulfilment
of the requirements for the Degree of

Doctor of Philosophy

Swansea University

October 2025

To my loving Dad

I. ABSTRACT

Nanotechnology is at the forefront of modern day lives with applications in a variety of different technological and industrial sectors through its many forms. The central drive behind this is the need for continued improvement and to do more with less. This can be achieved through the use of a variety of nanoscale materials and structures specific to the end usage requirements. In order to match these materials and structures with the suitable applications such as catalysis and electronics however, it is necessary to first understand them and how they work. As a result, scientific research is constantly needing to be carried out to provide this understanding through continuous experimentation and analysis. It is the objective of this work to contribute to this continued research by presenting new discoveries and publishing key findings.

Here research has been carried out on two types of nanomaterial; Multi-Walled Carbon Nanotubes, and Nanoclusters, where analysis is focused on the resulting sizes and structures of these nanomaterials and the discovery patterns between synthesis conditions and end results. To achieve this, TEM/STEM imaging was carried out on these materials and data was analysed using image processing software to ascertain the various sizes and structural characteristics of these nanomaterials. Carbon nanotube investigations included both surface and core structure analysis whilst, nanocluster analysis reviewed the atomic sizes, as well as isomeric structure, and quasi-shape of both Silver and Gold nanostructures. In carbon nanotube investigations, HRTEM investigations successfully showed grown carbon nanotubes from Polystyrene. It was further discovered how the concentration of Polystyrene affects the surface characteristics, in particular the uniformity, in addition to the core structural traits. Silver nanocluster analysis revealed how the synthesis conditions affected the overall sizes of Matrix Assembly grown nanoclusters whilst, it was discovered how post-production exposure to atmosphere influenced the nanoclusters isomeric structure through contaminants exposure. Similarly, Gold nanocluster investigations demonstrated how the sputtering conditions reflected on the size ranges of surface aggregation grown nanoclusters, and potentially influenced the end isomeric structure of the nanoclusters. Additionally, quasi-geometry analysis of Gold nanoclusters revealed a mix of both 3D and 2D structures, where 3D geometries were seen to vary between 3 quasi-geometries. Previously unknown ‘2D rafts’ were also discovered where structures up to 100 atoms in size were analysed to understand the nature of formation of this newly discovered structure. The results presented here offered further insight into both existing and novel nanostructures, and the relationship they have to the corresponding synthesis conditions. Such findings are important for not only the continued understanding of existing nanostructures, but also the discovery and development of new nanostructures with new potential applications. Furthermore, we report on the regeneration and recommissioning of a Caesium Sputtering Negative Ion Cluster Source as a new cluster beam deposition platform. Mass and Cluster spectra were carried out to understand the performance of the cluster source, and demonstrate its potential as an apparatus for the deposition and future study of few atom nanoclusters.

II. AUTHOR'S DECLARATION

This work has not previously been accepted in substance for any degree and is not being concurrently submitted in candidature for any degree.

Signed: [redacted]

Date: 17/10/2025

This thesis is the result of my own investigations, except where otherwise stated. Other sources are acknowledged by footnotes giving explicit references. A bibliography is appended.

Signed: [redacted]

Date: 17/10/2025

I hereby give consent for my thesis, if accepted, to be available for electronic sharing.

Signed: [redacted]

Date: 17/10/2025

The University's ethical procedures have been followed and, where appropriate, that ethical approval has been granted.

Signed: [redacted]

Date: 17/10/2025

Table of Contents

III. ACKNOWLEDGEMENTS

I would first like to thank Professor Richard Palmer, for not only giving me the opportunity but continuously supporting me throughout this thesis. Without his invaluable guidance and advice, I doubt I would have been this successful over the past four and a half years.

I would also like to convey my gratitude to Dr Yubiao Niu who provided invaluable support and essential training on the Transmission Electron Microscope, as well as Dr Thomas Slater at Diamond Light Source/Cardiff University for his mentoring and guidance in the nanocluster analysis portion of this thesis. Without their guidance, certain parts of this thesis would have been impossible.

Additionally, I would like to thank; Ali Hedayati, Jainaba Sallah-Conteh, Erica Watchrorn-Rokutan, and Dr James McCormack for providing their samples for analysis in this thesis, thus making this PhD possible.

Penultimately, I would like to thank Professor Richard Palmer, and the Nanomaterials Lab research group as well as, Professor Alvin Orbaek-White for their assistance in reviewing this thesis prior to submission. Their detailed feedback here has been invaluable during this stage of my thesis writing.

Finally, I would like to thank my family at home, and in particular my Dad, who have provided continuous emotional stability and the strength to complete this thesis.

Thank you to all, your support has allowed me to get through the good times and the bad.

IV. LIST OF PAPERS

PAPER I
Published
Orbaek White, A.; He- dayati, A.; Yick, T.; Gangoli, V.S.; Niu, Y.; Lethbridge, S.; Tsampanakis, I.; Swan, G.; Pointeaux, L.; Crane, A.; Charles, R.; Sallah-Conteh, J.; Anderson, A. O.; Lloyd Davies, M.; Corr, S. J.; Palmer, R. E. On the Use of Carbon Cables from Plastic Solvent Combinations of Polystyrene and Toluene in Carbon Nanotube Synthesis. Nanomaterials 2022, 12, 9. DOI: 10.3390/nano12010009

PAPER II
Published
Vernieres, J.; Tarrat, N.; Lethbridge, S.; Watchorn-Rokutan, E.; Slater, T. J. A.; Loffreda, D.; Palmer, R. E. Influence of air exposure on structural isomers of silver nanoparticles. Commun Chem 6, 19 (2023). DOI: 10.1038/s42004-023-00813-9

PAPER III
Published
Dearg, M.; Lethbridge, S.; McCormack, J.; Cobley, R. J.; Palmer, R. E.; Slater, T. J. A. Characterization of the Morphology of Surface-Assembled Au Nanoclusters on Amorphous Carbon. Nanoscale, 2024, 16, 10827. DOI: 10.1039/D4NR00978A

PAPER IV
Published
Lethbridge, S.; Pavloudis, Th.; McCormack, J.; Slater, T. J. A.; Kioseoglou, J.; Palmer, R. E. Stabilization of 2D Raft Structures of Au Nanoclusters with up to 60 Atoms by a Carbon Support. Small Sci, 2024, 2400093. DOI: 10.1002/smsc.202400093

V. LIST OF FIGURES AND TABLES

VI. UNITS AND ABBREVIATIONS

Å	Angstrom
eV	Electron-Volt
kV	Kilovolt
kx	Thousand-times Magnification
Mx	Million-times Magnification
nA	Nanoampere
nm	Nanometre
pm	Picometre
px	Pixel
µA	Microampere
µm	Micrometre

2D/3D	2/3 Dimensional
AC-STEM	Aberration Corrected Scanning Transmission Electron Microscopy
ADF	Annular Dark Field
Ag	Silver Chemical Symbol
Au	Gold Chemical Symbol
BF	Bright Field
CCVD	Catalytic Chemical Vapour Deposition
CNT	Carbon Nanotube
DFT	Density Functional Theory
Dh	Decahedral
EDS/EDX	Energy-dispersive X-ray Spectroscopy
Fe	Iron Chemical Symbol
FCC	Face-Centred Cubic
FFT	Fast-Fourier Transform
HAADF	High Angle Annular Dark Field
Ih	Icosahedral
LIR	Liquid Injection Reactor
MACS	Matrix Assembly Cluster Source
MiniMACS	Mini Matrix Assembly Cluster Source
MWCNT	Multi-Walled Carbon Nanotube
NC/NC's	Nanocluster/Nanoclusters'
PVD	Physical Vapour Deposition
PS	Polystyrene
SAI	Single Atom Intensity
STEM	Scanning Transmission Electron Microscopy/e
SWCNT	Single-Walled Carbon Nanotube
TEM	Transmission Electron Microscopy/e
U/A	Unidentified/Amorphous
VLS	Vapour-Liquid-Solid

Chapter 1

INTRODUCTION AND OVERVIEW

Overview

This chapter will introduce and summarise this PhD thesis as a whole in addition to, providing an outline of the structure of this thesis as well as, the motivation behind and end objective of this thesis.

1.1 Overview and Context

Nanoscale technology (1-100 nm regime) “Nanotechnology” represents the latest frontier in both technological and industrial development with the key to this being the production and understanding of new nanomaterials. Despite its name, the use of nanotechnology is not isolated to the computing and technology industry, and can in fact be linked to a large number of industry sectors including; Food, Medicine, Energy, and Environmental to name a few. Its wide variety of uses can be attributed to the ability to tailor the structures and compositions of materials on the nanoscale to achieve specific properties. Many of which are already applied to everyday products without the consumer realising, an example being waterproof coatings on glasses [1, 2]. The wide applicability of nanotechnology stems from the diverse forms it can come in, this can vary from thin films to nanoparticles. In the electronics industry this has lead to enhancement of device performance and efficiency whilst in the environmental industry this has led to improved water quality through removal of contaminants and pollutants [2, 3]. New advancements with the aid of nanotechnology are being made everyday with it being noted as a key factor in achieving sustainable development goals in addition to, the drive to improve on existing technologies. As a result, the requirement for continued research and understanding of new and existing nanomaterials is vital for future scientific and industrial progress [2, 3].

As previously mentioned, materials in the nanoregime can come in numerous different shapes and sizes however, two in particular present great promise in a wide variety of applications; Carbon Nanotubes and Nanoclusters. In 1993 it was discovered that single-walled carbon nanotube (SWCNTs) could conduct electricity about 70 times faster than silicon, making it an promising discovery for the electronics industry [3, 4]. On the other hand, multi-walled carbon nanotubes (MWCNTs) were found to have mechanical strength applications [3]. In contrast, nanoclusters open up the opportunity to explore materials and devices with precisely tuned applications ranging from catalysis, to sensing, to optics and photonics. The key in this structure being the atomic and nanoscale size and composition of the clusters, resulting in greatly varied properties in comparison to their bulk material equivalent [3, 5]. The realisation and understanding of these properties however, requires specialist analysis of the full synthesis process and end nanomaterial as will be illustrated in this thesis.

1.2 Outline of Thesis

This thesis has been structured into 7 chapters. An outline of the content of each of the succeeding chapters is described below. A brief appendix with supporting information is also presented at the end of this thesis.

Chapter 2

In Chapter 2, a literature review is carried out to provide a background to the topic of nanoclusters introducing the basic concepts relating to this field. Here, this begins by giving a brief overview of the subject before reviewing the various methods for producing nanoclusters with a focus on those relevant to this thesis. The topic of nanocluster growth is then discussed in the context of; deposition and formation as well as, the atomic sizes and structures of synthesised nanoclusters. In addition, an experimental review is conducted where the imaging techniques: HRTEM and STEM are introduced. Here, the operating principles for each imaging technique will be detailed along with the various imaging methods. For HRTEM, this will include standard TEM imaging as well as, diffractive imaging. In the area of STEM, this will include standard STEM imaging and the various detectors employed as well as, AC-STEM.

Chapter 3

In Chapter 3, the regeneration and recommissioning of a Caesium Sputtering Negative Ion Cluster Source is presented. This includes details of the operating principle behind the source stage of the system as well as a breakdown of the various stages of the system itself. The regeneration phases are then described including digitisation of the system as well as the design and installation of a new load lock. To recommission the cluster source, mass and cluster spectra are then carried out and then compared with previous results to evaluate the current performance of this cluster deposition system.

Chapter 4

In Chapter 4, details of investigations into the surface and structural characteristics of grown Carbon Nanotubes are presented. Initially, a literature review of the basic concepts of Carbon Nanotubes is given followed by, descriptions of the methods and techniques employed to both synthesise and analyse the produced Carbon Nanotubes. Results of HRTEM investigations are then presented, first covering the surface properties before transitioning to the core structure characteristics of the Carbon Nanotubes.

Chapter 5

In Chapter 5, the methods used to analyse AC-STEM images of nanoclusters is presented along with details of investigations into produced Ag nanoclusters. Here, this begins with descriptions of the techniques employed to first determine the atomic size of nanoclusters through single atom calibration. This is followed by discussion of the multiple techniques used to estimate both the geometric and isomeric structures of nanoclusters. The first set of investigations into Matrix-Assembled Ag nanoclusters are then presented and discussed.

Chapter 6

In Chapter 6, the results of analysis into surface assembled Au nanoclusters are presented. First, a short description of the production method used is given, describing the nature of the nanocluster growth in this method. Using the same analysis techniques as described in the previous chapter, size and structure investigations are then carried out and discussed where the structure is reviewed from a geometric and isomeric viewpoint.

Chapter 7

In Chapter 7, the findings presented in earlier chapters are summarised and concluded. Furthermore, any interesting observations are discussed from the viewpoint of potential future investigation.

1.3 Motivation and Objective of Work

The use of nanomaterials represents the next step in technological advancement, particularly in the area of electronics where a main drive has been the scaling down of devices thus enabling an increased number in the same package. This being more commonly known as *Moore's Law* [6]. In order for this to ring true however, component sizes would have to continue to decrease and indeed have with the current level of performance known as the *3 nm Process* [7]. On the nanoscale there are however numerous applications for particles and structures of a variety of shapes and sizes where properties are highly dependent on such factors thus opening the possibility for nanoscale structures with specific properties [8].

Synthesis of such nanostructures is not trivial however, and heavy research must be performed to understand the optimum production methods and conditions for achieving desired structures. In this thesis the size, structure, and growth mechanisms of atomic clusters produced through two Physical-Vapour-Deposition (PVD) methods in addition to, surface and core structure investigations on Chemical-Vapour-Deposition (CVD) grown carbon nanotubes are investigated. They have then been analysed with the aim of further understanding these nanostructures, their synthesis methods, potential applications, as well as understanding the analysis techniques themselves. Furthermore, the development and recommissioning of a cluster-beam deposition source is presented and discussed to understand one of the many methods for production of atomic clusters'.

The objective of this work is to develop a strong knowledge of a selection of PVD synthesis and analysis techniques for nanostructures, with a focus on nanoclusters and their formation through surface interaction. These results will create a positive future contribution to research involving nanocluster formation and analysis as well as, ultimately supporting the advancement of technologies and applications utilising these nanostructures.

Chapter 2

REVIEW OF NANOCLUSTER SCIENCE AND TRANSMISSION ELECTRON MICROSCOPY IMAGING

Overview

This chapter will present, discuss, and summarise the topic of nanoclusters of which the majority of this work is based. This will include a general overview of the subject, a review of various production methods employed in the synthesis of nanoclusters, a breakdown of the deposition and formation methods involved in PVD synthesis, as well as a review of the sizes and structures that can be obtained during the synthesis process. Furthermore, a brief review of the history of electron microscopy will be presented for which this is the main method for analysis of nanostructures.

2.1 Nanoclusters

This section of the chapter will look to introduce the topic of nanoclusters in the context of this thesis. This will include a general overview of the topic, approaches to the production and synthesis of nanoclusters, deposition techniques and formation mechanisms of nanoclusters, as well as a look into the atomic sizes and structures of nanoclusters.

2.1.1 Overview of Nanoclusters

Nanoclusters' (NC's) are nanoscale groupings of atoms in an assortment of shapes and sizes, though primarily in the sub 2 nm size range [9]. The shape or arrangement of these NC's is referred to as the 'Isomer', of which there are numerous. For the context of this thesis, three isomers are focused on: Icosahedral (Ih), Face-Centred-Cubic/Cuboctahedral (FCC), and Ino-Decahedral (Dh). The critical feature of NC's is that their properties are dependent on the atomic size of the cluster [8, 9]. This does not mean however that NC's of a specific atomic size can be freely produced, a NC of a certain size also has a certain stability. There are however specific NC sizes which are especially stable, these sizes are known as magic numbers as will be discussed later on in this chapter [8].

Nanoclusters' represent a new advancement in material property manipulation with applications in numerous areas such as; optics, electronics, catalysis, mechanical materials and more. Deposition of NC's onto the surface of materials to form particle coatings or thin films, allows for the production of materials and devices with unique and tunable properties [8]. The tunability of these properties can further come from not only the size of the NC's, but also their internal structure, and the materials contained within the NC's.

2.1.2 Production Methods

The production of NC's can be achieved through numerous methods across the biological, chemical, and physical fields. In general, each method is categorised as either a Top-Down or Bottom-Up approach. Bottom-up synthesis involves building up from single atoms. This can be achieved through techniques like vapour deposition where atoms aggregate to for larger NC's. Alternatively, Top-Down synthesis involves breaking down bulk materials to NC size. This can be done through techniques like sputtering. A summary of these approaches is illustrated below in Figure 2.1.

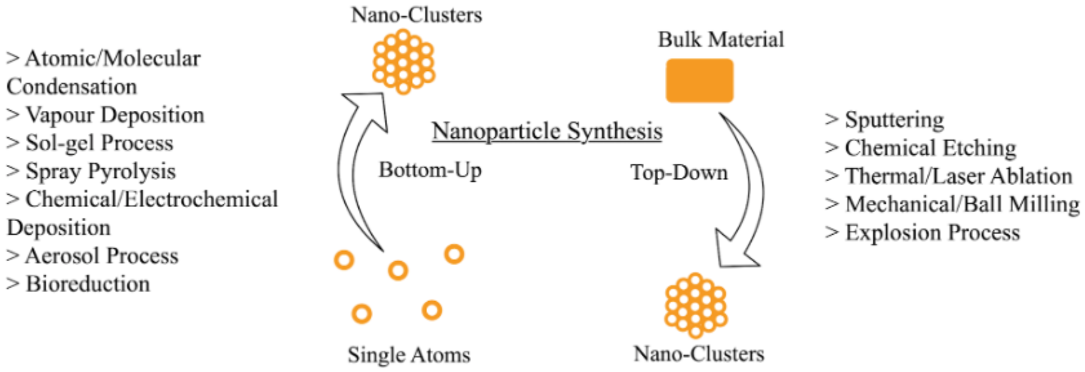

Figure 2.1: Top-Down and Bottom-Up approaches to synthesis of atomic clusters' after [10]. The Bottom-Up approach demonstrates the growth of nanoclusters' by the aggregation of single atoms into a larger cluster. In contrast, the Top-Down approach shows how larger bulk material is broken down into atomic clusters'. Example processes for each of these approaches are given.

In this thesis the Top-Down and Bottom-Up methods; Sputtering and Thermal Evaporation are utilised respectively in addition to a new method, Matrix Assembly, to deposit NC's onto substrates. These will be detailed in Chapters 5 and 6.

Sputtering

Sputtering is a widely used method for thin film deposition and nanoparticle generation, and involves the ejection of atoms from a target material through the bombardment of energetic particles, ions, on the target [11, 12]. The bombardment of energetic particles can be achieved through two processes: the use of an ion source, or ion plasma [11]. Sputtering through an ion source (Ion Beam Sputter Deposition - IBSD) involves aiming a beam of energetic ions directly at the target to be sputtered, where ejected particles can be collected on the substrate [11, 13, 14]. In contrast, sputtering through ion plasma involves either the heating of a gas or presenting a gas with a strong electric field until the electrons become detached from their parent atom or molecule [15]. The generated positively charged ions can then be attracted to the target material by applying a high negative voltage [11]. The electric field generated cause the ions to gain sufficient energy to bombard the target and initiate sputtering [11]. This approach can be summarised into three methods depending on setup and configuration; Magnetron, DC, and RF sputtering.

In this thesis, two types of sputtering are employed to produce single atoms and nanoclusters': Ion Beam Sputter Deposition (IBSD), and an adaptation of DC sputtering employing Caesium as the sputter mechanism. Both of which will be elaborated on in Chapters 5, 6, and briefly in Chapter 7.

Thermal Evaporation

Thermal Evaporation is one of the most common methods of physical vapour deposition [16, 17]. This process utilises both high temperature heating and a vacuum to produce a vapour of the evaporated material and direct it towards a substrate [16–18]. Upon encountering the substrate, a thin film of the material is grown, and the material is returned to a solid state [16, 17]. This method is hence referred to as a method of thin film deposition [16]. Thermal evaporation can be achieved through using one of two different approaches: Filament Evaporation or Electron-Beam Evaporation (E-Beam) however, the term 'Thermal Evaporation' most commonly refers to the former of the two. There are many different designs surrounding thermal evaporation however, the principle of operation remains the same. Thermal evaporation techniques employ joule heating of a material located in a boat or crucible to raise the temperature of the material to its evaporation point. This is done through the utilisation of high power electrical supply's commonly in the order of several hundred watts where a large current is primarily responsible for the high temperatures produced. The vaporised material then travels and is deposited onto the substrate where it can aggregate to form small particles or a thin film [19].

In this thesis, filament heated crucibles are used to vaporise materials for co-deposition with argon to form a matrix. These methods will be described further in Chapter 5.

E-Beam Evaporation

Electron-Beam Evaporation (E-Beam Evaporation), like its name suggests, also utilises heat to evaporate the desired material however, the method used to vaporise the target material is quite different. Compared to filament evaporation, in E-Beam evaporation a filament is used to “boil” off electrons which are then accelerated by a large potential difference in the order of kV’s to form an electron beam. The generated beam current however is on the scale of mA’s. This beam is then steered by magnets towards a crucible containing the material to be evaporated. It is this concentrated application of high energy electrons that is used to heat up the material producing a vapour [16]. The vaporised material, as in thermal evaporation, then travels to the substrate where it can aggregate to form small particles and thin films.Due to the concentration of this power, the crucible itself requires cooling to prevent its own destruction [16].

In this thesis, E-Beam evaporation is used to produce thin films for ion beam sputtering. The application of this method with be detailed further in Chapter 6.

Matrix Assembly

Matrix assembly is a relatively new technique for producing a beam of nanocluster’s. In short a matrix of rare gas atoms impregnated with atoms from a target material is grown before being sputtered by an Argon ion beam [20, 21]. The matrix is grown on a cold-finger support maintained at a temperature between 10-15K with the target material being evaporated through Thermal or E-beam evaporation and co-condensed Argon gas [20–22]. The presence of the Argon in this growth mechanism is essential, by the laws of conservation of energy and momentum, for aggregation of two metal atoms in a three-body collision [22]. Left on their own, atoms and clusters’ would naturally aggregate in the grown matrix however, this would take time. To speed up this nucleation process as well as create a method for ejecting the grown clusters from the matrix, an Argon ion beam is used to sputter the matrix and direct the clusters’ towards a substrate [20–22]. The use of an Argon ion beam in this way also has the added effect of ‘stirring’ the matrix causing further cascade collisions and clusters’ to nucleate [20–22]. Clusters’ produced using this method can also be size-selected to a certain degree through the control and tuning of matrix growth and sputter parameters such as the metal loading, matrix temperature, and sputtering conditions [21]. A schematic illustration of this technique is shown below in Figure 2.2.

In this thesis, Matrix Assembly is used to produce cluster's for HAADF-STEM analysis. The precise use of this method will be described further in Chapter 5.

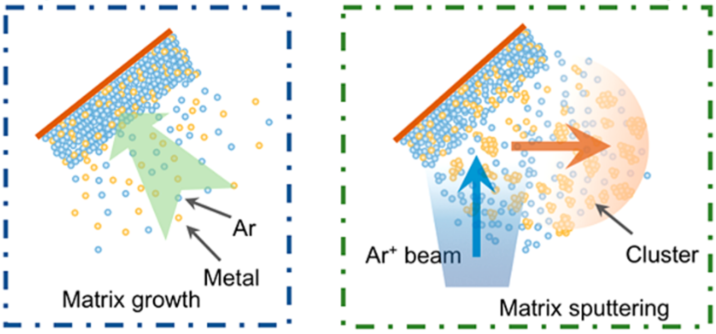

Figure 2.2: Schematic representation of the Matrix Assembly Nanocluster synthesis method [20]

2.1.3 Deposition and Formation

As previous described, deposition and formation of nanoclusters can be achieved through numerous different techniques characterised as either a top-down or bottom-up approach. However, as will now be detailed, the size and structure of the end nanocluster is also dependent on deposition conditions and interactions with the substrate material.

Landing Techniques

The term landing techniques refers to how the produced particle or cluster initially reacts with the substrate and this is dependent on a number of factors including Energy, Particle Size, and Substrate Hardness. For example a low energy Au cluster may soft-land on a substrate whilst a high energy Au cluster may embed or fragment [23]. An illustration of some of the various processes that can be undertaken is given below in Figure 2.3. Understanding these processes is key in the production of nanoclusters where a change in landing process may effect how a particle is structured and thus its properties in application.

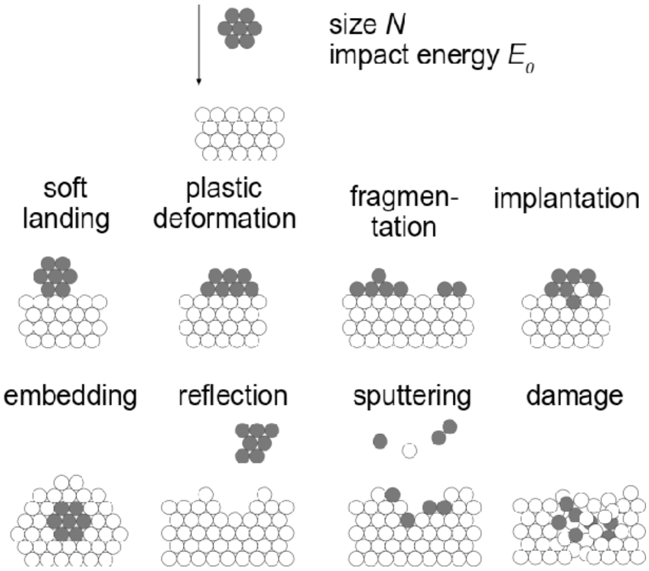

Figure 2.3: Illustration of the different processes that can occur when a cluster deposits onto a substrate [23]

In the context of nanoclusters where size is variable, the impact or deposition energy is often given as 'Electron-Volts per Atom' (eV/atom) where the value can then be universally applied to clusters provided the size is known. The difference between soft landing energies and embedding energies however, is often only a few eV/atom or less, with a upper bound for soft landing conditions being given as $< 1eV/atom$ [23, 24]. Previous works by Pelletier et al., and Popok et al., have demonstrated both large (few eV/atom) and small (meV/atom) changes in impact energies can be the difference between different landing processes depending on the various synthesis conditions [24, 25]. In addition to this, the landing effect can also be dependent on the materials used for both the nanocluster and the deposition substrate. This makes the setting of discrete energy boundaries for different landing techniques very difficult, often requiring tailored simulations where the difference between deformation and sputtering could be a few $eV/atom$ to $10s$ $eV/atom$ depending on nanocluster size, materials used, and process conditions [23, 25]. For nanoclusters in the order of thousands of atoms in size, kinetic energy becomes the more important factor in determination of the landing technique [25].

In this work, nanoclusters are synthesized and deposited at room temperature with low impact energies $(approx 25meV)$ to encourage soft-landing and surface aggregation. This will be further detailed in Chapters 5 and 6 in the contect of Silver (Ag) and Gold (Au) nanoclusters respectively.

Surface Interaction and Aggregation

Particles, both single atoms and nanoclusters, ejected during the sputtering process, both neutral and ionic, continue to be energised whilst in flight and initially when landing on a substrates surface. As a result of this retained energy, deposited particles continue to move or diffuse across a substrates surface. The extent of this diffusion is dependent on the particle size and energy, where larger particles inherently have more contact points with the surface and thus require more energy to move. Results of this surface diffusion include aggregation and nucleation with other particles to form and grow nanoclusters, islands, and layers [26–28]. Growth of these nanoclusters, islands, and films can occur in three different modes: Frank-van der Merve (FM), Stranski-Krastanov (SK), and Vollmer-Weber (VW), named after their original investigators. These are demonstrated below in Figure 2.4 [28].

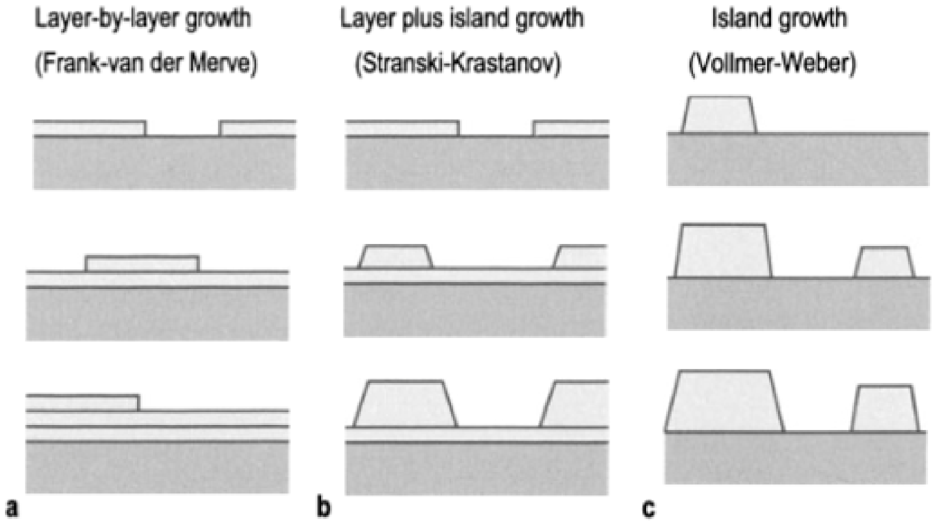

Figure 2.4: Schematic representation of the three main growth modes of clusters'/films from [28]. a) Layer-by-Layer (FM) growth mode; b) Layer-Plus-Island (SK) growth mode; c) Island (VW) growth mode. The stages of growth for each mode is portrayed in a top down fashion.

In the Frank-van der Merve mode, growth occurs through a layer-by-layer method where atoms have a stronger bond with the substrate than between each other. This gives way to the formation of complete layers [28]. This growth mode is common in the synthesis of thin films where layers are grown atom by atom. Alternatively, in the Stranski-Krastanov growth mode, where islands are seen to form during growth before the completion of layers. This is a result of a non-uniform layer growth rate which is represented as islands [28]. This can occur as an artefact of the synthesis process, particularly in sputtering, or as a result of synthesis using mixed materials or growth as a result of varied deposition particle sizes. Finally, in contrast is the Vollmer-Weber growth mode where islands are the only growth structure. This is an example of a greater atom to atom bond strength in comparison to atom to substrate bond strength, thus resulting in island or nanocluster growth [28]. This particular growth mode is the most frequent in nanocluster growth where atoms and small nanoclusters diffuse across the substrate surface and aggregate to form larger nanoclusters.

2.1.4 Sizes and Structures

The size and structures of nanoclusters is extremely varied, and very much dependent on numerous factors such as the synthesis method used and deposition energy. In this section, metastable cluster sizes and structures will be introduced and discussed including the topics of magic numbers and isomer structures.

Magic Numbers

First termed in 1981 by Sattler et al., ‘Magic Number/s’ in nuclear and cluster physics refers to an atom or particle of nuclear or atomic size N respectively that is particularly metastable [29–31]. Whilst in both cases the term ‘magic number’ refers to stability, the context in which this is applied is quite different. These can therefore be categorised into either *Electronic* and *Structural* magic numbers relating to nuclear and cluster physics respectively, of which both will be detailed in the following sections.

Electronic Magic Numbers

In the context of nuclear physics, this refers to the stability of the nucleus where is it have been found that nuclei with even numbers of protons (Z) and neutrons (N) are more stable than those with odd numbers. The term ‘Magic Number’ arises from the completion of nuclear shells by either protons or neutrons separately, where specific proton and neutron counts have been found to be specifically stable e.g. 2, 8, 20, 28, 50... [30, 32, 33]. The presence of these magic numbers suggests a closed shell configuration as in atomic structure which in-turn has led to the creation of a *Shell Model* to explain this phenomenon, as demonstrated below in Figure 2.5 [32, 33].

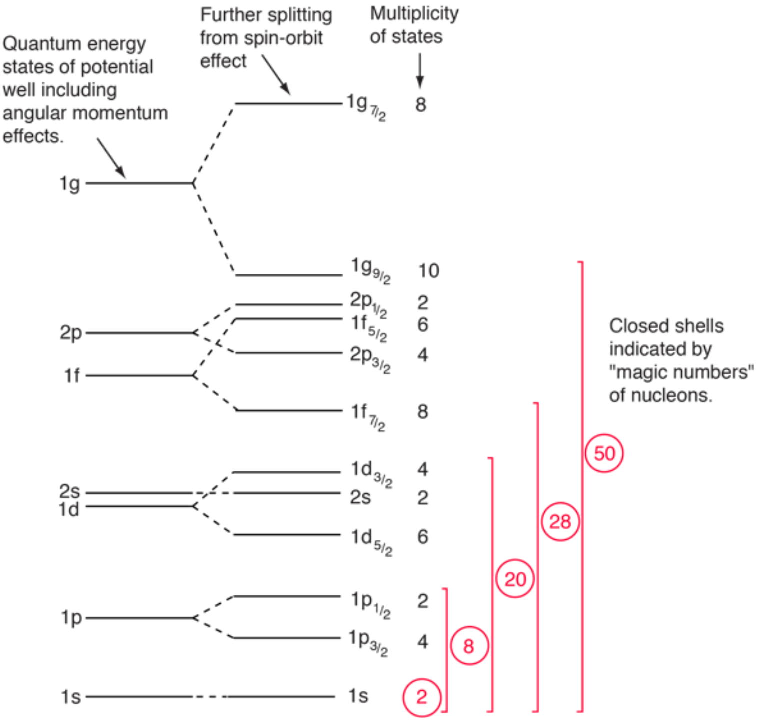

Figure 2.5: Illustration of the nuclear shell model demonstrating a closed shell structure by the presence of magic numbers of nucleons [33].

In addition, nuclei can also be considered *Doubly Magic* when the condition arises where both the number of protons (Z) and the number of neutrons (N) are both equal to one of the magic numbers. In this case, nuclei are considered exceptionally stable. An example of this can be seen in Calcium which has two 'doubly' magic isotopes; $^{40}_{20}$Ca and $^{48}_{20}$Ca which have 20 and 28 neutrons respectively in addition to 20 protons [33].

Structural Magic Numbers

Previous work has observed a similar relationship with numerous Sodium (Na) clusters where large peaks appeared on mass spectra at 2, 8, 20, 40, ... atoms which was attributed to cluster of particularly high stability [29, 30]. Analogous to the nuclear shell model, Knight et al. attributed these metastable clusters to having 'magic number' sizes and hence was said that these clusters have a 'magic number' of atoms [30]. This metastability and hence magic numbers are not the same for every material however, numerous studies have demonstrated a variation in the metastability occurrences depending on the base material. The stability of cluster's however, has been said to become more and more difficult to predict as the size of the particle increases and the surface to volume ratio decreases. Thus an exact number at which a cluster is metastable is not always predictable [34]. Additionally, there is no set rule or equation for determining a materials magic numbers and in the case of transition metals, which are quasi-de-localized and possess a magnetic moment, this identification is even more difficult [30, 34]. Geometric structure stability offers a solution however, where specific numbers of atoms are geometrically stable, e.g. geometric magic numbers [34]. Previous work has shown a pattern for stable Icosahedral (Ih), Decahedral (Dh), and Cuboctahedral (FCC) isomer packings in sizes: 1, 13, 55, 147, 309, 561... [34, 35]. This has been shown to correspond to rare gas clusters where the magic numbers are ruled by the close-packing sphere rule, also a geometric shape [30]. For clusters' of sizes greater than 13 atoms, this geometric magic number pattern or close-packing sphere rule, in addition to its structure, is used as an identifier.

Isomer Structures

As mentioned previously, the term 'Isomer' refers to the geometric packing arrangement of the atoms in a nanocluster. There are numerous different types of isomer, and it has already been shown that the number of metastable isomers increases quickly with the number of atoms in the cluster [34]. Three isomers in particular are observed and discussed in this thesis; Icosahedral (Ih), Ino-Decahedral (Dh), Cuboctahedral (FCC). It has been found previously that these three isomers share the same sizing relationship which can be characterised by Equation (2.1), where 'n' denotes the number of shells in a cluster [36]. As in the nuclear shell model, the completion of each shell denotes a metastable point for the cluster and hence the magic number can be determined by the total number of atoms in a completed shell structure. As it will be demonstrated, these configurations are quite different in both quasi-shape and crystallinity.

$$N_{Atoms} = \frac{(10n^3 - 15n^2 + 11n - 3)}{3} \tag{2.1}$$

By modification of Equation (2.1), it is possible to determine the number of surface atoms for each isomer structure as shown by Equation (2.2).

$$N_{Surf} = 10n^2 - 20n + 12 \tag{2.2}$$

Through use of both Equations (2.1) and (2.2), it is possible to tabulate the relationship between a clusters' number of shells, number of atoms, and number of surface atoms, as well as the resulting surface to volume ratio (SA/V). This is shown in Table 2.1.

Table 2.1: Table of values of total and surface atoms for clusters' with n shells. Each shell represents addition of N atoms on the surface of the previous shell. N_{Atoms} denotes the total number of atoms in a cluster with n shells. N_{Surf} denotes the number of atoms on the surface of a cluster with n shells. SA/V denotes the surface to volume ratio of the structure as a percentage.

Shells	1	2	3	4	5	6	7	8	9
N_{Atoms}	1	13	55	147	309	561	923	1415	2057
N_{Surf}	1	12	42	92	162	252	362	492	642
SA/V	100%	92.3%	76.3%	62.5%	52.4%	44.9%	39.2%	34.8%	31.2%

The Icosahedral isomer structure can be described as a 20-faced quasi-spherical structure and of the three, most resembles a true sphere. However, unlike the FCC and Dh isomer structures, Ih is not described as crystalline but in fact described as ordered non-crystalline or quasi-crystalline configuration due to its incompatibility with periodic models yet high degree of symmetry [34, 37, 38]. Like others, this structure begins with a single atom from which surface atoms are added forming triangular faces with a mix of five-fold, three-fold, and two-fold symmetry as demonstrated in Figure 2.6.

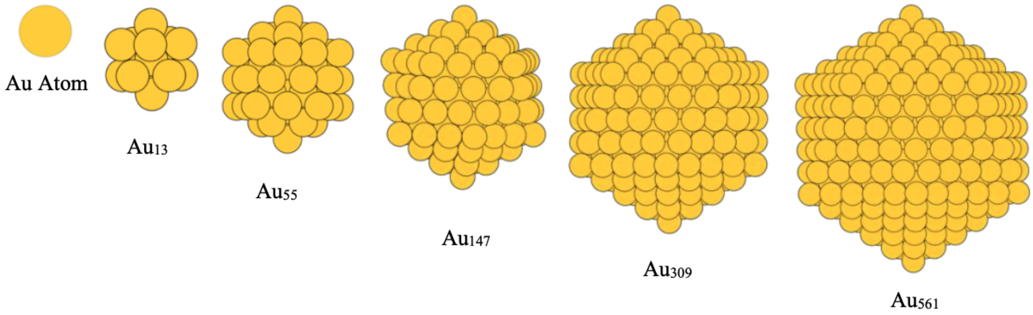

Figure 2.6: Demonstration of Au 1-561 Icosahedral structured clusters'. The size of clusters' is shown to increase however, the shape and isomer structure are shown to be the same but on a larger scale. A single Au atom is the exception where only a spherical shape is given. Code for construction of clusters' from [39].

The Cuboctahedral isomer structure is the most closely packed of the three isomers at 0.74 and can also be described as a quasi-spherical structure however, unlike the Icosahedral structure, this structure is made up of only 14 faces mixed as both square and triangular faces as demonstrated in Figure 2.7 [40–42]. This represents only one of many FCC structure types although, unlike the Icosahedral structure, Cuboctahedra as well as other FCC structures are classified as crystalline and such nanoclusters are often treated as a fraction of the bulk material [34, 41]

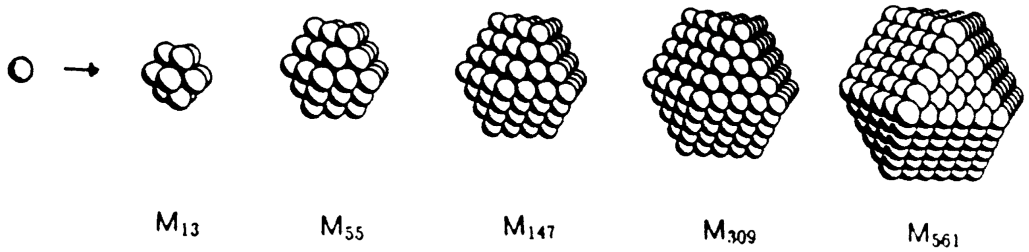

Figure 2.7: Example Au 1-561 Cuboctahedral isomer structured clusters' from [43]. The size of clusters' is shown to increase however, the shape and isomer structure are shown to be the same but on a larger scale. A single Au atom is the exception where only a spherical shape is given.

Finally, is the Decahedral isomer structure. Similar to the previous two, this structure is also quasi-spherical and like the Cuboctahedral structure is also crystalline in nature. Observable in Figure 2.8, this isomer structure consists of 15 faces and also like Cuboctahedra, contains a mix of square and triangular faces [34]. However, in addition to this, the Decahedral structure also contrains a single five-fold axis symmetry [44].

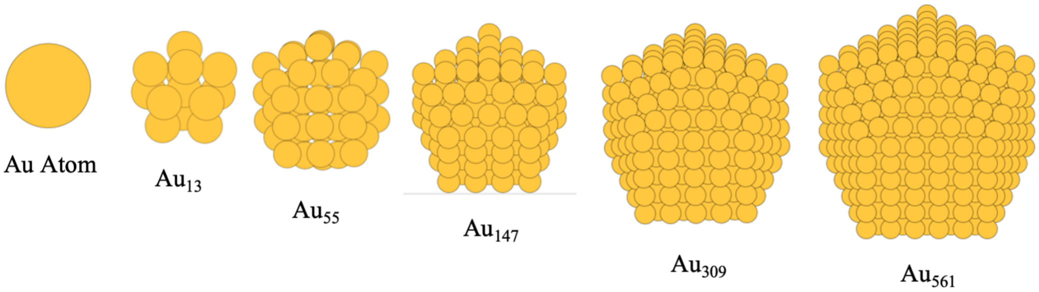

Figure 2.8: Example Au 1-561 Ino-Decahedral isomer structured clusters. The size of clusters is shown to increase however, the shape and isomer structure are shown to be the same but on a larger scale. A single Au atom is the exception where only a spherical shape is given. Code for construction of clusters' from [39].

As will be discussed in Chapter 4, it is extremely rare for clusters formed through deposition and surface aggregation to be of the exact same size and shape as illustrated in Figures 2.6 to 2.8.

2.2 Introduction to Transmission Electron Microscopy

This part of the chapter will aim to provide a short background to the topic of Electron Microscopy where it is required for the imaging and analysis of nanoscale structures. This will include; a brief introduction into the types of electron microscopy and their uses with a focus towards the techniques used in this thesis in addition to, a review of Transmission Electron Microscopy (TEM) and Scanning Transmission Electron Microscopy (STEM) imaging.

2.2.1 Overview of Electron Microscopy

Electron microscopy can be summarised into two categories; Transmission Electron Microscopy (TEM) and Scanning Electron Microscopy (SEM) and whilst both are quite different, each utilises similar principles and components to analyse structures on the nanoscale. As will be explained in the following chapter, in both types of electron microscope, electrons are excited from an electron source before being focused through lenses onto a sample where scattered electrons are used to obtain information about the sample [45]. In SEM, electrons are focused to a fine point on the sample surface. This convergent electron beam is then scanned across an area of the sample in a raster pattern. In this method, low-voltage secondary electrons emitted from the sample are collected by a detector to form a digital image [45, 46]. As a result of the collection of emitted secondary electrons, SEM allows for a detailed understanding of the surface structure of samples [45]. In contrast, TEM allows for detailed understanding of the internal structure of sample materials. Here a parallel electron beam is focused onto and through the sample where transmitted and diffracted electrons are collected by a specialised camera to produce an image of the samples internal structure [45, 46]. In addition, these two categories can also be further combined into one instrument to produce Scanning Transmission Electron Microscopy (STEM), which can further be used to provide information on the compositions and structures of samples at higher magnifications [46]. The fundamentals of TEM and STEM imaging will be further described in the following sections.

2.2.2 The Transmission Electron Microscope

This section will introduce the topic of Transmission Electron Microscopy. This will include; an overview of the operation of a transmission electron microscope, HRTEM imaging and diffraction pattern inspection, as well as STEM and AC-STEM imaging.

Operating Principle

The purpose of a Transmission Electron Microscope (TEM) is to produce images of particles and structures that are of the nanometre scale. Its working principle is quite similar to that of a optical microscope however, where an optical microscope uses light to focus and produce an image, the TEM uses a beam of electrons to image an ultra-thin sample ($<$*100nm*) [47, 48]. The requirement for using electrons comes about due to the need to image on the nanometre scale which necessitates a much higher resolution. This is achieved because of the difference of wavelength between light rays and electrons where electrons have a much smaller wavelength than that of light. The result is an optimal resolution that is many orders of magnitude higher than from a optical microscope [47, 49]. This allows for the imaging of the smallest structures, unveiling new information into the internal nature of nanometre scale particles, and under optimum conditions even atomic scale features [48, 49]. To achieve this level of detail however, the TEM is composed of a complex arrangement of lenses and apertures to produce the fine focused electron beam required for imaging as displayed below in Figure 2.9 [47–49]. As a whole however, the instrument can be summarised into three stages; the illumination system, objective lens and stage, and imaging system, each containing multiple individual components [50].

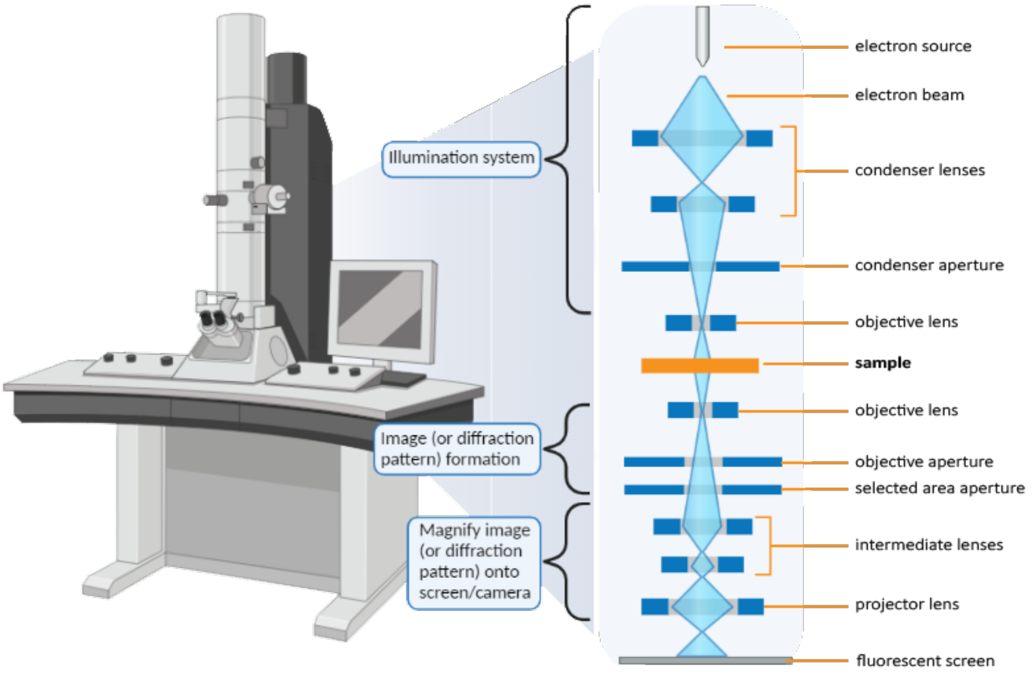

Figure 2.9: Simplified TEM breakdown diagram highlighting the various components and their order within a TEM [51].

The illumination system refers to the part of the microscope that is responsible for generating and focusing the produced electron beam onto the sample. This is comprised of two components; the electron gun/source, and the condenser lenses. As will be described later, the illumination system can produce an electron beam in two different forms depending on the imaging mode being employed, these are a parallel beam for TEM mode, and a convergent beam for STEM mode [50]. The Objective lens and Sample stage are a combination at the centre of the TEM and are the primary components for forming reproducible images and diffraction patterns. In this section both the Objective lens and Specimen holders will be detailed, describing how they work and the roles they play in the capture of the various forms of image [50]. Once the electron beam has been formed and focused onto and through the sample, it is then the job of various lenses, screens, cameras, and detectors to produce the information in the form of an image [50]. Control computers allow for remote operation of the microscope and its various components through specialist software. Due to the complex operation of the microscope as well as employment of various different pieces of analysis equipment, often multiple computers are linked to a single microscope [51].

Aberrations and Astigmatism

Despite the use of multiple lenses to produce the optimum electron beam shape and size, there are still a number of defects present of which the main ones are Spherical Aberration (C_s), Chromatic Aberration (C_c), and Astigmatism. Aberrations can be seen to be the result of differences in the properties of the travelling electrons in the electron beam whereas, Astigmatisms occur as a result of defects in the lenses themselves [50]. Spherical aberration occurs as a result of the difference in interaction between off-axis electrons and the magnetic field of the lenses. As previously mentioned, in an electromagnetic lens, the further the electron from the centre, the stronger the electron is bent back to the centre axis. As a result, the cross-over point for electrons after passing through a lens is different depending on the off-axis degree when entering the lens. In imaging terms this results in a non-uniform focal point within the beam as illustrated in Figure 2.10a. Such an aberration prevents the achievement of higher resolution images such as on the atomic scale, fortunately this can be corrected through the use of a C_s corrector which refocuses all off-axis electrons to the same single point as shown in Figure 2.10b [50].

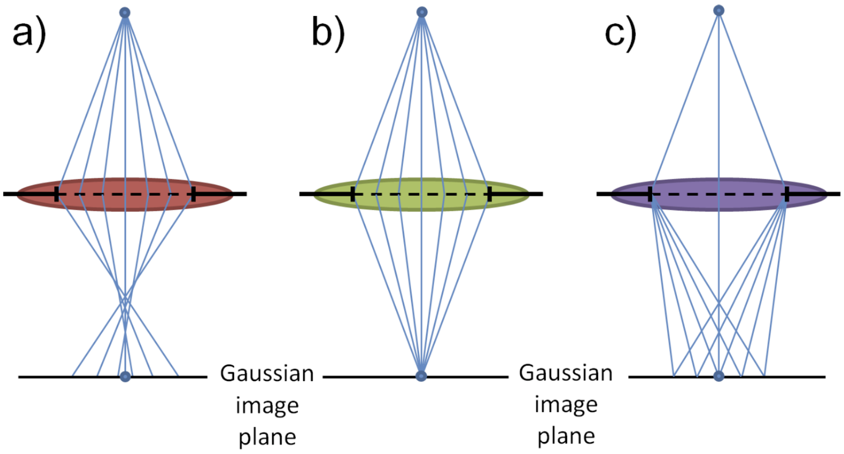

Figure 2.10: Illustration of the types of Aberrations present in TEM imaging, a) Spherical, b) Ideal, c) Chromatic [52].

On the other hand, Chromatic aberration occurs as a result of energy differences in the generated electrons. This stems mostly from the type of electron source used where the energy spread can be as little as *0.3eV* for a cold-FEG compared to upto *1eV* for a

LaB_6 Thermionic source. The effect this has is that electrons with differing energies, respond differently when passing through the electromagnetic lenses where the convergence angles differ. This is demonstrated above in Figure 2.10c. Furthermore, Chromatic aberration also occurs when passing through thicker samples and inelastic scattering occurs, this is one reason why sub-100 nm thick samples are preferred for high resolution imaging and analysis [50, 51]. For the most part however, the effect of Chromatic aberration can be considered negligible in non Spherical aberration corrected TEMs where the image resolution makes it unnoticeable. However, in C_s corrected TEMs, Chromatic aberration can begin to be noticed. Chromatic aberration is beginning to be corrected in some analysis techniques such as EELS through the use of Monochromators where electon energies are very important and correctors for use further up the column are in development. Unfortunately, due to the multiple causes of Chromatic aberration, progress of C_c correction is very much limited [50, 51].

Unlike aberrations, Astigmatisms occur as the result of defects in the lenses, specifically in the quality of the soft-Iron pole-pieces which cannot be manufactured as perfectly symmetrical all the way through the bore. As a result of this, a non-uniform magnetic field is generated causing the passing electrons to spiral about the optical axis. This effect also arises from issues such as off-axis apertures and built up contamination which can disturb the magnetic fields. Fortunately, this can be created through the use of devices called Stigmators. These are small octupoles that correct the non-uniform magnetic fields by introducing a compensating magnetic field to restore balance. Multiple Stigmators are often employed in a TEM system and are most commonly found after the Condenser and Objective lenses [50].

Beam Effects

In addition to imperfections in the electron beam and lenses, beam-sample interaction must also be considered. As a form of ionizing radiation, exposure to the electron beam can damage samples in a variety of different ways however, there are also ways to reduce and mitigate these effects. Examples of common beam-induced effects will be described here along with techniques for reducing these effects.

Beam-Induced Damage

Beam-induced damage can occur in a variety of different forms with effects such as; Carbon contamination, heating, vibration and displacement, and even sputtering, being very common [50, 53]. The first of these effects is carbon contamination whereby carbon ions are attracted to areas exposed to the electron beam. This is most pronounced when imaging in STEM where a high intensity small sized (high dose) beam is scanned in a raster pattern over an area of the sample. This high dose scanning encourages the build-up of Carbon over the scanned area and, in some cases can prevent the sample underneath from being distinguished [50, 53].

The second form of damage that can occur is sample heating which is again most pronounced in high dose imaging. Here the electron-beam interaction with the sample generates heat in the area focused on, and its effects can vary depending on the composition of the sample. For example, in polymer samples this can result in the melting and evaporation of the sample whilst in Carbon based samples, excessive heating can burn physical holes in a sample [50, 53]. Luckily, these two effects are often focused on a small area of the sample allowing for imaging to continue in a different area.

The final form of beam effect reviewed here is common to small particles such as the nanoclusters imaged in this thesis. Here exposure to the electron beam can cause vibrations, particle displacements and even sputtering, whereby the resulting effect is determined by the exposure dose and time. In the context of nanoclusters, vibration effects occur when the electron beam provides enough energy for the composing atoms to vibrate cause a nanoclusters structure to reorganise itself. In this case the electon beam can be considered to have altered the sample thus making any results irrelevant. Displacement and sputtering however, occur when a nanocluster or particle gains enough energy to diffuse across the sample, or in extreme cases, cause it to be ejected from the sample entirely. This issue is common in STEM imaging, particularly when imaging is focused on few or single particles and therefore are exposed to high doses of electrons [50, 53].

Fortunately, there are techniques available, both pre-imaging as well as during imaging, to reduce and even mitigate these beam effects. These techniques will be described next.

Mitigation Techniques

As previously described, beam effects can potentially cause a number of issues when imaging samples in TEM and STEM. Certain steps can be taken however to reduce the likelihood of these effects occurring. In the case of Carbon contamination, two steps can be taken to avoid this during imaging. Firstly, where a sample is known to be heavily contaminated with Carbon, short durations of plasma cleaning allow for excess carbon to be removed from the sample prior to insertion into the TEM [50]. Care must be taken however when using this method as over plasma cleaning can begin to destroy a sample, leaving nothing left to be imaged. Alternatively, a technique known as beam showering can be used during TEM imaging to remove and disperse Carbon from a particular area of interest on the sample [50]. This can be achieved by exposing an area of interest on the sample to a high dose but broad electron beam thus removing Carbon contamination from that area. Unlike plasma cleaning however, this technique does not last and is only focused on an a specific area, and therefore must be repeated across other areas of the sample.

Effects such as heating, vibrations, and displacements, are all caused as a result of exposure to a high dose electron beam and can therefore be mitigated through reducing the exposed dose. How this is implemented however, can vary depending on the conditions at the time of imaging [50]. For example, area dosage can be reduced by reducing the magnification and therefore increasing the area being imaged, effectively lowering the dose per unit area. Alternatively, if high magnification is required, the exposure or dwell time can be altered to reduce the time a specific area is exposed to the high intensity electron beam [50]. In both cases the effective dose is reduced. Some situations exist however where samples are extremely sensitive to electron beam dosage such as polymers. In this case a technique known as low dose imaging exists whereby the electron source parameters are adjusted to significantly lower the overall intensity of the electron beam allowing for imaging of beam sensitive materials [50, 54].

2.2.3 TEM Imaging

Unlike Scanning Electron Microscopy which gives information on a samples surface and composition, Transmission Electron Microscopy is used to determine a samples inner structure. In this technique, a parallel electron beam from an electron source is focused through a series of electromagnetic and electrostatic lenses as well as electron apertures and passed through a thin sample [55]. The transmitted electrons passed through the sample are then collected on the other side by a specialised camera [56]. All this must occur under High/Ultra-High vacuum. TEM offers the ability to image at a significantly higher magnification than SEM however, this comes at a cost where the field of view of the sample is severely decreased. Furthermore, samples imaged under TEM are limited by their thickness, typically less then 150 nm further limiting applications [55]. In this section, the various types of image obtainable through a TEM operating in TEM mode, will be described.

TEM Image Formation

When operating in TEM mode, the selected area of the sample is exposed to a large parallel beam all at once producing on exit a series of diffracted/scattered electrons which are focused by the lower objective lens [50, 57]. From here, multiple further apertures and lenses are employed to produce the desired final image. The apertures employed here are known as the *Objective* and *Selected-Area Diffraction* apertures, whilst the lenses are known as the *Intermediate* and *Projector* lenses of which there are usually at least two intermediate lenses. The TEM has two primary forms of imaging mode; Diffraction mode, and Image mode, from which the resulting images greatly differ from each other. The choice of which imaging mode is determined through the use of one of the two available apertures and by adjusting the strength of the first intermediate lens. In diffraction mode, the objective aperture is removed and the selected-area diffraction aperture is inserted, and the first intermediate lens is adjusted to focus on the *Back Focal Plane* of the objective lens. In contrast, in imaging mode the selected-area diffraction aperture is removed and the objective aperture is inserted, and the first intermediate lens is adjusted to focus on the *Image Plane* of the objective lens [50, 58]. The implementation of each of these imaging modes is demonstrated below in Figure 2.11.

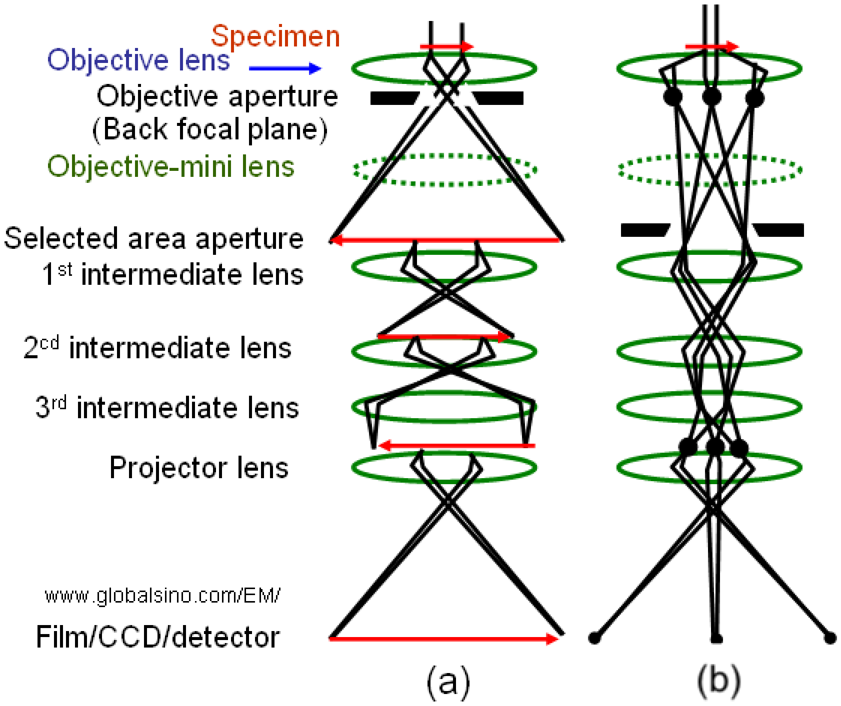

Figure 2.11: Illustration of the (a) Diffraction, and (b) Image modes in TEM Imaging [58].

The produced image can be viewed in two different ways; a viewing screen, or via camera. Certain TEMs employ a fluorescent viewing screen to allow the user to see the produced image inside the TEM when viewed though a shielded glass window. This is done through the use of a Phosphor coated Aluminium plate which emits light when excited due to electron collisions. This light appear in both light and dark contrast corresponding to the electron intensities on the screen thus forming an image of the sample [59, 60]. This image however cannot be captured digitally, to do this a special camera is used known as a *Charge-Coupled Device* (CCD) consisting of an array of Metal-Insulator-Silicon devices called *Potential Wells*. In a CCD, a single potential well corresponds to one pixel in an image and hence, depending on the resolution, a single CCD can contain millions of individual potential wells. To form an image, these potential wells store a charge corresponding to the number of electron collected during exposure. Each row is then shifted to a parallel register where the pixels are read one by one before the next row is shifted and read. A corresponding image can then be digitally generated where the intensity is a function of the charge read by the register [50, 61].

Image Mode

As previous mentioned, a TEM operating in TEM mode has two primary imaging functions, the first of which is *Image mode* where an image of the sample itself is produced. This is achieved by adjusting the first intermediate lens so its object plane is the image plane of the objective lens [50]. In this mode two forms of image can then be generated; a Bright-Field Image, and Dark-Field Image, each of which will be described in the following sections.

Bright-Field (BF) Imaging

In image mode, Bright-Field imaging is the most common form of imaging where the objective aperture is centered around the optical axis thus only allowing the direct beam and low angle scattered electrons to pass through. In this form of imaging the unscattered (transmitted) electrons reflect the mass and crystallinity of the sample where high mass and crystalline areas will appear darker and low mass and amorphous areas will appear brighter [51, 62]. Since, in TEM mode, the local contrast is proportional to the number of electrons striking the viewing screen or detector, in BF imaging contrast between smaller and/or low mass crystalline features can often become an issue. In this case it is often necessary to adjust the image contrast in post-image processing to realise drowned-out features [62, 63]. This is not always useful however, if features are not visible whilst capturing the images themselves, in which case it can often be more beneficial to capture images in the Dark-Field. An example comparison of Bright-Field and Dark-Field images of tissue paper is shown below in Figure 2.12.

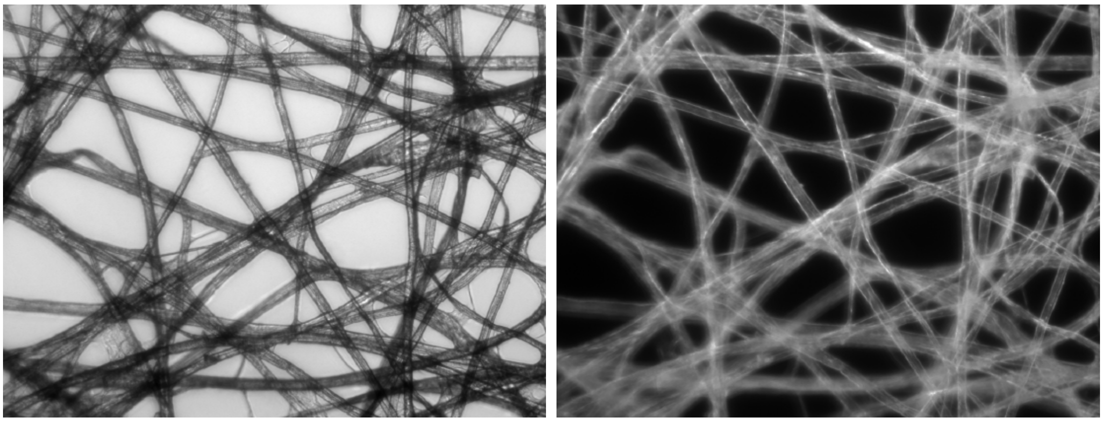
(a) (b)

Figure 2.12: Example a) Bright-Field, and b) Dark-Field TEM image of tissue paper [62].

Dark-Field (DF) Imaging

In contrast, the other form of image in TEM image mode is Dark-Field imaging. Here, unlike Bright-Field imaging, the objective aperture is positioned off axis. As a result, the direct beam is blocked and only one or more of the Bragg-diffracted electron beams are allowed to pass. Similar to BF imaging, in the Dark-Field the mass and crystallinity of the sample is also reflected however, due to the exclusion of the direct beam the contrast is reversed. In the Dark-Field crystalline and higher mass areas are instead brighter and amorphous and low mass areas are darker [51, 62, 64]. Due to the reduced selection of electrons by the removal of the direct beam, contrast between sample features is improved however, this can also be a limiting factor depending on the type of sample being imaged. Image intensity and contrast can be somewhat improved in Dark-Field imaging by adjusting the size of the objective aperture and thus adjusting the number of diffracted electrons allowed to pass to the viewing mechanism. In general, image intensity can be improved by increasing the objective aperture size and image contrast can be improved by decreasing the objective aperture size. As a result, obtaining the desired image in the Dark-Field is often a balance between objective aperture size and position whilst also being sample dependent [50, 62, 64].

Diffraction Patterns and Power Spectrums

Diffraction patterns are an additional form of data obtained directly during TEM imaging and used to further determine the structural characteristics of a sample through the use of the Selected-Area-Diffraction aperture and setting of the intermediate lens to focus on the Back-Focal-Plane of the objective lens [50]. The use of these patterns can tell us whether a sample is crystalline or amorphous, for example if spots are seen on a diffraction image, then a sample is said to at least partly crystalline whereas blurred diffraction rings indicate an amorphous structure [50, 65]. In a crystalline structure this can indicate its specific crystallographic properties e.g., lattice parameter, and symmetry, as well as other structural characteristics [50]. Furthermore, the distance that these spots and rings appear from the central peak can also be used to determine the interplanar spacings of the sample, for example the distance between walls in carbon nanotubes. In contrast there is also Power Spectrum images which can be obtained indirectly with a Fast Fourier Transform of a TEM image using processing software. This form of diffraction image however, relies heavily on the resolution and focus of the original TEM image where astigmatism and defocus can affect the symmetry of the rings. As a result, precise structural measurements through this method are less reliable than from direct diffraction images. This limitation is also beneficial in TEM imaging where use of the power spectrum during imaging assists in the realisation and correction of astigmatism and defocus in a TEM image, thus allowing for the capture of higher quality images [66].

2.2.4 STEM Imaging

Scanning Transmission Electron Microscopy represents the best of both worlds as this technique combines both SEM and TEM, and can be performed on either instrument operating in STEM mode. Similar to SEM, a finely focused beam of electrons is scanned in a raster pattern over a sample generating a signal from interaction between electrons and the sample atoms [67]. The combination of both SEM and TEM techniques allows for a wide variety of signals to be generated such as electron scattering, Energy-Dispersive X-ray Spectroscopy, and Electron Energy-Loss Spectroscopy, allowing for in depth investigations of sample materials [55, 67]. These signals are collected by specialised detectors for analysis, this data is then used to virtually construct an image of the sample [67]. In standard STEM imaging however the resolution is limited and due to aberrations in the electron beam, and atomic resolution is not possible. For atomic scale resolution imaging, a corrector is required. In this section, the different types of obtainable STEM images will be described in addition to the requirements for Aberration-Corrected STEM (AC-STEM), which was used in this thesis, and its benefits.

STEM Image Formation

When operating in STEM mode, the selected area of the sample is exposed to a small convergent beam in sequence. As the name suggests, in this mode the convergent beam is scanned across an area of the sample to produce an image. The scanning effect in this method is achieved through the use of *Scanning Coils* and *De-Scanning Coils* located before and after the sample as illustrated below in Figure 2.13 [50, 68]. The un-deflected electron beam is then passed through the intermediate and projector lenses before reaching the STEM detectors.

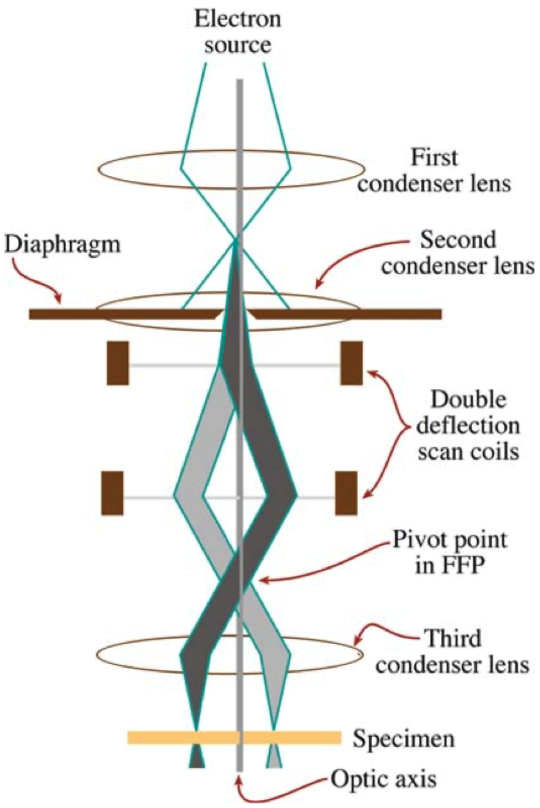

Figure 2.13: Illustration of the scanning process used in Scanning Transmission Electron Microscopy (STEM) [50].

In STEM, magnification is in-fact determined at the sample by the area the convergent beam is scanned over, i.e. a higher magnification is achieved by scanning over a smaller area and vice versa [50, 68]. Furthermore, unlike in TEM mode where one device is used to capture the final image, in STEM three detectors are used to collect information on the scattered electrons. These are the; High-Angle Annular Dark-Field (HAADF), Annular Dark-Field (ADF), and Bright-Field (BF) detectors, each of which will be further detailed in the following sections. STEM mode also offers additional data collection through the use of two other forms of spectroscopy; Energy-Dispersive X-ray Spectroscopy (EDS/EDX), and Electron Energy-Loss Spectroscopy (EELS). EDS allows for the production of spectra and maps of a samples elemental composition allowing the user to understand the location and proportions of different elements within a sample. This is achieved through the detection of emitted X-rays from the sample where the X-ray energy is characteristic of the interacted element. In contrast, EELS allows for the chemical and bonding information within a sample to be determined in addition to the elemental composition.

This is done by measuring the energy loss of inelastically scattered electrons which is again related to the element it is scattered from. This form of analysis is however, extremely reliant on the incident electron beam being of the same energy or ‘Monochrome’ and hence is very sensitive to chromatic aberration [68]. STEM and its associated techniques can therefore be seen as a powerful tool in sample analysis, able to give insight into a wide variety of sample characteristics.

Imaging Modes

A TEM when operating in STEM mode, can obtain information about the sample from any of three detectors specific to the bright and dark fields of the scattered electron beam. These are the; High-Angle Annular Dark-Field, Annular Dark-Field, and Bright-Field detectors, each set to collect scattered electrons with differing angle ranges. As previously mentioned, the detection angles of the STEM detectors are determined by the camera length and thus the intermediate lenses however, are commonly a reflection of the convergent beam incident angle as illustrated below in Figure 2.14. The characteristics and resulting images from these detectors will be described in the following sections.

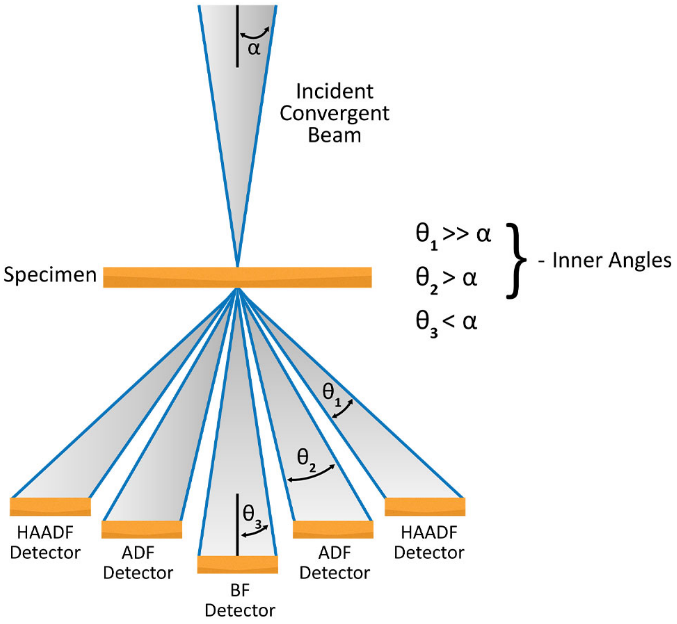

Figure 2.14: Illustration of the STEM detector arrangement and their relation to the incident angle [50].

Bright-Field (BF) Imaging

The first of the three STEM detectors is the Bright-Field (BF) detector which lies on the optical axis and like BF-TEM imaging, collects the transmitted electrons from the sample as seen above in Figure 2.14 [68, 69]. For this detector, the collection angle is typically half the angle of the incident convergent beam ($< 10mrad$) therefore acting in a similar role to the objective aperture in BF-TEM imaging. As such BF-STEM images are often comparable to BF-TEM images however, depending on the type of TEM, resolution can be improved or degraded in comparison to BF-TEM images [50, 68]. In the context of the other STEM detectors, BF-STEM is useful in determining material structures and thickness's, particularly in layered structures where material boundaries can be easily seen as demonstrated below in Figure 2.15a [69].

Annular Dark-Field (ADF) Imaging

The middle of the three STEM detectors is the Annular Dark-Field (ADF) detector however, unlike the BF-STEM detector, this detector is a ring-shaped detector that surrounds the BF-STEM detector. As a result of this, transmitted electrons are allowed to pass through this detector undetected [68, 70]. Like DF-TEM, here low-angle Bragg-diffracted electrons are collected however, due to the annular shape, more than one diffracted beam can be selected improving image contrast through better signal collection efficiency [68]. The collection angle in this form of detector, like others, can be varied by the intermediate lens strength, however common collection angles are between $10mrad$ and $50mrad$ [50]. As a result of losing the transmitted electron beam, like in DF-TEM, contrast is improved and the capture of many diffracted electron signals allows for improved contrast and easier distinction in layered samples. This can be seen below in Figure 2.15b [69].

High-Angle Annular Dark-Field (HAADF) Imaging

The third and final detector in the STEM detector set is the High-Angle Annular Dark-Field (HAADF) detector which is similar to the ADF-STEM detector only larger to collect electrons scattered through a higher angle ($> 50mrad$). Here the electron signal collected by this detector is dominated by Elastically scattered electrons (Rutherford scattering) which originate from electron interaction with atom nuclei [51, 68, 71]. As a result, HAADF-STEM image contrast is very sensitive to the atomic number of interacted atoms hence, HAADF-STEM imaging is also known as *Z-Contrast* imaging. Here heavier atoms appear brighter and lighter atoms appear darker where, the HAADF contrast is dependent on Z^2 which also facilitates atomic-resolution imaging [68, 71]. As a result, in HAADF-STEM imaging the contrast is also reversed in comparison to BF-STEM and ADF-STEM as demonstrated below in Figure 2.15c.

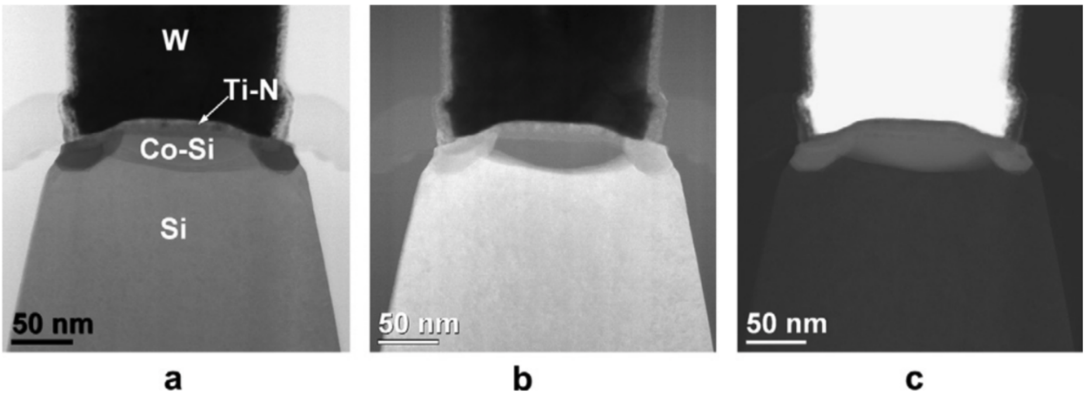

Figure 2.15: Comparison of a STEM image of a W/TiN/Co-Si/Si stack. a) BF-STEM, b) ADF-STEM, c) HAADF-STEM [72].

AC-STEM

Aberration-Corrected Scanning Transmission Electron Microscopy (AC-STEM) is a further sub-category in STEM imaging where the operating principle is the same however an extra lens is added to correct for spherical aberration as demonstrated in Figure 2.10a. This can be achieved in one of two different ways; pre-field, and post-field where the former is the preferred method due to it being significantly cheaper [73]. Such correction is achieved through the inclusion of electrostatic and magnetic *Quadrupoles* and *Octupoles* between the C2 and objective lenses arranged in sequence as demonstrated below in Figure 2.16 [74, 75]. The correction of spherical aberration allows for the production of a much finer beam spot size at the sample through the focussing of all electron rays onto the same point, in turn allowing for increased and atomic resolution on the scale of sub 0.1 nm whereby the full electron intensity can be positions a specific atomic columns [73, 76–78]. In total this can improve the STEM resolution by 2.5x and a beam current increase by as much as 10x [74].

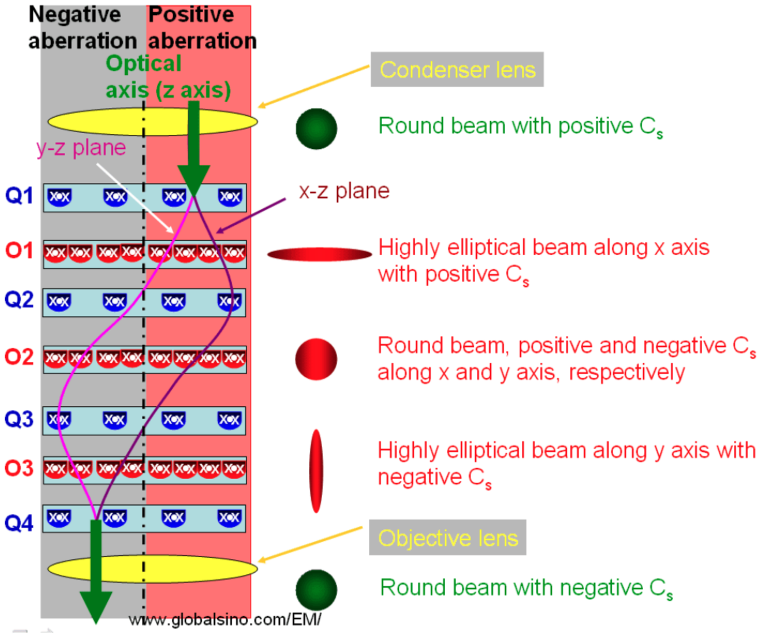

Figure 2.16: Illustration of the arrangement of Quadrupoles and Octupoles for the correct of Spherical Aberration [75]

2.2.5 TEM vs STEM and its use in this Thesis

TEM and STEM/AC-STEM are all techniques used for high-resolution imaging of nanoscale structures however, each technique has its own specialisation. As previously described, HRTEM uses a broad parallel beam to view and image a sample, whilst STEM uses a focused convergent beam to scan an area of a sample in a raster pattern. The variation in method here often means the technique used is determined by sample feature size and data trying to be obtained [50, 79]. In example, TEM's broad parallel beam is useful in imaging large areas and samples with large feature sizes where specific chemical analysis is not important however, characteristics like crystallinity and structure are. On the other hand, STEM's use of a fine focused beam allows for the imaging of smaller samples with a smaller feature size down to the atomic scale. In combination with imaging through a raster pattern, STEM also allows for complex chemical analysis through techniques like EDS and EELS [79].

In this work it was therefore appropriate to utilise HRTEM for the imaging and analysis of carbon nanotubes where sample sizes were on the micrometre scale and structural analysis was required. AC-STEM was used for the imaging and analysis of synthesised nanoclusters on the sub 5nm scale where atomic resolution imaging was needed. Details of the instruments used in this thesis are given below.

HRTEM Imaging in this Work

Imaging of produced carbon nanotubes in this thesis was carried out at Swansea University using the ThermoFisher Talos F200X Transmission Electron Microscope. This piece of equipment is a high-resolution non-aberration corrected Transmission Electron Microscope capable of providing a HRTEM resolution of 250 pm, and HAADF-STEM resolution of 160 pm [80]. In addition, the ThermoFisher Talos F200X Transmission Electron Microscope can magnify up to 630 kx in TEM mode and up to to 230 Mx in STEM mode, thus allowing for high quality nano-scale imagery [80]. This device is shwon below in Figure 2.17.

Figure 2.17: Illustration of the HRTEM imaging device used in this thesis; FEI/Thermofisher Scientific Talos F200X Electron Microscope located at Swansea University [80].

STEM Imaging in this Work

Imaging of synthesized clusters in this thesis was carried out in the Electron Physical Sciences Imaging Centre at Diamond Light Source by Dr Thomas Slater using the JEOL ARM300CF Electron Microscope. This piece of equipment is an atomic resolution imaging device with aberration correction capable of providing a High Angle Annular Dark Field Scanning Transmission Electron Microscopy (HAADF-STEM resolution of 78 pm [81]. In addition, the JEOL ARM300CF Electron Microscope can magnify up to 150 Mx in STEM mode, thus allowing for high quality atomic scale imagery [81]. This device is shown below in Figure 2.18.

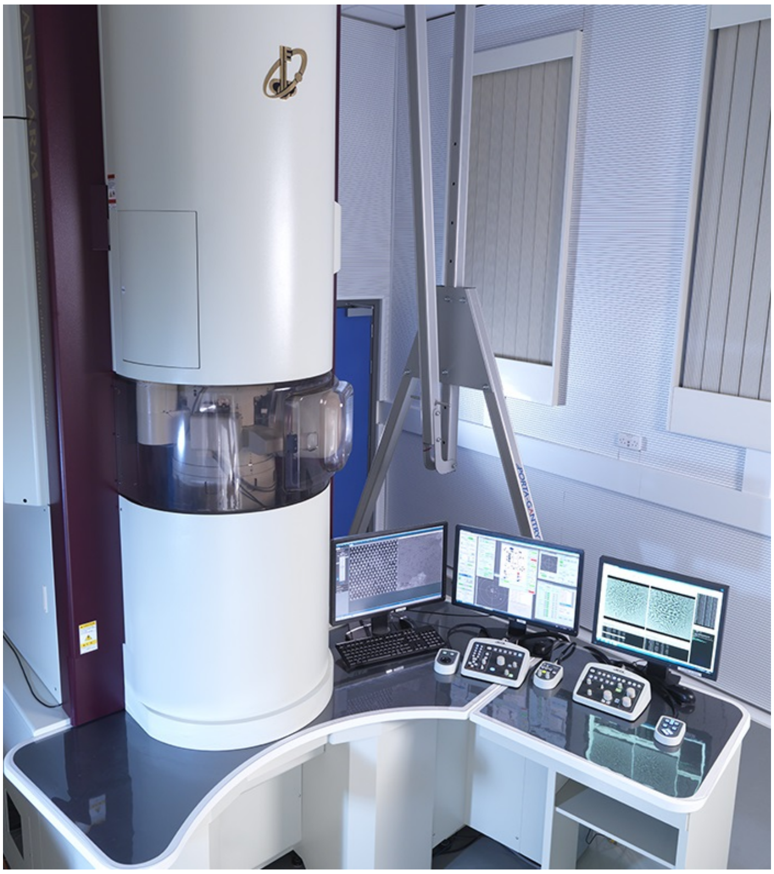

Figure 2.18: Illustration of the AC-STEM imaging device used in this thesis; JEOL ARM300CF Electron Microscope located at Diamond Light Source in Harwell [82].

Chapter 3

DEVELOPMENT OF A NEW CLUSTER SOURCE PLATFORM FOR THE FUTURE

Overview

In this chapter the topic of Nano-cluster production will be introduced in the context of a Caesium Sputtering Negative Ion Cluster Source. In this chapter the operation and design of this cluster source will be described, in addition to the apparatus revitalisation. Furthermore, the performance characteristics will be analysed and discussed in the form of Mass Spectra, as well as nano-cluster depositions. Spectrum investigations will include both atomic mass and broad cluster mass spectra.

3.1 Caesium Sputtering Negative Ion Cluster Source

This section of the chapter will look to introduce the Caesium Sputtering Negative Ion Cluster Source. This will include a general overview of the cluster source, principle of operation, and explanations of the cluster source stages and components.

3.1.1 Cluster Source Overview

The Caesium Sputtering Negative Ion Cluster Source is an example of a Physical-Vapour-Deposition (PVD) method that employs a sputtering mechanism to generate a beam of ionised single atoms and atomic clusters. The term Caesium Sputtering Negative Ion Cluster Source is used to describe the entire apparatus as a whole which itself comprises of four stages, each of which will be described in detail later in this chapter. These stages are: the Caesium sputtering stage, Beam tuning stage, Mass selection and ion deflection stage, and lastly the deposition stage. The source as a whole is maintained and operates at high vacuum, in the ranges of x10^{-5} to x10^{-7} mbar. As illustrated below in Figure 3.1, the Caesium Sputtering Negative Ion Cluster Source utilises multiple stages and elements to produce, tune, size-selected, filter, and then deposit ions onto or into a sample substrate. Each stage and element will now be further described to understand its purpose in the system as a whole.

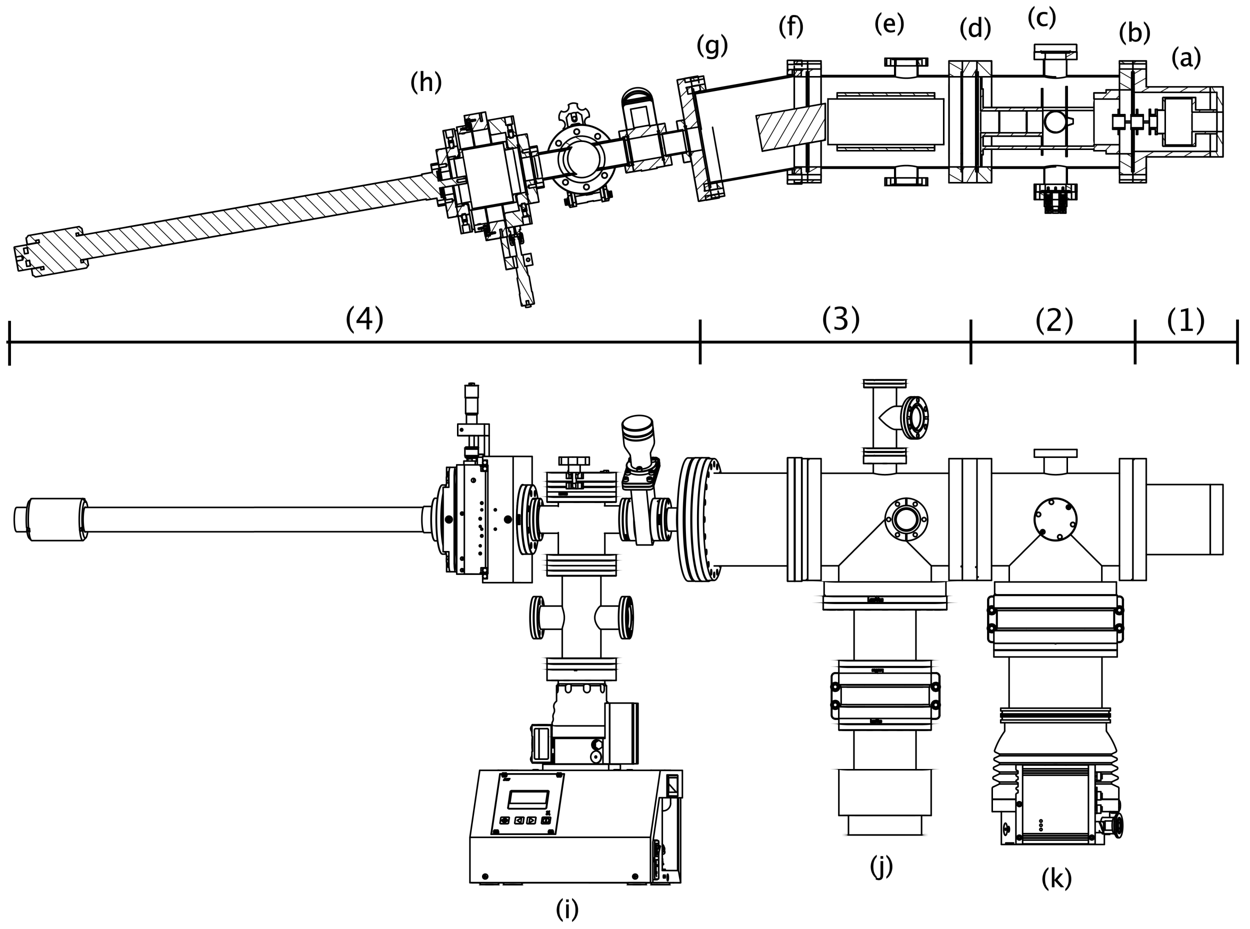

Figure 3.1: Schematic diagrams, bottom and side view, of the Caesium Sputtering Negative Ion Cluster Source. Operating right to left. The cluster source can be separated into four stages; (1) Caesium Sputtering Stage, (2) Beam Tuning Stage, (3) Mass Selection and Ion Deflection Stage, (4) Deposition Stage. The key elements of the cluster source are highlighted as follows; (a) Caesium Sputtering Cluster Source, (b) Primary Einzel Lens, (c) Primary Beam Skimmer and Secondary Einzel Lens, (d) Secondary Beam Skimmer, (e) Wien Velocity Filter, (f) 10° Deflector, (g) Deposition Area, (h) Sample XYZ Axis Motion and Manipulation, (i) Load Lock with 80l/s Turbomolecular Pump, (j) 200l/s Turbomolecular Pump, (k) 700l/s Turbomolecular Pump.

3.1.2 Caesium Sputtering Stage

The Caesium sputtering stage of the system refers to the initial section of the system where the cluster beam is produced. This stage itself has three main sections: Caesium evaporation, ionisation, and sputtering.

Principle of Operation

The principle of operation for this stage can be summarised in the following; Caesium is evaporated from a reservoir or oven to produce a vapour which is fed into the sputtering chamber. Here it comes into contact with a porous tungsten surface ionizer heated to approximately 1100°C, the critical ionisation temperature for caesium, which produces Caesium cations. Once ionised, these Caesium cations are attracted to a negatively biased target material initiating sputtering. The sputtered material consists of both atoms and anions which form a beam with kinetic energy corresponding to the bias applied to the target material [83]. This is extracted through a 4mm aperture in the centre of the ioniser assembly. A detailed diagram of the Caesium sputtering stage is shown below in Figure 3.2.

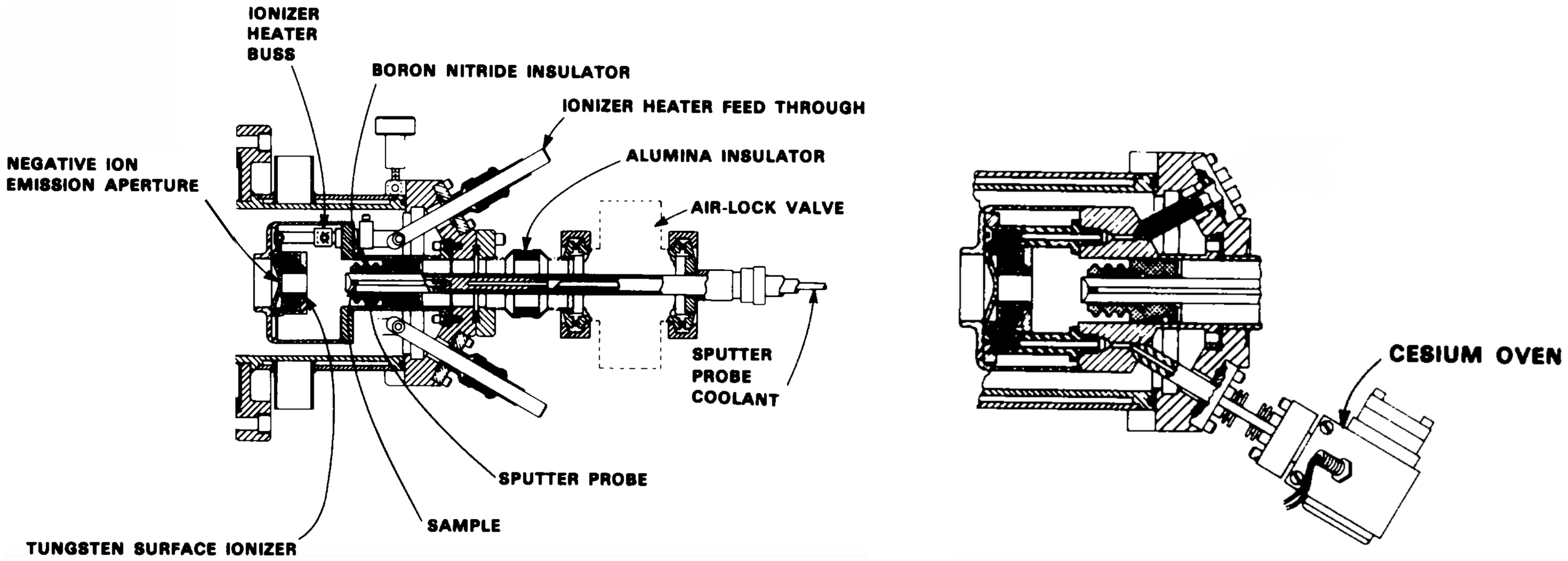

(a)

(b)

Figure 3.2: Detailed view of the Caesium sputtering stage of the Caesium Sputtering Negative Ion Cluster Source [84]. a) Detailed view of full Caesium sputtering stage assembly, b) Section view of sputtering area with Caesium oven.

The negative ion yields of the target material is dependent on a delicate balance between ionisation efficiency and Caesium vapour flow rate, both of which are dependent on temperature. To obtain the maximum yield it is necessary to heat the Caesium oven and ioniser to the optimum level whereby a temperature too low or too high would decrease efficiency. This is due to the work function lowering properties of Caesium [84]. In reference to the sputter target, it is optimal to maintain a monolayer coverage of Caesium on the surface of the target to increase the likelihood of ejected particles having a negative charge by lowering the work function of the target material. However, large amounts of Caesium counteract this effect and begin to increase the work function to that of elemental Caesium [84]. For the ionisation process, similarly, it is necessary to maintain a goldilocks temperature of approximately 1100°C to maximise the probability of ionisation of the neutral Caesium. As before, above and below these temperatures the probability of ionisation decreases. Further to this it is also necessary to create a large gap between material work functions of the surface ioniser and the ionising species. Where the ionisation potential is less than the work function of the surface ioniser, the probability of ionisation can be said to be unity. If the ionisation potential is greater than the work function the likelihood of ionisation is less so [84]. In this design, Tungsten with a work function of 4.52eV is used as the surface ioniser material with Caesium having a first ionisation potential of 3.89eV.

Prior knowledge and understanding of these effects on the efficiency of the cluster source is also key to maintaining consistently high yields of negative ions. This is particularly important in the start-up and power-down stages of operation where, in the beginning it is necessary to evaporate off any Caesium built up on the ioniser to prevent work function lowering effects and thus decrease ionisation efficiencies. Similarly, when powering down, it is necessary to do so in such a way to minimise the build up of Caesium on surfaces whilst the source is cooling down.

Once extracted, it is necessary to employ ion focusing to maintain control of and be able to maximise utilisation of the generated ion beam. This will be discussed in the next section of this chapter.

3.1.3 Beam Tuning Stage

The beam tuning stage of this system refers to the second section of the system where the produced ion beam is tuned and characterised prior to the Mass Selection and Ion Deflection Stage. This stage has two main sections: primary beam focusing and filtering, and secondary beam focusing and filtering, each consisting of an Einzel lens and Beam Skimmer.

Einzel Lenses

An Einzel or Unipotential lens is a very basic ion focussing lens consisting of three metal electrodes in series. The operating principle behind this is that by utilising the kinetic energy of the ions travelling through the lens and the potential difference between the central and outer electrodes, ionic particles can be focussed into a narrower beam [85]. An example of this principle is detailed below in Figure 3.3.

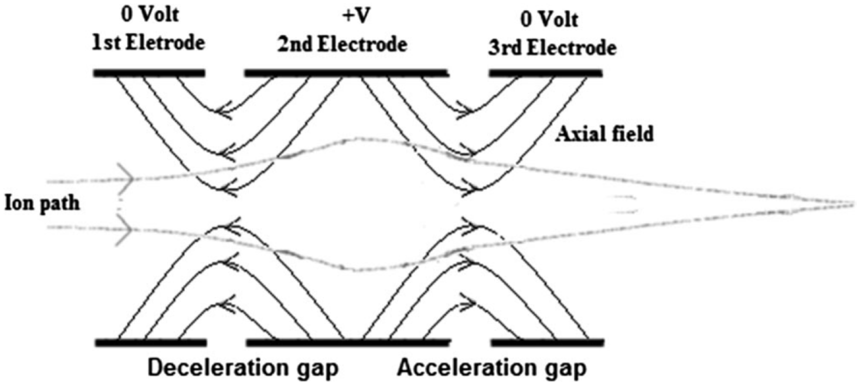

Figure 3.3: Schematic drawing of an Einzel Focussing Lens [86].

In detail this is a two stage process in which there are again two sub-stages; first a decelerating stage caused by the potential difference between the 1st and 2nd electrodes. In this stage, as the ions exit the 1st electrode they begin to decelerate axially and are pushed out radially. However, upon entering the second electrode, the radial action is reversed and the ions begin to be pulled back inwards radially, axially the ions are still decelerating however at a slower rate. The second stage of this process is the accelerating stage caused by the potential difference between the 2nd and 3rd electrodes. Continuing on from before, the ions continue to be pulled inwards radially however, they now begin to accelerate axially as they exit the second electrode. Lastly, on entering the third electrode the axial acceleration is still present though lessened, and radially the ions again begin to be pulled outwards [85]. Like optical microscopes, if the potential difference is set correctly, the desired effect is achievable. Similarly, an incorrect potential difference will result in ‘under’ or ‘over’ focusing of the ion beam. Furthermore, with an Einzel lens, if the potential difference is set too close to the kinetic energy of the ions, a reflective effect can be achieved where no ions pass through the lens.

The effectiveness of an Einzel lens is also dependent on the operating pressure and kinetic energy of the ions. Like all particles in vacuum, the higher the pressure the more collisions there will be and therefore for optimum performance, HV or UHV is preferred. The variability of ion kinetic energy is also a key factor in Einzel lens performance due to the nature of its tuning, for example when setting the potential difference for an Einzel lens, this will be tailored for an ion of certain kinetic energy. Ions with difference kinetic energies will respond differently in the lens hence performance is reduced for ion beams with high variation in ion kinetic energies [85].

In this system, two Einzel lenses are employed as shown in Figure 3.1 parts b and c. The primary and secondary Einzel lenses in this system are each designed to focus the incoming ion beam into a smaller finer outgoing beam. Here the primary Einzel lens acts as a course focusing mechanism with a short focal length whereas, the secondary Einzel lens acts as a much finer focusing mechanism with a much longer focal length. This results in a continuous parallel beam through the mass selection and ion deflection stages. Each of these Einzel lenses is followed by a Beam Skimmer, the purpose of which will be detailed in the next section.

Beam Skimmers

Beam skimmers are solid plates with conical protrusion in the centre facing the beam of which there is a hole in centre for the beam to pass through. The primary function of a beam skimmer is to filter out or cut off the edge of a beam from the main central part. This can be to remove non-axially-travelling or minority particles, collimate a particle beam, or reduce beam diameter. Depending on the skimmer design, an number of different secondary effects can also be employed including acting as a differential pumping mechanism. Differential pumping is achieved when the vacuum between two chambers is different yet the chambers are connected by a small hole small enough to prevent vacuum equalisation. This is a common secondary use for beam skimmers as the hole used is commonly only a few millimetres in diameter maximum. Examples of two types of beam skimmers are shown below in Figure 3.4.

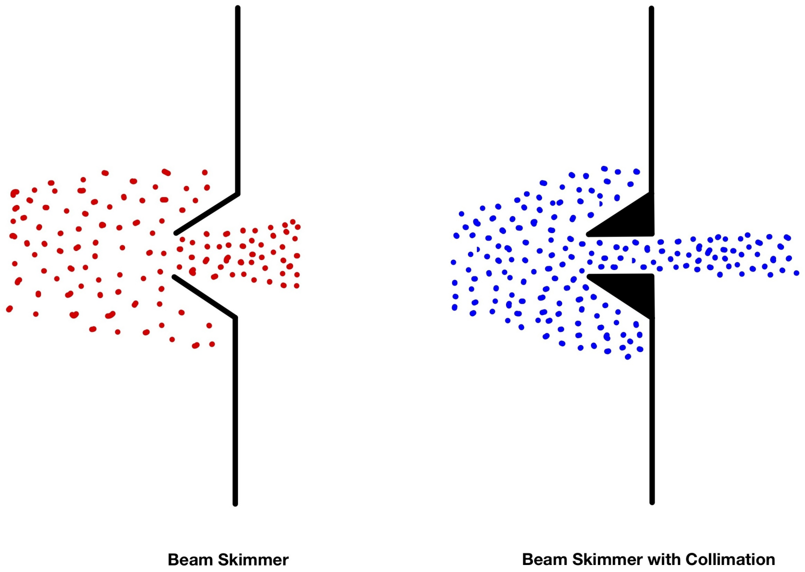

Figure 3.4: Example of Beam Skimmers designs for different purposes.

In this system, two beam skimmers with collimation are used after each Einzel lens as shown in Figure 3.1 parts c and d. The second beam skimmer between the secondary Einzel lens and Wien filter is flange mounted to provide differential pumping between the two stages and a lower vacuum in the Mass Selection and Ion Deflection stage. In both cases, the primary role of the employed beam skimmers is to remove unfocussed and non-axially-travelling minority particles. This has the effect of not only removing unfocusable particles early-on in the beam, but also preventing potential interference with the main focussed beam.

3.1.4 Mass Selection and Ion Deflection Stage

The mass selection and ion deflection stage of this system to the penultimate stage of the system where the focused ion beam can be further filtered prior to deposition. This stage has two key sections: mass selection, and ion beam deflection, comprised of a Wien Velocity Filter and Electrostatic Deflector respectively.

Wien Velocity Filter

A Wien Velocity Filter is used for the separation of charged particle beams by mass, velocity, or charge. This is achieved through the use of orthogonally superimposed electric and magnetic fields [87, 88]. A schematic view of a Wien Velocity Filter is shown below in Figure 3.5.

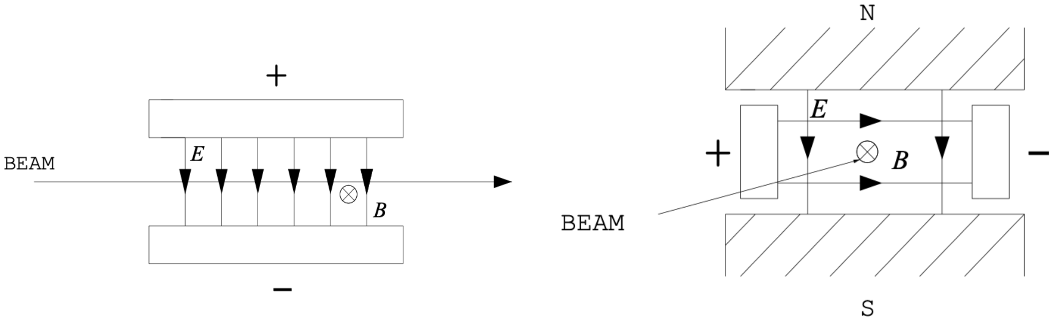

(a) (b)

Figure 3.5: Schematic view of the Wien Velocity filter a) top view, b) view from beam entrance [87].

The principle of operation for this filtering is as follows; for a beam of negatively charged particles, the electric field would deflect the beam left whilst the magnetic field would deflect the beam right. Hence, for a particle to pass through the filter un-deflected, a condition must arise where the Coulomb force is equal to the Lorentz force being applied. This principle can be utilised for mass selection in a mixed mass beam through the knowledge that particles with different masses experience a stronger or weaker deflection depending on the mass. This is demonstrated in Equation (3.1) [87–89].

$$\begin{gathered} Magnetic\ Force\ F_B = Bqv, \qquad Electrostatic\ Force\ F_E = Eq \\ where\ v = \sqrt{2q\frac{V}{m}} \end{gathered} \tag{3.1}$$

$$M = 2qV(\frac{B}{E})^2 \tag{3.2}$$

By rearranging these equations, a specific mass of particle can be filtered as shown above in Equation (3.2) [87–89]. For simplicity, either the Electric field strength (*E*) or Magnetic field strength (*B*) is often kept constant whilst the other is varied. In the operation of this filter, a constant Electrical bias was applied during operation and the Magnetic field strength was used for precise mass selection. The Electrical field strength also acts as a maximum mass limiter where a lower voltage allows filtering of a larger range of masses starting at 0 AMU [87]. The Wien Velocity filter in this system can be seen in Figure 3.1 part e.

10° Deflector

Identical to the Electrostatic deflection in a Wien Velocity filter, the 10° Deflector or Neutral Beam Dump is an assembly of two pairs of electrostatic deflection plates. These are mounted at an angle relative to the previous parts of the system as shown in Figure 3.1 part f. Similar to mass filtration, these pairs of plates are designed to remove any non-charged (*Neutral*) particles from the beam, where these would have been unaffected by previous focussing and filtering stages [90]. This is demonstrated below in Figure 3.6.

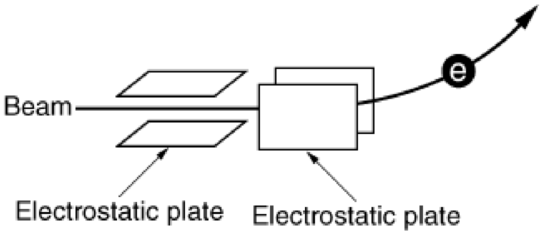

Figure 3.6: Example schematic of Electrostatic deflectors for ion beam manipulation [91].

Each pair of plates are orientated to handle a specific plane of deflection, and each plate can be individually biased to control the degree of deflection which is proportional to the applied bias [91, 92]. In this system the pairs of deflectors are ordered such that ions are first horizontal deflected before vertically deflected. During operation, the horizontal deflection plates are oppositely biased whilst the vertical deflectors receive an equal but negative bias to centre the beam prior to deposition.

3.2 Regeneration and Development of the Cluster Source

This section of the chapter will detail the improvements and additions made to the cluster source. This will include both physical additions such as the load lock stage as well as, accompanying improvements such as modelling and digitisation.

3.2.1 Digitisation

To aid in the regeneration of the the Caesium Sputtering Negative Ion Cluster Source as well as the addition of future upgrades, digitisation of the system was undertaken. This included modelling of the system in CAD as well as the ion optics in SIMION for simulation. These stages of digitisation will be detailed below.

CAD Model

The first stage of digitisation involved the production of a Computer-Aided-Design (CAD) model using *Autodesk Fusion 360*. This allowed the refurbishment of the existing cluster system to be expedited as well as providing a foundation for future upgrades. Using measurements from the existing system, component models sourced from vacuum suppliers were modified to match those present on the system. When components could not be sourced online, custom components were designed on Fusion 360 that approximately matched those in the system. This included the cluster source stage and many of the internal optics and filters. An illustration of the final system CAD model is shwon below in Figure 3.7.

The production of such a CAD model greatly improved the efficiency of the regeneration, allowing for easy visualisation of both the internal and external structure of the system for both restoration and illustration purposes. This in turn allowed for further efficiency when designing and sourcing new or replacement components, where design files could be sent to a supplier thus expediting ordering processes. Such modelling was particularly useful in the case of custom components such as ceramic insulators used in the cluster source stage. A full CAD model of the main system then allowed for the design of more complex upgrades such as the Load Lock, as will be shown in the next section.

Figure 3.7: Illustration of the Full CAD model for the Caesium Sputtering Negative Ion Cluster Source

SIMION Modelling

The second stage of digitisation of the Caesium Sputtering Negative Ion Cluster Source involved the modelling of the initial cluster source stage and ion optics. To do this, the simulation program *SIMION* was used in which, the trajectories of charged particles can be modelled in electric and magnetic fields [93]. In this software the sputter target, ionizer as well as, the primary and secondary einzel lenses were modelled allowing for the simulation of the initial ion optics stages of the system. An example of one of these simulations is shown below in Figure 3.8.

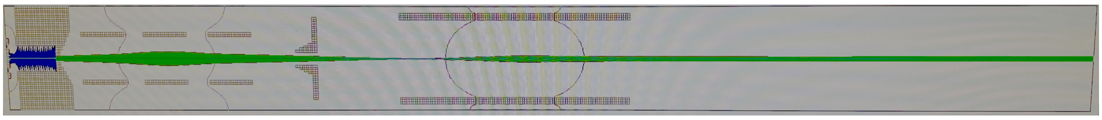

Figure 3.8: Example beam profile model for the source and ion optics stages in the Caesium Sputtering Negative Ion Cluster Source produced using SIMION.

Modelling of the initial stages of the cluster system in this way allowed for not only a visual representation of what was happening inside the vacuum system but also improved efficiency in system tuning. The use of SIMION allowed for initial values for einzel lens biases to be found, where the optimum beam profile at the exit of the ion optics stage was a long, small diameter, parallel beam. The final tuning could then achieved by hand to maximise the beam current at the end of the system. This proved to be particularly useful where multiple materials were used, which inherently required different ion optics tuning due to variation in charged particle masses.

3.2.2 Deposition Stage Development

As part of the regeneration of this system, the existing deposition stage required upgrading. Here the design of the new deposition stage will be described. This will include a breakdown of the various components that form the deposition stage of this system.

Load Lock

Prior to the installation of the upgraded load lock, the Caesium Sputtering Negative Ion Cluster Source had a small chamber by which a linear translator could move small samples, such as TEM grids, into and out of position. Furthermore, this area was not separated from the main system meaning that to remove and change samples, the entire system required bringing up to atmosphere. This proved to be very inefficient and prevented deposition onto larger samples and as a result, a new larger load lock was designed the would allow for sample changeover without venting of the full system as well as deposition onto larger samples if necessary. To do this, the CAD software *Autodesk Fusion 360* was used as in the production of the main system CAD model. The resulting finished product and design are shown below in Figure 3.9.

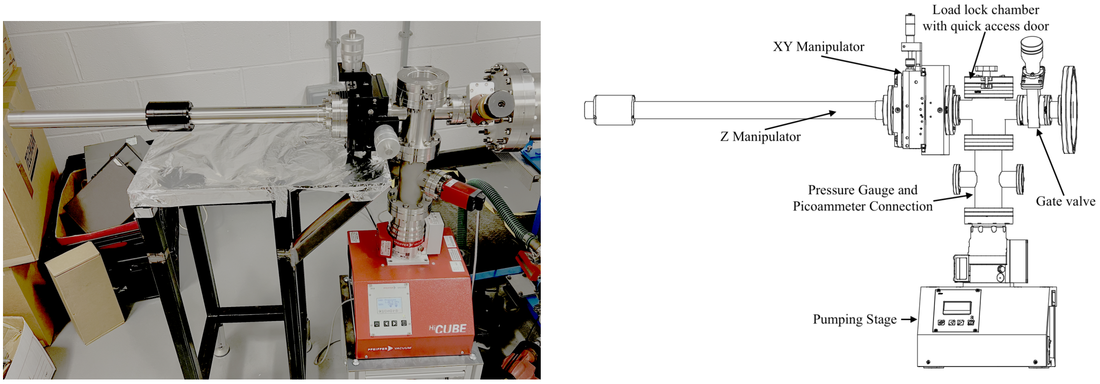

(a) (b)

Figure 3.9: Illustration of the Caesium Sputtering Negative Ion Cluster Source upgraded load lock; a) Photograph of the finished load lock, b) Schematic drawing of the load lock.

The full load lock assembly can be separated into two main parts; the load lock chamber and pumping stage, and the motion and manipulation stage. As shown in Figure 3.9b, the load lock and pumping stage can be separated into three main components; the pumping stage, the pressure stage and picommeter connection area, and the main load lock chamber. The pumping stage used here consists of a Pfeiffer Vacuum HiCube Eco pumping station in which a backing pump and small turbomolecular pump are enclosed. Above this is a DN63CF cross linking the pumping stage and main load lock chamber together as well as, providing 2x DN40CF ports for mounting of the Pirani/Cold-Cathode pressure gauge and Picoammeter feedthrough connection. At the top is another DN63CF cross which is used as the main load lock chamber. Here the top DN63CF port has a quick access door for easy removal of the deposition samples, whilst two DN40CF ports are positioned on the sides. These smaller side ports allow for mounting of a sample motion and manipulation stage on one side and a gate valve on the other allowing for isolation of the load lock from the main system. The addition of the gate valve allows the load lock to be vented without venting the rest of the system, whilst a larger load lock chamber allows for the accommodation of larger samples up to 24mm x 24mm. These new features therefore solve the issues presented in the previous sample stage.

As previously mentioned, the new load lock also includes a sample motion and manipulation stage consisting of a ±15mm XY manipulator and 500mm Z translator as shown above in Figure 3.9. The addition of both of these stages allow for samples to not only be inserted but also for the ion beam to deposit clusters in specific areas. As it will be shown later, this allows for depositions onto multiple small samples or alternately, different areas of one larger sample.

Sample Holder and Beam Current Measurement

To be able to utilise the new sample motion and manipulation stages in the load lock, a custom sample holder had to be made onto which samples could be mounted. The end of the Z translator arm consists of a 6mm female thread and as such a simple holder was designed on CAD that could mount to this thread. Designed for vertically mounted samples, the produced Teflon holder can accommodate a single 24mm x 24mm sample or smaller samples mounted using additional holders. These can all me attached through the use of the four holes shown in the four corners of sample holder in Figure 3.10a.

(a) (b)

Figure 3.10: Illustration of the a) main deposition sample holder and b) deposition sample holder configured with OFHC Copper for beam measurement.

When measurement of the overall beam current was required, a Oxygen-Free-High-Conductivity Copper plate was attached to the holder as shown in Figure 3.10b. This in turn was connected to a Keithley Model 6485 Picoammeter though the BNC electrical feedthrough previously described. The inclusion of this feature allowed for the measurement of both mass-selected and non-mass-selected beams at the deposition point, further allowing for mass spectrum's to be carried out at this point in the system.

TEM Grid Sample Holder

One of the main uses of this cluster source was to be able to deposit onto TEM grids which are inherently very fragile. As such a custom holder was designed through CAD and fabricated so that multiple grids could be mounted and deposited on, as shown in Figure 3.11. The designed holder is comprised of two pieces; the backing plate and locking plate shown in Figure 3.11a and b respectively. The backing plate consists of five slots where TEM grids can be mounted, into which the locking plate fits to lock the samples into place. Sandwiched together the to plates can the be screwed to the Teflon sample holder with the locking plate facing outwards towards the incoming ion beam. From here, the individual samples can then be placed in front of the beam via the XY manipulator therefore allowing for multiple samples to be produced in a single deposition session. Afterward the sample can then be easily removed and stored ready for imaging under TEM.

(a) (b)

Figure 3.11: CAD designs of the TEM grid sample holder a) backing and b) locking plates.

The ability to utilise custom sample holders here allows for a wide range of sample types and sizes to be used. This in turn allows the Caesium Sputtering Negative Ion Cluster Source to be potentially utilised for a variety of different applications.

3.3 Experimentation and Results

This section of the chapter will present the experimentation and results carried out using this cluster source. This will include Mass Spectra investigations, and Cluster deposition experiments.

3.3.1 Performance Evaluation

To evaluate the performance of this cluster source, mass spectroscopy was employed. This was carried out in two approaches; Mass Spectra covering the range of masses included in the periodic table (1-300 AMU), and Cluster Spectra covering a range of mass corresponding to the max mass of the clusters being investigated. Each was taken pre and post deflection. For this cluster source, performance was investigated using Silver as a target material.

Mass Spectra

In the first stage of performance analysis, beam scans were carried out over a mass range covering that of the periodic table (1-300 AMU). To do this, the electrical bias across the Wien Mass Filter was set to 129V so that the maximum magnetic field strength corresponded to a mass of approximately 297 AMU. In this analysis, mass spectra was taken at two points; pre and post 10° deflection, where the deflection skimmer plate and deposition sample holder were used as collection points respectively. The results of this analysis is shown below in Figure 3.12.

Beam current measurements taken without deflection are illustrated below in Figure 3.12a. Here, results are characterised by Gaussian peaks centred around specific masses. It is worth noting that broad peaks are demonstrated here for two reasons; firstly, due to the aperture at the exit of the Wien filter being large thus reducing selectivity and secondly, due to the heating of the Wien filter magnets as they are used thus reducing magnetic field strength. The later of these is most pronounced at higher masses where larger currents are used to drive the magnets thus increasing magnet temperature. Results initially demonstrate multiple peaks at masses between 10 and 60 AMU corresponding to clusters of Carbon upto four atoms in size with current measurements at 1.5nA, 1.0nA,0.9nA, and 0.45nA respectively. In addition to this, a hidden peak at 28 AMU with a current measurement of approximately 0.35nA is also identified which can be assumed to be Carbon Monoxide, a common contaminant in vacuum systems. Above this, the next distinct peak is centred at approximately 107 AMU corresponding to single Silver ions with peak current measurement of 0.8nA. The presence of a clear peak here provides evidence the cluster source is operating and producing an ion beam containing Silver ions. Above this, smaller peaks were also seen at around 141 AMU and 178 AMU which approximately aligned with clusters comprising of Caesium and Carbon. Specifically, these aligned with CsC and CsC_4. The final peak shown in this mass spectrum was a broad peak centred around 240 AMU. This was suggested to be a reading for Silver Peroxide or Ag_2O_2, formed as a result of a presence of oxygen in the cluster source where Silver is known to be susceptible to oxidisation.

Analysis taken post deflection is also shown below in Figure 3.12b, where the ion beam is passed through a smaller 3mm aperture prior to measurement at the deposition holder as previously described. Here results are shown as discrete peaks at specific masses as a result of this aperture filtering. As in the pre deflection mass spectra, similar peak locations are demonstrated however with clear increases in beam current. Beam current fluctuations were often noticed during testing where repeated use within short periods was thought to contribute to this through a combination of target cleaning and components warming up and stabilising. As before, multiple carbon cluster peaks were observed at cluster sizes from 1-6 atoms. Like the pre deflection mass spectra, C_1 is shown to be the primary peak for Carbon where larger clusters quickly become less frequent. A single peak at 107 AMU was also observed corresponding to Ag_1, with a further peak at approximately 234 AMU which was identified as Silver (I) Oxide. As in the Carbon peaks, both Silver peaks showed increased beam currents of 60nA and 10nA respectively. In addition, a single small peak at 135AMU was shown which approximately aligned with Caesium. Once again this can be expected given its use in the cluster source as a sputtering mechanism.

In both mass spectra, the primary silver peak is shown to be that of Ag_1 where the peak amplitude is shown to far greater than that of other silver peaks. This leads to the suggestion that, for Silver, the main produced size of particle is a single atom and that larger clusters are rare in this mechanism.

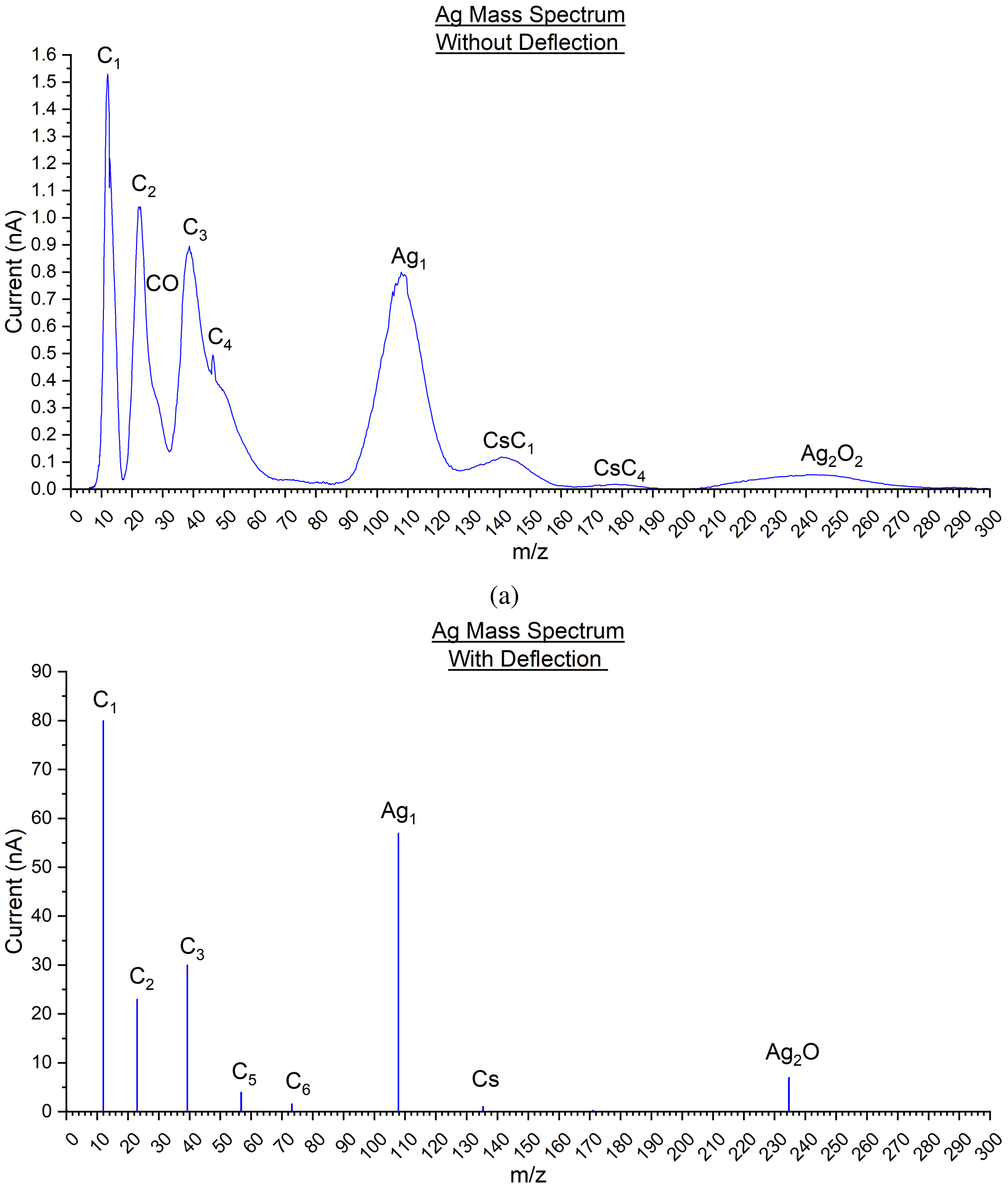

(a)

(b)

Figure 3.12: Results of mass spectra carried out using a Silver (Ag) target a) Pre 10° deflection, and b) Post 10° deflection.

Cluster Spectra

Once successful mass spectra had been carried out, the next step was to perform larger cluster spectra to ascertain what sized clusters were being produced and to what proportion. To do this the electrical bias on the Wien filter was reduced to 55V to enable a mass scan range of 1-1300 AMU, corresponding to a cluster size of up to 12 Silver atoms. As in the mass spectra, analysis was carried out both pre and post 10° deflection where the results are shown below in Figure 3.13.

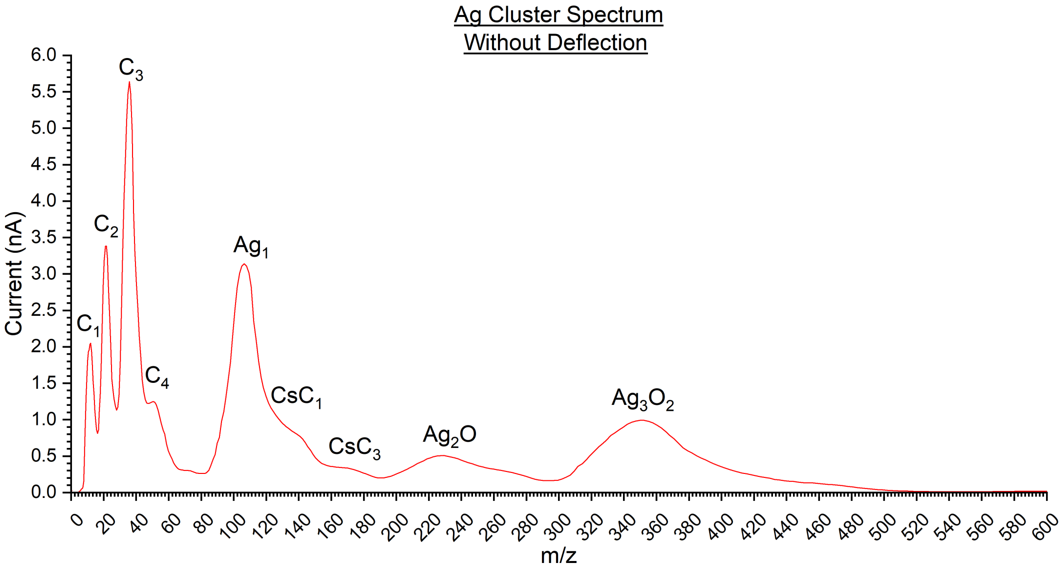

(a)

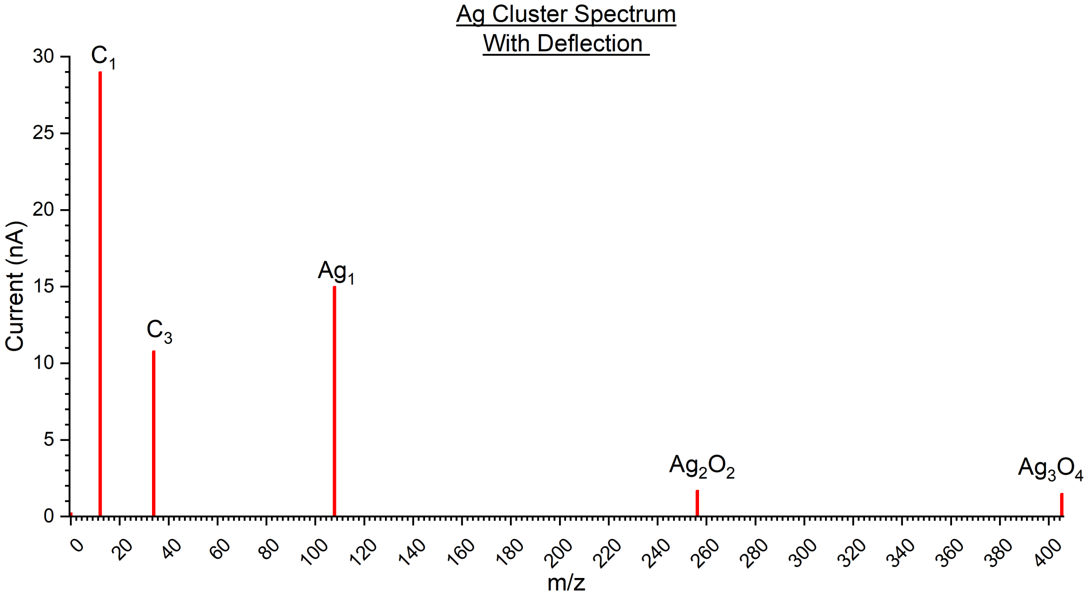

(b)

Figure 3.13: Results of cluster spectra carried out using a Silver (Ag) target a) Pre 10° deflection, and b) Post 10° deflection.

Pre-deflection cluster spectra also demonstrated a number of broad peaks centred around specific masses as shown above in Figure 3.13a. As in the mass spectra, initial peaks corresponding to carbon clusters of up to 4 atoms were identified however, here the primary peak was shown to be C_3 with a beam current of approximately 5.4nA. A strong peak for Silver at 107 AMU could also be seen with a beam current of around 3.2nA. Larger Silver clusters were shown to be oxidised however, with peaks corresponding with Ag_2O and Ag_3O_2 at approximately 230 AMU and 350 AMU respectively. Once again these larger oxidised clusters were also shown to be smaller in intensity with beam currents of 0.5nA and 1.0nA respectively. Furthermore, two hidden peaks could also be seen at around 140 AMU and 168 AMU which roughly aligned with CsC and CsC_3, again suggesting a small portion of the produced beam is containing the sputtering medium Caesium. In this analysis, no signal was observed above 500 AMU was observed suggesting that no Silver clusters larger that 3 atoms were being produced.

Post-deflection cluster spectra also yielded similar characteristics as in the mass spectra where, results were given as discrete peaks and at larger beam currents. These results are shown above in Figure 3.13b. Once again, initial carbon peaks are demonstrated at C_1 and C_3 with C_1 being the primary peak with an amplitude of 29nA. Above this no peak is observed until the primary Silver peak at 107 AMU with an amplitude of 16nA. As in previous spectra, larger Silver clusters are shown to be oxidised with small peaks being observed at approximately 257 AMU and 405 AMU which align with the Silver oxides Ag_2O_2 and Ag_3O_4. In this spectra, no Caesium peaks were observed however, it cannot be conclusively said whether this is due to the deflection stage or lack of presence within the cluster beam. Once again, no signal was observed above the final Silver peak at 405 AMU, this further suggests that no silver clusters above 3 atoms are produced.

As in the mass spectra, the cluster spectra have again shown that the primary form of Silver produced in this cluster source is a single atom, once again demonstrating that larger clusters are rare and only observable upto 3 atoms in size. Further study using other materials would however be needed to ascertain whether this is a trait of the cluster source or the use of Silver as a target material.

Comparison with Previous Work

Prior to regeneration and recommissioning, the Caesium Sputtering Negative Ion Cluster Source had been successfully operated during the mid-1990's. Papers published by Hall et al. containing examples of mass spectra using Silver as a target material, allow for performance comparisons to be made between the original cluster system and the system currently being restored.

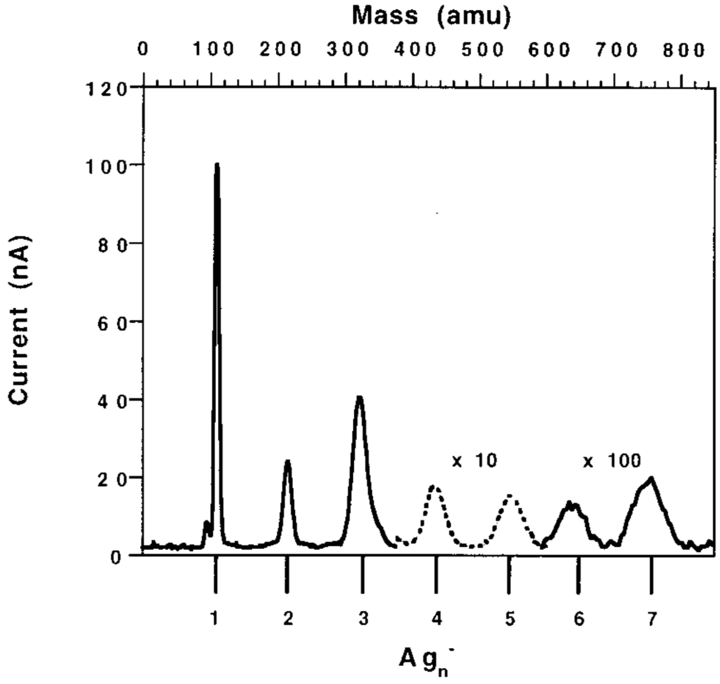

Figure 3.14: Results of Silver (Ag) Mass spectra previously carried out in 1997 using the now Caesium Sputtering Negative Ion Cluster Source [83].

Mass and Cluster spectra taken from the existing system have successfully shown the production of Silver monomers as well as, several Silver oxide compounds, Carbon clusters, and Caesium-Carbon compounds. To evaluate the systems current performance, this can be compared with a previous Silver mass spectra, shown above in Figure 3.14, taken by Dr Stuart Hall in 1997. In this spectra, Silver atoms as well as clusters ranging from 2 atoms to 7 atoms are being produced, with the primary peak being that of Ag_1 at 100nA. This is then followed by peaks for Ag_2 and Ag_3 at approximately 25nA and 40nA respectively. Larger cluster can then be seen to be present but a rapidly decreasing currents. On comparison with current mass and cluster spectra, a similar trait can be seen where the primary peak for Silver is located at the mass for a single atom. And whilst current 2 and 3 atom clusters are oxidised, a current can be identified on a scale similar to that of a single atom. This suggests that the performance of the current cluster source is not too dissimilar from that of the original system, and that while peak amplitudes are smaller they are in similar locations. Upon closer inspection of Figure 3.14 it can also be seen that there some very small peaks in the area of Carbon clusters up to 4 atoms in size. The presence of larger signals in the current mass and cluster spectra suggest that this could be simply a build up of carbon contamination in the cluster source. This can be supported by visual inspection also. A similar argument can be made for the presence of Oxygen in the larger Silver clusters where it can be reasonably suggested that this is present from either contaminants degassing or a very small leak in the cluster source area of the system.

On review, comparison with previous work has shown that the current cluster source remains operational and somewhat comparable to previous use however, minor work is still needed to fully regenerate the system to optimum working condition.

3.4 Summary

The regeneration and recommissioning of a Caesium Sputtering Negative Ion Cluster Source has been described. A breakdown of the cluster source has been given detailing the operating principle of the caesium sputtering stage as well as the roles of the forward beam tuning, mass selection, and deflection stages. As part of the regeneration project, digitisation was undertaken to produce a full CAD model of the system to expedite to restoration and aid in the design and manufacture of parts. Further to this, a SIMION model of the source stage as well as the ion optics was made to enable computer simulations of beam profiling, allowing for efficiency in operation through estimation of Einzel lens bias's. Upgrading of the deposition stage was also undertaken through design and installation of a new load lock. This allowed for the use of a wider variety of samples to be made as well as removing the need to vent the entire system for sample removal and changeover.

To evaluate the performance of the regenerated cluster source, mass and cluster spectra were carried out using Silver as a target material. Spectra were performed at two points in the system; pre-deflection and post-deflection, where pre-deflection results yielded smaller broader signals whereas post-deflection results yielded larger discrete peaks. In all cases, results showed the presence of Carbon clusters up to 6 atoms in size, Silver single atom peaks as well as, Silver oxides consisting of 2 and 3 Silver atoms. In some cases, small signals for Caesium-Carbon compounds were also shown. Of the Silver peaks, Ag_1 was shown to be the primary peak with larger silver containing clusters showing a significantly weaker current. Comparisons were made with previous work with the cluster source. The comparisons showed similar responses with Silver proportions though Silver oxides were not shown. The results of this comparison informs us that the cluster source is operational however, some work still needs to be carried out to bring it up to its previous operational level.

Chapter 4

HRTEM INVESTIGATIONS OF CARBON NANOTUBES

Overview

This chapter will present, discuss, and summarise the theory, production methods, and results of TEM investigations into Multi-Walled Carbon Nanotubes. Investigations will be split between Surface and Core structure analysis where Surface structure pertains to Carbon Nanotube lengths and diameters as well as visual observations. Core structure investigations will include wall count inspections, and interlayer spacings through FFT pattern analysis. These results are summarised at the end of this chapter as well as in Paper I: On the Use of Carbon Cables from Plastic Solvent Combinations of Polystyrene and Toluene in Carbon Nanotube Synthesis.

4.1 Carbon Nanotubes

In this section of the chapter, the concepts relating to carbon nanotubes in this thesis will be introduced. This will include: a general overview of carbon nanotubes, an introduction to their structures, production methods, types of carbon nanotubes, as well as their properties.

4.1.1 Overview

Carbon Nanotubes are large cylindrical structures formed of a hexagonal arrangement of carbon atoms [94]. They are produced through cylindrical layered sheets of graphene to form Single-Walled (SWCNTs) or Multi-Walled (MWCNTs) Carbon Nanotubes [94]. Discovered by Sumio Iijima in 1991 whilst studying the synthesis of Fullerenes using an electric arc discharge evaporation method, carbon nanotubes have quickly become a popular and well researched nanostructure for their unique and desirable properties [95, 96]

4.1.2 Structure of Carbon Nanotubes

The base structure of carbon nanotubes is a cylinder however, there are numerous different configurations that the carbon atoms in the graphene sheets can take during the bonding process. Here, the various aspects relating to the arrangement of carbon atoms and structure of the carbon nanotubes, will be described.

Graphene

Graphene alone represents and material with several useful properties ranging from electrical to optical [97]. Graphene's structure consists of carbon atoms arranged in a hexagonal lattice with each atom bonded with its three nearest neighbour atoms. This is done through hybrid s, p_x, and p_y orbital, single electron σ-bonds [97]. The formed nearest neighbour bonds are approximately 0.142 nm or 1.42 Å in length [97]. The electron remaining forms two half-filled bands through a hybridized p_z orbital orientated perpendicularly to the plane, known as π and π^*, which are responsible for the majority of Graphene's electronic properties [97]. The hexagonal structure of graphene is illustrated below in Figure 4.1.

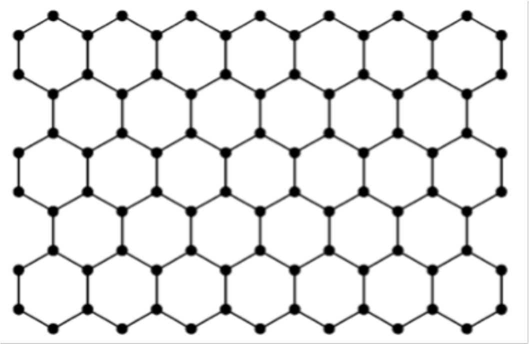

Figure 4.1: Hexagonal lattice structure of Graphene from [97]. Dots represent individual carbon atoms whilst the lines represent the covalent bonds between each atom. As mentioned, each atom is shown to bond with its three nearest neighbour atoms.

Chirality

The orientation of the hexagonal lattice in rolled graphene sheets, determine the properties of the carbon nanotube. This orientation can appear in one of three forms; Armchair, Zig-Zag, or Chiral, each with different properties [97]. These are each demonstrated below in Figure 4.2. The chiral vector of a carbon nanotube is used to determine its heaxgonal lattice structure and thus its form. This is characterised by Equation (4.1).

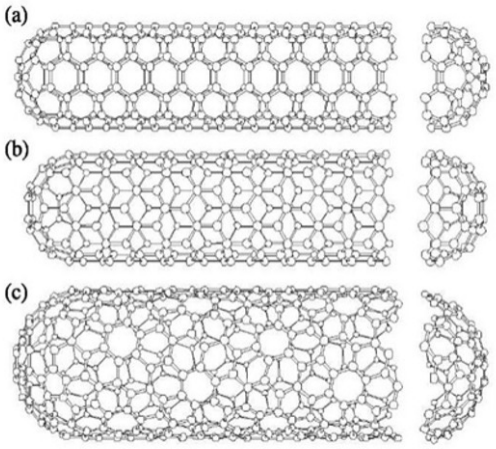

Figure 4.2: Demonstration of the three types of carbon nanotube structure, from [98]. a) Armchair SWCNT, b) Zig-Zag SWCNT, c) Chiral SWCNT. As before, dots represent the individual carbon atoms whereas, the lines represent the covalent bonds between them.

$$C = na_1 + ma_2 = (n,m) \tag{4.1}$$

where a_1 and a_2 are the basis vectors of the graphene lattice.

Through these vectors it is then possible to determine the type of carbon nanotube using the relationships: Armchair (m,m), Zig-Zag (n,0), and Chiral (n,m) [99]. Furthermore, the electronic properties of a carbon nanotube can be determined through knowing whether a carbon nanotube is metallic or semiconducting. This can be found through the relationship; Metallic if $n = m$ or $n - m = multiple\ of\ 3$, and Semiconducting when $n - m \neq a\ multiple\ of\ 3$. The chiral angle of a carbon nanotube is also useful for determining additional individual carbon nanotube properties and can be characterised by Equation (4.2) [100].

$$\theta = \arctan\sqrt{3}(\frac{m}{2n+m}) \tag{4.2}$$

Single & Multi-Walled Carbon Nanotubes

Carbon nanotubes can also be categorised by their number of layers or walls, and hence can be summarised as either; Single-Walled Carbon Nanotubes (SWCNTs) or Multi-Walled Carbon Nanotubes (MWCNTs). Single-walled carbon nanotubes contain only a single rolled sheet of graphene, capped at each end [97]. Both the sidewalls and caps of the carbon nanotube exhibit different physical and chemical properties [97]. In contrast, MWCNTs contain multiple layers of rolled graphene sheets with a layer separation corresponding to that of graphite at 0.334 nm or 3.34 Å [97]. Each of these two forms exhibit their own specific traits, in particular SWCNTs are greatly desired for their highly conductive properties, whereas MWCNTs are preferred where tensile strength and thermal stability are required [97, 101].

4.1.3 Synthesis Methods of Carbon Nanotubes

There are numerous methods for synthesising carbon nanotubes including; Arc Discharge as explored by Iijima [96]. A more common method however is Chemical Vapour Deposition (CVD). This process involves the use of a carbon source alongside a catalyst (usually Ni, Fe, or Co) at high heat (650-900°C) to separate the carbon atoms from the source and bind them to the catalyst material allowing for good control over growth parameters [97]. The CVD process is very adaptable and is often further tuned through methods such as laser-assisted CVD, or plasma-enhanced CVD [97]. In this thesis, the technique employed is an example of catalytic chemical vapour deposition using a liquid-injection-reactor as described in Section 4.1.5.

4.1.4 Properties of Carbon Nanotubes

The strengths of carbon nanotubes lie in numerous areas such as electrical, thermal, and mechanical to name a few. As previously shown, the occurance of these strengths is heavily dependent on the structure and chirality of the carbon nanotube. In particular, Collins et al. report how the conducting nature of synthesised CNTs are greatly impacted by the type of CNT produced. For example, two-thirds of produced ‘straight’ nanotubes (Armchair or Zig-Zag) are metallic, whereas two-thirds of chiral tubes are semiconducting [102]. Furthermore, the highly conductive nature of SWCNTs is owed to the zero-gap semiconducting characteristic of graphene where the conduction and valence bands meet at the Dirac point [97]. In tandem with the high thermal conductivity of graphene, this makes carbon nanotubes very popular for electronic applications [97, 102]. Benefits such as high tensile stress, chemical durability, and hollow interiors make them useful in applications such as materials, bio-sensors, and nanomedicine [103].

4.1.5 Carbon Nanotube Synthesis and Analysis

In this section, the various methods used to synthesise and analyse the Multi-Walled Carbon Nanotubes (MWCNTs) investigated in this thesis, will be described including the tools and techniques used.

Synthesis

In this thesis, carbon nanotubes synthesised by Ali Hedayati and Jainaba Sallah-Conteh were analysed. Here recycled plastics, namely Polystyrene, were explored for their potential re-use in the production of carbon nanotubes through being dissolved in a thermodynamically compatible solvent [104]. In total four samples were analysed where the synthesis method was kept the same; however, the concentration of Polystyrene in the initial solutions were varied to consist of 0, 1, 2, and 4%. The use of a varied concentration was crucial to observe trends and evaluate the efficacy of utilising recycled plastics as feedstock for carbon nanotube growth [104].

The method employed for synthesis of carbon nanotubes in this thesis is known as 'Catalytic Chemical Vapour Deposition (CCVD)', occurring in a two-zoned horizontal liquid injection reactor (LIR) [104]. In this method, carbon nanotubes were produced through injection of a Ferrocene and Polystyrene infused Anhydrous Toluene solution (1 mL/865 mg) at 5 mL/hr under a mixed gas flow of 5% Hydrogen in Argon at a rate of 1 L/min into a 100 cm long, 38 mm internal diameter quartz tube inside a two-zoned furnace [104]. The purpose of a split furnace was as follows; The first zone was designed for vaporisation of the process solution. This stage of the furnace was set to a temperature of 225°C. The produced vapour was then transported into the second zone by the mixed gas flow where the growth of the carbon nanotubes was induced at a temperature of 780°C [104]. An illustration of this process is detailed below in Figure 4.3.

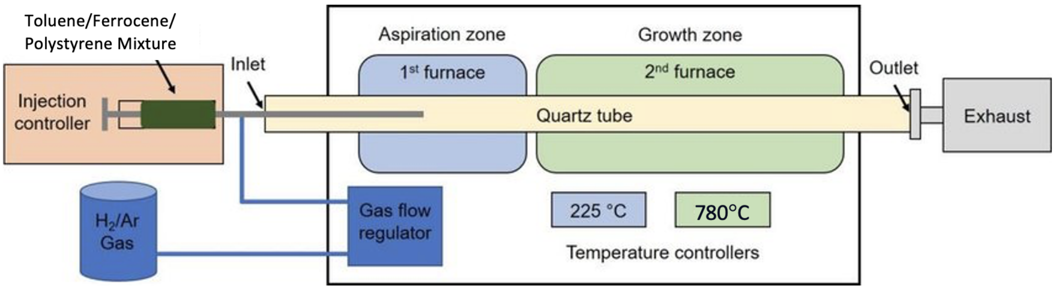

Figure 4.3: Modified example diagram of Liquid Injection Catalytic Chemical Vapour Deposition method used in this experiment after [105]. Shown is a two stage furnace used for growth of carbon nanotubes. Furnace 1 is set at 225°C and is used to vaporise the solution injected by the Liquid Injection Reactor. Furnace 2 is where carbon nanotube growth occurs and is set to the higher temperature of 780°C. A H_2/Ar mixture flows continuously throughout.

Prior to injection, the Ferrocene/Polystyrene/Toluene solution was thoroughly mixed and degassed for 15 mins using ultrasonication [104]. Once mixed, the solution was loaded into the liquid injector where the vaporisation process begins. Upon transportation into the second furnace zone, vapour droplets containing the Fe catalyst particles were deposited onto the inner wall of the quartz tube where CNT growth could occur. The higher temperature in this section of the furnace allowed for the breaking of bonds and the vaporised solution to be separated into its component elements. This allowed the carbon atoms to self-assemble into nanotubes where the Fe catalyst particle initiated growth. Once the deposition and growth process is complete, the resulting carbon nanotubes were peeled from the inner quartz tube wall and stored.

In this analysis, the stored carbon nanotubes were then deposited onto holey-carbon TEM grids by lightly 'dabbing' a TEM grid onto the carbon nanotube powder for analysis under HRTEM. In this investigation, four samples were analysed with varying concentrations of Polystyrene, as highlighted below in Table 4.1.

Table 4.1: Carbon nanotube sample solution compositions from [104]. Dosages for each component of the end sample solution are given where quantities are given in units of mass, volume, and a weight for weight percentage.

Sample ID	**Anhydrous Toluene Content**	**Polystyrene Content**	**Ferrocene Content**
T56P132 (0 wt% PS)	1mL (865 mg)	0%	5wt% w/w (45.5 mg)
T74B2P5 (1 wt% PS)	1mL (865 mg)	1wt% w/w (8.75 mg)	5wt% w/w (46.0 mg)
T72B2P5 (2 wt% PS)	1mL (865 mg)	2wt% w/w (17.5 mg)	5wt% w/w (46.5 mg)
T82B2P18 (4 wt% PS)	1mL (865 mg)	4wt% w/w (35.0 mg)	5wt% w/w (47.5 mg)

Imaging using ThermoFisher Talos F200X TEM (Swansea University)

Imaging of the grown carbon nanotubes was carried out using the ThermoFisher Talos F200X Transmission Electron Microscope at Swansea University as previously detailed. TEM grids were prepared by dipping into the vials containing carbon nanotubes. The TEM grids were then air sprayed to remove large particulates, leaving only carbon nanotubes on the holey-carbon film. Samples were then imaged in TEM mode using a Ceta 16M camera at an accelerating voltage of 200 kV [80]. Imaging was carried out at various magnifications ranging from 5.5 kx to 630 kx to produce a variety of images where effective investigation of the carbon nanotubes length, diameter, number of walls, and consistency could be carried out using the image processing software Fiji/ImageJ.

Analysis in Fiji/ImageJ

Analysis of carbon nanotube properties from images captured under HRTEM was carried out through image processing software Fiji/ImageJ. This software offers a large variety of tools and packages well suited for inspecting electron microscopy images and thus analysing the properties of grown carbon nanotubes. Tools used in this investigation include line profiling and FFT transforms, as well as basic shape and measurement features. How these tools were used in this investigation are detailed below.

Structure Examination

Multi-walled carbon nanotube structure analysis included the examination of nanotube length, diameter; both overall diameter and consistency along the structure, and lastly the core structure of the nanotube and its consistency throughout the structure. Additionally, surface structure observations were also noted. Nanotube lengths were measured using the line tool in Fiji/ImageJ where a line would be drawn from start to finish corresponding to the nanotube length. Where carbon nanotubes contain abrupt structure deviations, measurements woere broken down into smaller segments in order to gain a more accurate approximation of nanotube length. Similarly, the diameter of nanotubes were determined by using the line tool across the nanotube from edge to edge. Multiple diameter readings were taken at various locations along the nanotube to account for thinning and thickening zones in the nanotube structure. Thus ensuring an accurate average diameter as well as a good approximation of nanotube diameter consistency.

In the final part of the structure examination, the internal characteristics of the nanotubes were analysed including; nanotube wall count and deviations along the structure. This was carried out using three approaches; firstly, using the line plot method where a line will be drawn from the innermost wall to the outermost wall allowing for a line plot to be created where the number of peak points, with a separation greater than 0.17 nm, would equal the number of walls in the nanotube. Secondly, using the multi-point tool, the walls in carbon nanotubes were manually counted recording the maximum number. This approach would not be possible in every image. Thirdly, using the found interplanar spacing of MWCNT layers *(0.34 nm)*, the formula shown in Equation (4.3) was applied [97, 101].

$$Approximate\,No.\,Walls = \frac{Distance\ between\ innermost\ and\ outermost\ walls}{0.34} + 1 \tag{4.3}$$

The results of these methods, where possible, were then tabulated and compared to see if a common approximation could be found.

FFT Pattern Investigation

Further investigation of carbon nanotube structure and interlayer spacing of nanotube walls, was carried out through Fast-Fourier-Transforms (FFT) of HRTEM images and image segments. The result was a power spectrum of the area being analysed, allowing for a FFT pattern to be seen [106]. FFT of whole images could be used to gain a brief understanding of the structure of the object/s within the image however, segmented FFT could be used to gain a more specific insight into the structure of the objects within the segmented area. In this case, this was the carbon nanotube walls and their spacings. For segmented area FFT, the rectangle tool in Fiji/ImageJ is used to highlight a section of a carbon nanotube from which a FFT should be produced. In the FFT image, diffraction rings and spots were shown from which the interlayer spacing could be deduced from their distance from the central spot. To do this, Fiji's peak finding tool in the 'BAR' package was used to identify to clear peaks where unwanted peaks could then be removed manually. In addition, FFT patterns could also be used to determine characteristics like a structures crystallinity through visual observations of the diffraction ring and spot strengths. For example, the presence of strong diffraction rings indicated a mostly amorphous structure, whereas diffraction spots indicated crystallinity.

4.2 Transmission Electron Microscopy Investigations

In this part of the chapter the results of investigations into Multi-Walled Carbon Nanotube structure through HRTEM imagery will be presented, discussed, and summarised. This section will be categorised into surface and core structure investigations, each exploring the relative aspects of grown carbon nanotube characteristics.

4.2.1 Surface Characteristic Investigations

In this section, the surface characteristics of investigated Multi-Walled Carbon Nanotubes will be presented and discussed. This will include length and diameter inspections as well as visual observations of carbon nanotubes in each sample.

Length

Average carbon nanotube lengths were investigated for three individual carbon nanotubes per sample. Imaging was achieved using the Thermo Fisher Scientific Talos F200X HRTEM at Swansea University as previously described. Analysis was then carried out in the image processing software Fiji/ImageJ where segmented lines were drawn along the carbon nanotubes to record overall lengths. Results of the analysed carbon nanotubes are shown below in Table 4.2.

Table 4.2: Table of lengths for carbon nanotubes from different samples. Lengths of three carbon nanotubes from each sample, measured in Fiji/ImageJ are presented in μm. The value for one standard deviation of the length per sample is also given in μm.

Sample ID	**MWCNT 1** (μm)	**MWCNT 2** (μm)	**MWCNT 3** (μm)	**Standard Deviation** (μm)
T56P132 (0 wt% PS)	10.8	1.72	1.76	5.23
T74B2P5 (1 wt% PS)	3.79	2.17	9.75	3.99
T72B2P3 (2 wt% PS)	8.13	5.08	1.21	3.47
T82B2P18 (4 wt% PS)	8.78	2.85	4.30	3.09

From this examination it could be seen that grown carbon nanotubes varied in length dramatically with some only being a couple of microns in length to others reaching over 10 microns long, as demonstrated below in Figure 4.4. This variation of length was present both across and within samples, with no immediately visible relationship between polystyrene and the length of grown carbon nanotubes. This corresponded with previous work where grown carbon nanotubes varied heavily in length [107]. Further investigation of these lengths however, did reveal a potential trend between carbon nanotube length and polystyrene content. Statistical analysis of nanotube length distribution demonstrated a decrease in length standard deviations with increasing dosage of polystyrene. This suggested that the increased concentration of polystyrene in the initial growth solution, promotes a more consistent and less distributed length growth. With the knowledge that with a increased polystyrene concentration comes an increased carbon concentration, this in turn suggests that carbon nanotube length uniformity can be influenced by the amount of carbon available. The small sample size however, could also suggest this trend is pure coincidence and as such further investigation should be undertaken to confirm this relationship.

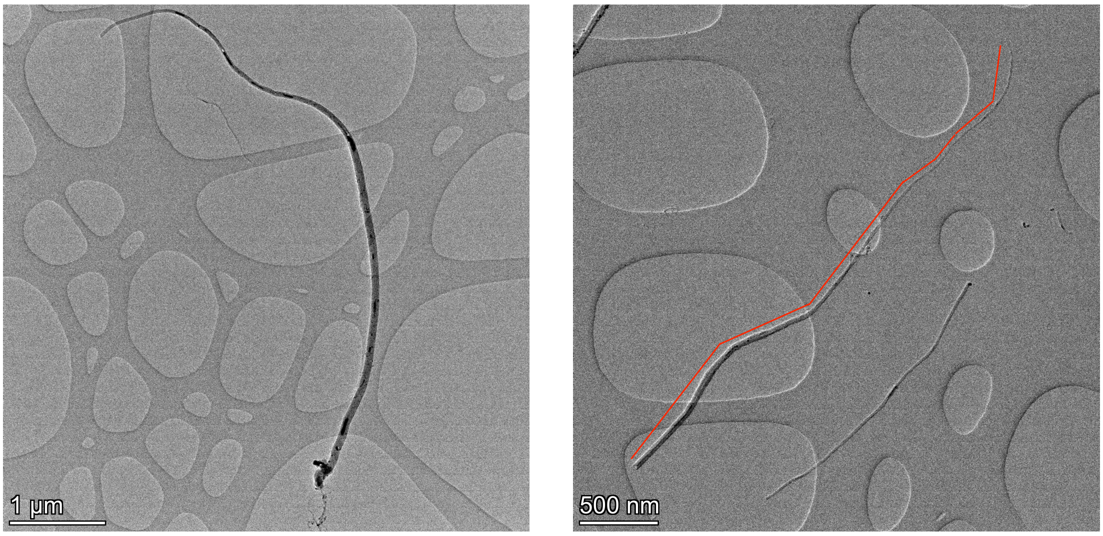

(a) (b)

Figure 4.4: HRTEM image examples of variations in carbon nanotube lengths taken from a) T56P132, and b) T74B2P5 samples. Length measurement is exampled in b).

Additional efforts to fine tune this parameter have been attempted, Tripathi et al. has demonstrated how the flow rate and duration of an Acetylene-based CVD method can be used to control and optimise the length of grown carbon nanotubes [108]. From this it could be inferred that, with further experimentation, the lengths of carbon nanotubes in this production method could be produced more uniformly by tuning growth parameters.

Diameter

Similar to length, diameter investigations were carried out for three individual carbon nanotubes per sample using analysis tools in Fiji/ImageJ. Initially, three readings were taken at quarterly points along each carbon nanotube, measuring the distance from outer edge to outer edge. The average diameter and standard deviations were then calculated and recorded. The results of this analysis are presented below in Table 4.3.

Table 4.3: Table of average diameters for carbon nanotubes from different samples. Average diameters and standard deviations for individual carbon nanotubes per sample are given in nm. A further average of average diameters value is then presented as well as the range in average diameter.

Sample ID	MWCNT 1		MWCNT 2		MWCNT 3		Overall		
	Average (*nm*)	Standard Deviation (*nm*)	Average (*nm*)	Standard Deviation (*nm*)	Average (*nm*)	Standard Deviation (*nm*)	Average Diameter (*nm*)	Range (*nm*)	Standard Deviation Range (*nm*)
T56P132 (0 wt% PS)	63	13.89	71	9.93	30	2.05	55	41	11.84
T74B2P5 (1 wt% PS)	44	3.86	77	2.87	92	12.36	71	48	9.49
T72B2P3 (2 wt% PS)	64	9.42	37	4.99	23	4.50	43	41	4.92
T82B2P18 (4 wt% PS)	63	21.23	68	23.70	111	28.08	81	48	6.85

As in the results of length investigations, the results presented in Table 4.3 suggested no intial relationship between the average diameter of synthesised carbon nanotubes and the concentration of polystyrene in the initial solution. The variation of average diameters within samples was also shown to be very dispersed with ranges in the order of 40 nm to 50 nm with a mixture of minimum and maximum points, further re-enforcing the conclusion of little relationship between polystyrene content and average diameter. In particular, sample T82B2P18 (4 wt% PS) demonstrated both a large range in average diameters as well as large variations of diameters within individual measured carbon nanotubes. Furthermore, standard deviations of diameters within carbon nanotubes were also shown to be greatly varied with deviations ranging from 2.05 nm to 28.08 nm as illustrated in Figures 4.4 and 4.5. Analysis of standard deviation ranges within samples suggested no initial relationship between polystyrene content and nanotube diameter variations. Specific analysis of sample T82B2P18 (4 wt% PS) however, demonstrated particularly high deviations of diameters within carbon nanotubes suggesting a possible negative effect of the higher polystyrene concentration. This, in combination with decreasing standard deviation ranges in lower concentration samples suggested that the presence of polystyrene in solutions aided consistency in produced carbon nanotubes, until it reached a critical concentration. As shown in sample T82B2P18 (4 wt% PS), above this critical polystyrene concentration, a negative effect occurs.

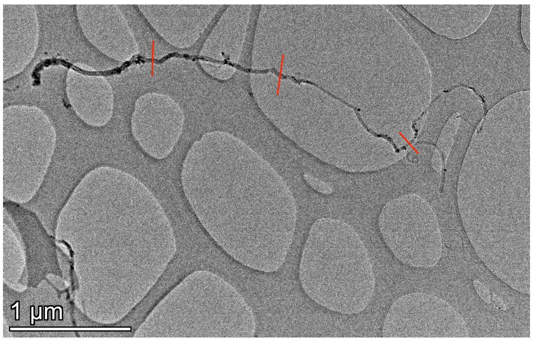

Figure 4.5: HRTEM image example of variations in carbon nanotube diameters taken from the T72B2P3 sample, illustrating the diameter measurement process.

It is possible to compare two samples against previous work: T56P132 (0 wt% PS), and T72B2P3 (2 wt% PS), where approximately 0 mg and 17.5 mg respectively is used. This could reasonably be compared with Hedayati et al. work in which carbon nanotube samples were produced with 16.5 mg of polystyrene [109]. The results of the diameter investigations in Hedayati et al. work, where analysis was undertaken through SEM studies, demonstrated carbon nanotubes with an average diameter of 30-40 nm in the control samples and 41.3 - 43.5 nm in polystyrene samples [109]. Furthermore, in Hedayati et al. experiments, the results displayed a large range for the control samples, whereas the polystyrene samples were shown to have a much more confined range [109]. The results of these were found to be closely matched with those produced in this method where the control sample average diameter is shown to be slightly larger than in Hedayati et al. work, though this could be attributed to either the small sample size here and large range shown in Hedayati et al. work or the use of SEM for analysis in Hedayati et al. work. For the polystyrene samples, the results were shown to be much more closely matched in terms of average values. This provides evidence to suggest that this method could reproduce carbon nanotubes of similar diameters.

Other work by Tripathi et al. has also demonstrated the effect of flow rate and flow duration on the final diameter of carbon nanotubes [108]. In this similar method, results have shown that increased duration and flow rate of acetylene during the CVD process tend to increase the diameter of carbon nanotubes [108]. This introduces an additional method for control of carbon nanotube diameter, however this being different from the effect on length means that control of dimensions in this way could result in a trade-off between length and diameter.

Carbon Nanotube Diameter Consistency

A breakdown of the diameter analysis allowed for further investigation of the consistency of carbon nanotube diameters. Using readings taken, the results were compared and are displayed below in Table 4.4.

Table 4.4: Table of diameter readings at different points along the carbon nanotubes. Readings of the tube diameter are recorded at three separate points for each carbon nanotube and the range in values is recorded. All values are given in nm.

Sample ID	**MWCNT 1**				**MWCNT 2**				**MWCNT 3**			
	Reading 1 (*nm*)	Reading 2 (*nm*)	Reading 3 (*nm*)	Range (*nm*)	Reading 1 (*nm*)	Reading 2 (*nm*)	Reading 3 (*nm*)	Range (*nm*)	Reading 1 (*nm*)	Reading 2 (*nm*)	Reading 3 (*nm*)	Range (*nm*)
T56P132 (0 wt% PS)	46	64	80	34	85	65	63	22	27	32	30	5
T74B2P5 (1 wt% PS)	49	42	40	9	80	73	77	7	109	81	85	28
T72B2P3 (2 wt% PS)	77	87	64	23	25	29	37	12	17	28	23	11
T82B2P18 (4 wt% PS)	89	64	37	52	48	54	101	53	149	82	102	67

From Table 4.4 and Figures 4.4 and 4.5 it could be seen that investigated carbon nanotubes exhibit varying degrees of change in diameter along the full length of the tube. The magnitude of this change however, was shown to vary dramatically amongst carbon nanotubes, even within samples. Initially, this gives evidence that the consistency in the diameter of grown carbon nanotubes is independent of the polystyrene content. It is only in the highest polystyrene concentration sample that larger variations in diameter were present as well as, larger diameter readings. As before, this could suggest that diameter variation is uneffected by polystyrene content until a critical concentration is reached, at which point the increased dose of polystyrene causes greater variation in diameters within single carbon nanotubes. For higher polystyrene dose samples, increased diamters and variation can somehwat be accounted for by the increased dose of carbon present [104]. Secondly, given the same process conditions were used on all samples, this suggests the degree in variation of diameters could also be a process related control variable where parameters like flow rate and temperature have more of an influence on this attribute. To further aid the identification of patterns in diameter consistency in carbon nanotubes, diameter ranges for individual carbon nanotubes were plotted against their corresponding lengths. This data is presented below in Figure 4.6.

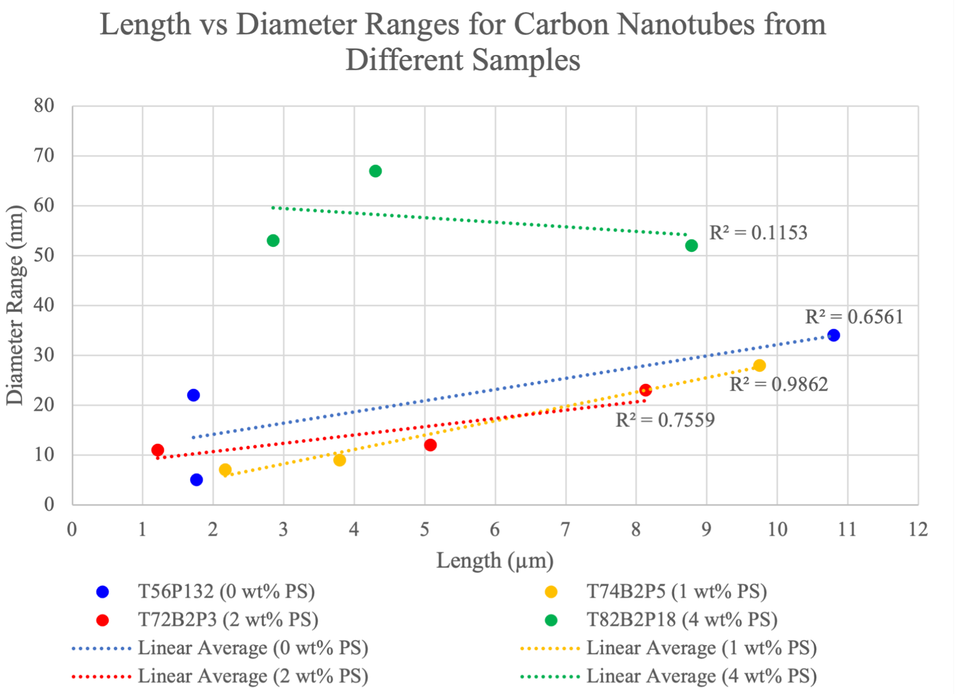

Figure 4.6: Plot of carbon nanotube length vs diameter ranges. Carbon nanotubes within each sample are plotted as a function of their length in μm and diameter range in nm. The linear average is also shown per sample and R2 value given to gauge how well the linear average trends fit the data.

Analysis in Figure 4.6 demonstrated a clear relationship between length and variation in diamter (diameter range) however, the strength of this relationship varies between samples. Using linear trendlines and statistics it was possible to determine how well the range in diameters correspond to the overall carbon nanotube length. In samples T74B2P5 (1 wt% PS), and T72B2P5 (2wt% PS) a strong positive linear relationship could be seen between the length of grown carbon nanotubes and their variation in diameters, where an R^2 value of *0.9862* and *0.7559* could be seen respectively [110]. Sample T56P132 (0 wt% PS) demonstrated a slightly weaker moderately positive linear relationship as shown by an R^2 value of *0.6561* [110]. As previously mentioned, the ranges in diameters for carbon nanotubes in sample T82B2P18 (4 wt% PS) showed a much larger variation in diameter at varying points along the nanotubes, this was reflected in a poor R^2 value of *0.1153* [110]. This further supports the notion that this particular growth method is susceptible to overdosing of polystyrene/carbon causing increased variability in grown carbon nanotubes.

Visual Observations

Further investigation through visual inspection allowed for the identification of additional structure features as well as other interesting observations. This was first demonstrated in the ‘Thick’ to ‘Thin’ growth of carbon nanotubes. In the previous section it was noted that carbon nanotubes exhibited varying degrees of diameter changes along the nanotube, this could be observed on visual inspection. An example of this is illustrated below in Figure 4.7.

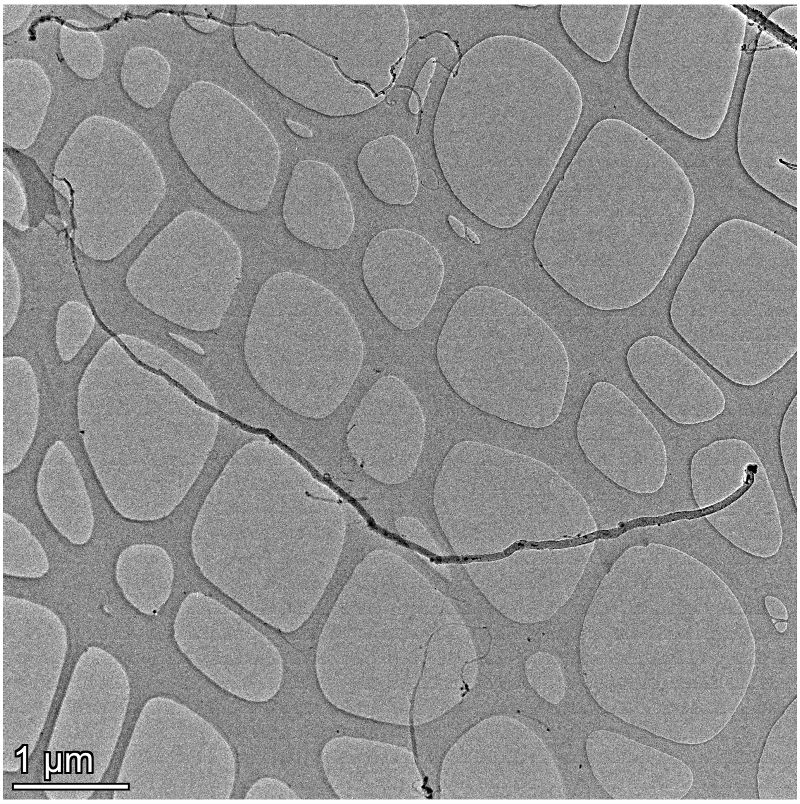

Figure 4.7: Demonstration of thick-to-thin growth in T72B2P3 (2 wt% PS) MWCNT 3. Carbon nanotubes shown in this TEM image visually demonstrate thick-to-thin growth, not only in the central carbon nanotube but also surrounding nanotubes as well.

Inspection of HRTEM images demonstrateed how the thickest point in the carbon nanotube is around the catalyst particle. From there a constant diameter was initially maintained however, this often gradually decreases either naturally or due to the inclusion of another smaller catalyst particle. This was witnessed in many of the other imaged carbon nanotubes. It is worth noting that a ‘Thick’ to ‘Thin’ to ‘Thick’ trait was never observed however, it’s reverse ‘Thin’ to ‘Thick’ to ‘Thin’ was occasionally witnessed.

Additionally, in carbon nanotube structures, there was the presence of direction changes. These could be a mixture of slight to abrupt changes; however, these often followed the introduction of a further catalyst particle in the carbon nanotube growth where a difference in shape or orientation could cause a change in growth direction. It could be observed that abrupt changes only tended to happen as a result of a catalyst particle, whereas shallow changes could happen with or without catalyst particle interference. It has been widely found that catalyst particles can cause carbon nanotube deviations through the introduction of defects, as well as the growth of multiple carbon nanotubes from different facets of a single catalyst particle [111]. The exact cause of independent shallow changes however, is unknown and could be a result of the production process or slight structural changes such as changing numbers of walls. Examples of both of these types of direction changes can be seen in Figure 4.7 and Figure 4.8.

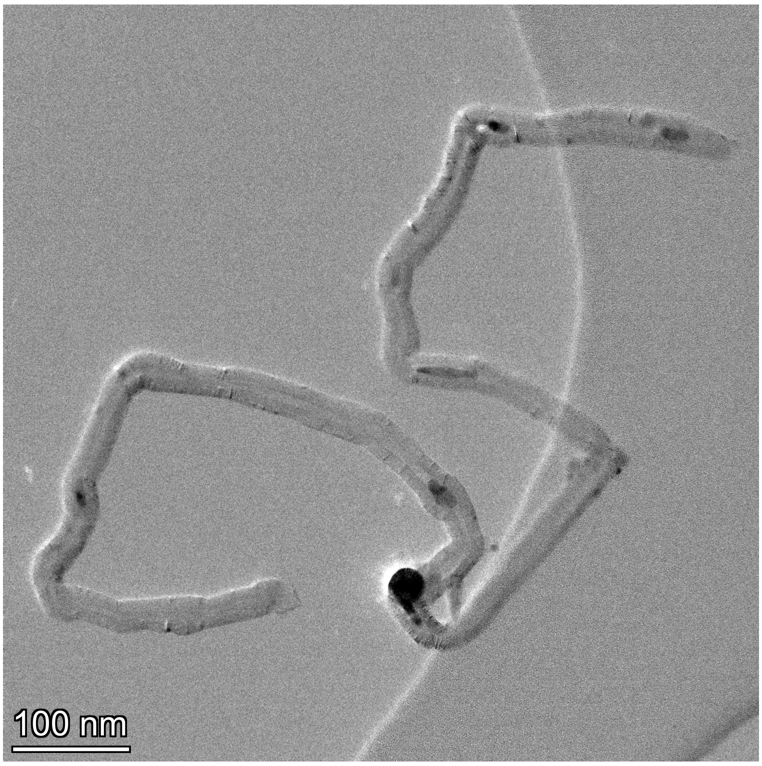

Figure 4.8: Demonstration of growth direction changes in T56P132 (0 wt% PS) MWCNT2. The carbon nanotube shown in this TEM image visually demonstrates multiple 90° direction changes in a single carbon nanotube.

Both instances suggested the presence of defects in the growth stage of these nanotubes resulting in direction changes as demonstrated above [112]. The growth of "curved" and "kinked" carbon nanotubes is known to be a common occurrence in chemical vapour deposition methods [112].

The final observation was specific to one sample in particular: T82B2P18 (4 wt% PS), in which it was noticed that grown carbon nanotubes contained a shell coating. Upon further inspection this was found to be the presence of amorphous carbon. This is illustrated below in Figure 4.9.

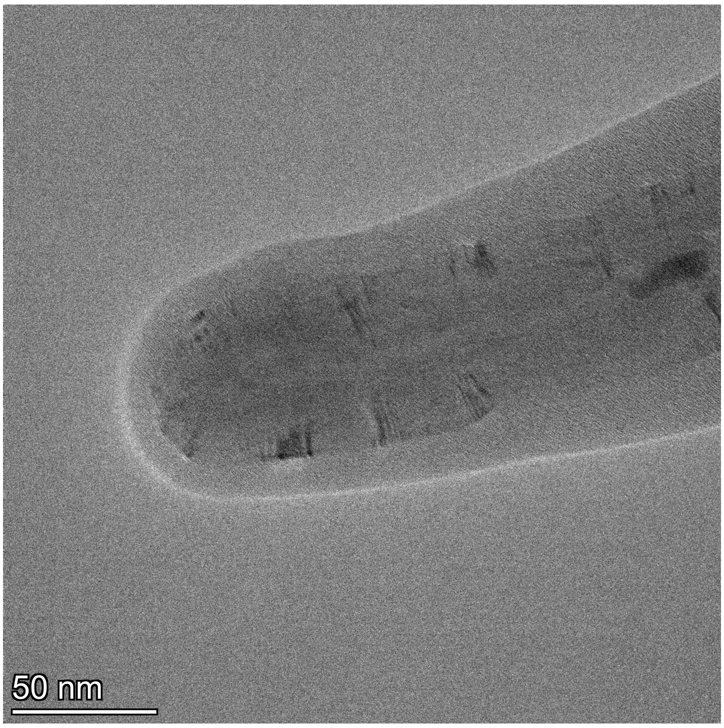

Figure 4.9: Demonstration of amorphous carbon growth on the outer layer of carbon nanotubes in sample T82B2P18 (4 wt% PS). Clearer in zoomed and better quality images, a clear shade and pattern difference is noticeable indicating the difference structure type. When compared with the shade and pattern of known amorphous carbon film of the TEM support (not visible in this image) an almost identical similarity is noticed.

The presence of amorphous carbon could be confirmed both on high resolution inspection and through comparison with the TEM grid substrate which was also amorphous carbon. The isolation of this occurrence to the T82B2P18 (4 wt% PS) sample, provided evidence to suggest that it was a result of the higher polystyrene content in the initial solution. Furthermore, it could then be argued that this was a further effect of polystyrene overdosing where resulting carbon nanotubes were inherently thicker than standard nanotubes due to the hybrid structure of a nanotube core with amorphous carbon shell as illustrated in Figure 4.9.

4.2.2 Core Structure Investigations

In this section of the chapter, results from investigations into carbon nanotube core structure will be presented and discussed. This will include analysis of the number of walls in carbon nanotubes in each sample, as well as an inspection of the interlayer/wall spacing through the use of FFT pattern analysis.

Number of Walls

Analysis of carbon nanotube wall counts was performed using three approaches as detailed in Section 4.1.5. The first of these approaches applied the line profiling tool in Fiji/ImageJ, where a line was drawn across carbon nanotubes. The resulting plot obtained was a graph of distance vs pixel intensity, where the peaks represented walls in the carbon nanotubes. To efficiently determine the number of walls in a given carbon nanotube, the "Find Peaks" tool was used where the number of *Maxima* and *Minima* points were given. For the purpose of carbon nanotube wall counting, the number of maxima corresponds to the number of walls. An example of line profile drawing and the resulting line profile and analysis is given below in Figure 4.10.

The second approach used involved visually counting the number of walls in carbon nanotubes using the multi-point tool in Fiji/ImageJ. Finally, Equation (4.3) was used to approximate the number of walls in carbon nanotubes, utilising the distance between the innermost and outermost walls. The use of three methods was not only for comparison but also for redundancy should one or two of the methods not be possible. As it will soon be demonstrated, one of these methods quickly showed unreliability compared to the other two. Furthermore, determination of the number of walls in carbon nanotubes from the sample: T82B2P18 (4 wt% PS), could not be completed due to inability to visualise individual walls under HRTEM. The results of this investigation on these samples are shown below in Table 4.5.

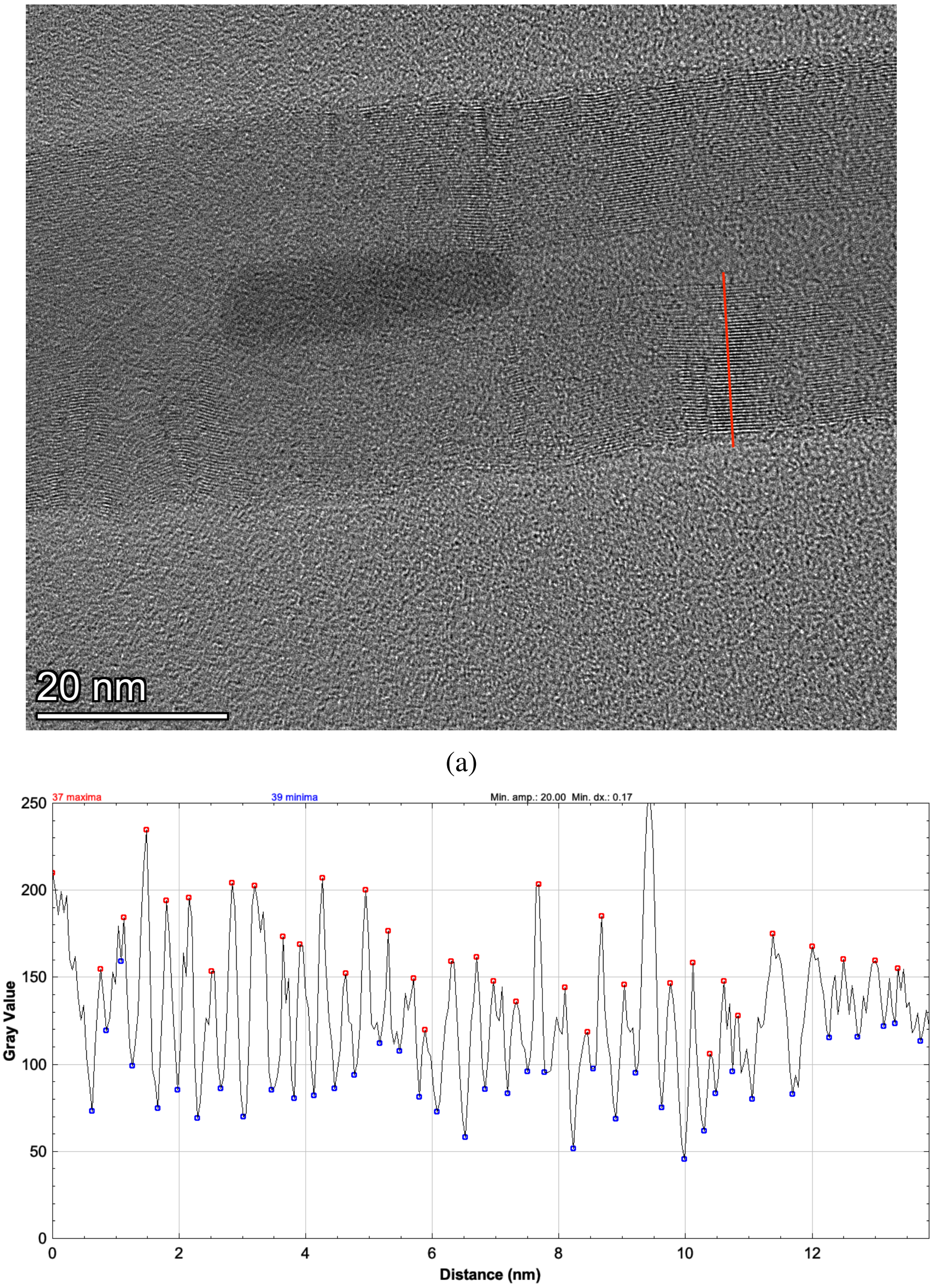

(a)

(b)

Figure 4.10: HRTEM image indicating positions of line profiles and corresponding line profile plot with Find Peak analysis of a carbon nanotube where the resulting maxima corresponds to the number of walls in the carbon nanotube.

Table 4.5: Table of the number of walls from the first reading in each carbon nanotube. Wall readings are displayed as a product of three methods for each carbon nanotube in each sample.

Sample ID	MWCNT 1			MWCNT 2			MWCNT 3		
	Line Profile	Visually	Equation	Line Profile	Visually	Equation	Line Profile	Visually	Equation
T56P132 (0 wt% PS)	69	77	78	49	68	67	-	-	32
T74B2P5 (1 wt% PS)	34	50	55	67	-	90	63	102	105
T72B2P3 (2 wt% PS)	-	-	85	20	21	21	14	18	19
T82B2P18 (4 wt% PS)	No Reading	No Reading	No Reading	No Reading	No Reading	No Reading	No Reading	No Reading	No Reading

In Table 4.5 it could be seen that that there were numerous instances of inconsistency between results obtained from the line profile method vs the visual and numeric methods. As a result of this, readings acquired using this approach would not be used in carbon nanotube wall number investigations. Similar to average carbon nanotube diameter investigations, the counted number of walls were shown to vary greatly both within samples and across all samples. Furthermore, there did not appear to be any initial correlation between wall count and dosage of polystyrene in samples. The varying factor between these carbon nanotubes however, was the shape, orientation, and size of the initial Fe catalyst particles as noted from observation. The size of the catalyst particle is known to have effects on both the diameter and wall count in carbon nanotubes, as shown both earlier in this investigation and in previous works [113]. It was therefore reasonable to suggest that given the growth process remains unchanged and no pattern was observable between samples, the variation of wall count in these carbon nanotubes was a factor predominantly affected by the Fe catalyst particle size, shape, and orientation.

Carbon Nanotube Wall Count Consitency

Similar to the diameter consistency investigations, carbon nanotube wall count consistency along the nanotubes was analysed by recording the number of walls found using the three approaches previously described at three separate points along the nanotubes. The results of these investigations are detailed in Table 4.6 below.

Table 4.6: Table of number of wall readings at different points along each carbon nanotube. Wall readings were taken at three different points per carbon nanotube for each method where possible.

Sample ID		**MWCNT 1**			**MWCNT 2**			**MWCNT 3**		
		Line Profile	**Visually**	**Equation**	**Line Profile**	**Visually**	**Equation**	**Line Profile**	**Visually**	**Equation**
T56P132 (0 wt% PS)	Reading 1	69	77	78	49	68	67	-	-	32
	Reading 2	64	-	78	65	-	106	-	-	41
	Reading 3	-	-	72	39	55	58	-	-	31
T74B2P5 (1 wt% PS)	Reading 1	34	50	55	67	-	90	63	102	105
	Reading 2	24	34	34	66	91	91	92	141	146
	Reading 3	37	55	55	72	101	105	-	-	-
T72B2P3 (2 wt% PS)	Reading 1	-	-	85	20	21	21	14	18	19
	Reading 2	-	-	89	-	-	32	12	17	20
	Reading 3	-	-	94	-	-	-	21	25	27
T82B2P18 (4 wt% PS)	Reading 1	No Reading	No Reading	No Reading	No Reading	No Reading	No Reading	No Reading	No Reading	No Reading
	Reading 2	No Reading	No Reading	No Reading	No Reading	No Reading	No Reading	No Reading	No Reading	No Reading
	Reading 3	No Reading	No Reading	No Reading	No Reading	No Reading	No Reading	No Reading	No Reading	No Reading

As in previous analysis one of the approaches, the line profile approach, proved to be quite inaccurate in comparison to the visual and equation counting methods. Hence, in this examination the results from the line profile approach would also not be used. As in the diameter consistency analysis, the number of carbon nanotube walls was shown to change in all samples. However, the degree of change was shown to vary significantly between carbon nanotubes. As in previous analysis, this could be accounted for by the introduction of new variably sized Fe catalyst particles at different points along the carbon nanotubes [113]. When comparing with the ranges in diameters for each carbon nanotube however, cases were observed where the change in wall count did not fit with the change in nanotube diameter. A typical example being MWCNT1 from sample T56P132 (0 wt% PS) where the range in diameter was shown to be *34 nm* and the range in number of walls was shown to be approximately *6* walls. The excess diameter could only be accounted therefore in two ways; surface growth of amorphous carbon, or core diameter increase. In the case of this carbon nanotube, no amorphous carbon was visible on the surface of the carbon nanotube, as such the excess diameter must be accounted for in an increased core diameter. The presence of a larger core diameter is characteristic of the insertion of a larger catalyst particle at a joining stage in the carbon nanotube growth. This larger core but limited change in wall count further supported the idea that the number of walls present in a carbon nanotube was not solely linked to the size of the catalyst particle from which they were grown, but were also determined by other factors during their growth. This therefore makes the topic of consistently structured carbon nanotube growth much more complex to achieve.

FFT Pattern Analysis

To best determine the interlayer structure of carbon nanotubes, FFT (Fast Fourier Transform) patterns of selected image areas were used. By performing this technique on on HRTEM images and selected areas of HRTEM images, basic diffractograms could be created, where features like diffraction spots and rings could be used to determine the interlayer spacing and structure of the area of investigation.

Carbon Nanotube Wall Spacing

Carbon nanotube wall/layer spacings (d spacings) were determined through the use of FFT analysis on HRTEM images. Specifically, on segmented areas of high magnification carbon nanotube images where walls could be clearly seen by eye, thus making their signal more prominent in FFT spectrum images. The inter-planar distance of nanotube walls could be found by recording the locations of FFT spots indicating the distance per cycle value and thus the inter-planar distance. This is demonstrated below in Figure 4.11.

Analysis of results of segmented area FFT spectrums of high magnification HRTEM images allowed for approximation of interlayer spacings of carbon nanotube walls. Results have shown peak positions vary between images and thus carbon nanotubes however, certain peak positions were common to all and particularly in HRTEM images where carbon nanotube walls were clearly defined. As illustrated above in Figure 4.11b, the common peak in all images was located at a distance of *0.34 nm*. This peak demonstrated the interlayer spacing of carbon nanotube walls. Furthermore, this value corresponded with the known inter-planar spacings of graphite, *0.335 nm*, which comprises of stacked of graphene sheets much like carbon nanotubes [97]. The exact interlayer spacings of carbon nanotube walls were shown to

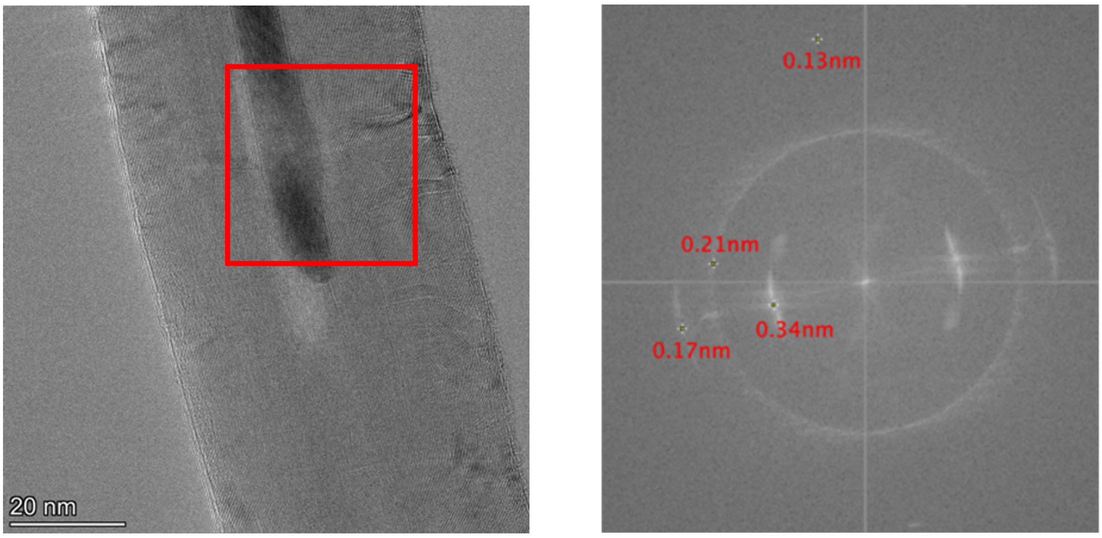

(a) (b)

Figure 4.11: Demonstration of wall spacing investigation. a) High magnification TEM image of carbon nanotube with visible walls, b) FFT of segmented area indicating atomic plane spacings. Segmented area FFT was applied to the area indicated by the red box to determine the inter layer spacings of carbon nanotube walls.

vary depending on numerous factors such as curvature and number of layers [114–116]. Investigation conducted by Kiang et al., Kharissova et al., and Singh et al. have all shown how interlayer spacings decrease towards *0.34 nm* as the diameter of the carbon nanotubes increases, suggesting an inversely proportional relationship between the two parameters [114–116]. Further studies also suggest these changes in interlayer spacings could be linked to interlayer Van der Waals interactions and equilibrium interlayer spacing for the different carbon nanotube structural orientations e.g., Armchair or Zig-Zag [115].

Structural Observations

In addition to interlayer spacings, FFT spectrums could further be used to determine the structural composition of selected areas, through the identification of either spots or rings in FFT spectral images. Examination of selected area FFT images taken from high magnification HRTEM images, showed a mixture of crystalline, poly-crystalline, and in some cases, amorphous structures.

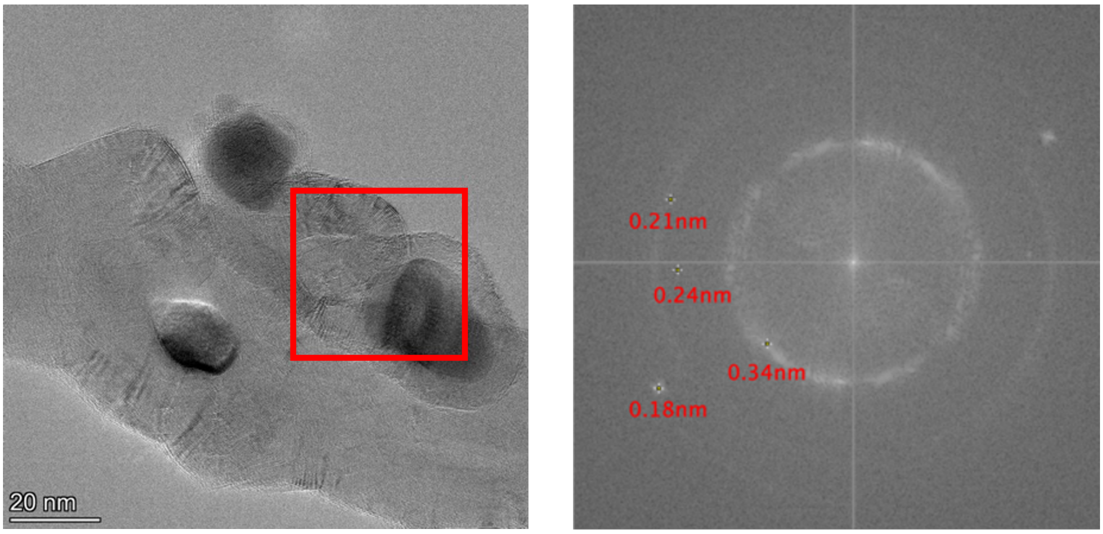

(a) (b)

Figure 4.12: Example of polycrystalline structure in T56P132 MWCNT 1. a) HRTEM image with selected area, b) selected area FFT. Segmented area FFT was applied to the area indicated by the red box to determine the inter layer spacings of carbon nanotube walls. Analysis of the type of FFT response was used to determine the polycrystalline structure of the segmented area.

As illustrated above in Figure 4.12, it was often noticed that the structure surrounding the catalyst particles were shown to be poly-crystalline/amorphous in nature from FFT patterns. This was demonstrated above in Figure 4.12b by the presence of a "ring" pattern at a distance of *0.34 nm*. In contrast, FFT spectrums of areas containing walls only, similar to that shown in Figure 4.11b, it was noticed that these patterns demonstrated a crystalline/poly-crystalline structure by the presence of "spots". On comparison of image originals, it was also noticed that multi-directional walls were shown around catalyst particles, giving the illusion of an amorphous structure. This was in-fact a demonstration of a 'junction' point in the carbon nanotubes structure where two carbon nanotubes with mismatched orientation had joined, or multi-directional growth had occurred from a single catalyst particle. This was more clearly illustrated in Figure 4.13 by the overlapping of carbon nanotube walls from different directions.

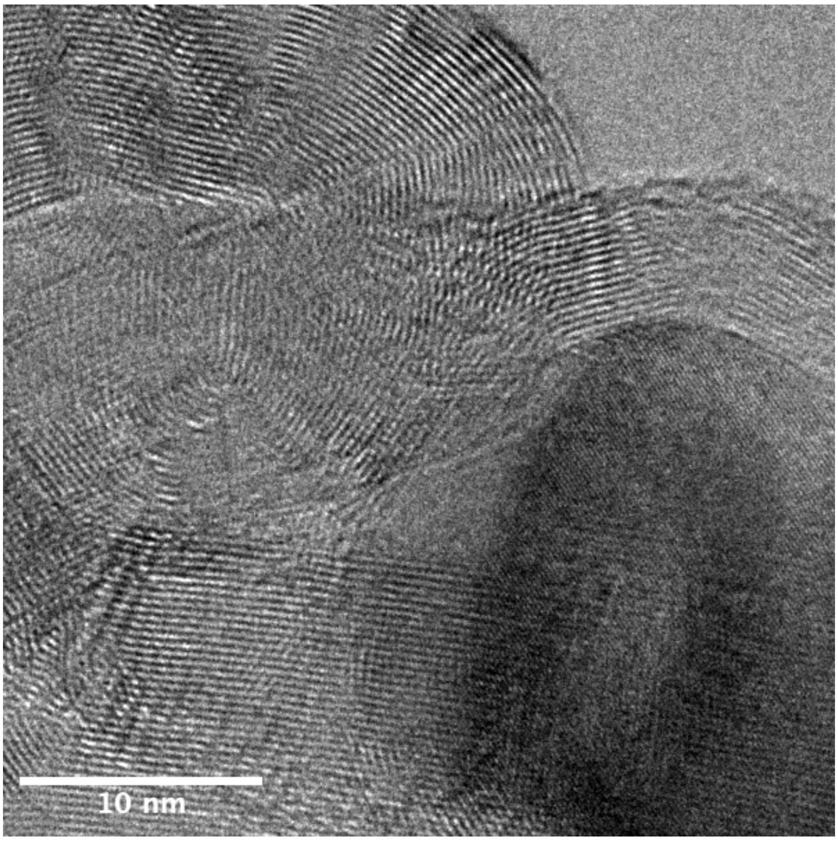

Figure 4.13: Selected area view of HRTEM image shown in Figure 4.12a. A zoomed in view of the segmented area shown in Figure 4.12a clearly presenting multiple wall of different and overlapping orientations.

4.3 Summary

Multi-walled carbon nanotubes grown by Ali Hedayati and Jainabi Sallah-Conteh, through catalytic chemical vapour deposition (CCVD) were imaged using HRTEM where their surface and core structures could be investigated using image processing software. Example carbon nanotubes were selected from each sample for surface and core structure investigations. Surface structure investigations involved length and diameter analysis to observe results and identify trends. Initial length investigations did not identify any relationship between carbon nanotube lengths and polystyrene content in growth solutions. Results here appeared random in nature which was shown to match previous works. However, further statistical analysis did in-fact identify a trend between polystyrene content and carbon nanotube lengths, suggesting that increased polystyrene content, increases length uniformity between carbon nanotubes grown. Similarly in diameter investigations, the results also appeared random in nature. However, further statistical analysis presents a possible relationship between polystyrene content and diameter consistency when viewing overall standard deviation ranges. Here it could be seen that overall diameter standard deviations decreased with increasing polystyrene content to a critical concentration, above this critical concentration a negative effect was observed. Visual observation of these carbon nanotubes supported these findings where nanotubes were shown to start thick at one end and transition to thin at the other. Length vs Diameter analysis also revealed a pattern corresponding to polystyrene content, similarly to that shown in overall diameter investigations. Here, the relationship between length and diameter was shown to become more linear with increased polystyrene concentration up to a critical concentration where, as before, the linearity in the relationship decreases. Further visual observations also included the presence of carbon nanotubes with curves as well as large angle changes indicating defects during the growth of walls. Finally, for the 4 wt% polystyrene sample it was noticed the outermost layer consisted of amorphous carbon making these carbon nanotubes particularly large in diameter. The presence of this in only carbon nanotubes from the 4 wt% sample suggested this could be related to the polystyrene dosage.

Core structure inspection was possible through the use of high magnification, wall visible, HRTEM images. Much like the diameter and length investigations, the number of walls in each carbon nanotube was shown to vary greatly with no establish-able correlation to polystyrene content. It was therefore reasonable to suggest that the polystyrene content had not effect on walls grown and this variable was predominantly effected by catalyst particle size, shape, and orientation. Similarly, the range in number of walls was shown to vary within each tube however, an interesting discovery was made when the change in number of walls in some carbon nanotubes did not match the change in diameter. This suggested that the unaccounted-for distance must be found in a larger centre core determined by the size of the catalyst particle. To further understand the structure of carbon nanotube walls, selected area FFT's of wall visible HRTEM images were preformed from which interlayer spacings could be determined. The results from these carbon nanotubes found the interlayer spacing value to be 0.34 nm which corresponded with the known interlayer spacing of stacked graphene sheets e.g., graphite. FFT specctrums could also provide some insight into the crystallinity of the carbon nanotubes. The presence of “rings” and “dots” in these images suggested a crystalline/poly-crystalline structure in wall only areas whereas, in areas surrounding catalyst particles the structure was found to be more poly-crystalline/amorphous. This change however could partially be accounted for in the overlapping of multi-directional walls where rings presented as sharp and thinner signals in comparison to broad and smooth/blurred rings for amorphous structures.

Overall, HRTEM analysis of samples has demonstrated the successful growth of carbon nanotubes utilising the recycled plastic *Polystyrene* as a feedstock. This analysis provides a strong basis for future research involving the up-cycling of otherwise wasted plastics into carbon nanotube based materials and structures for numerous applications.

Chapter 5

ATOMIC STRUCTURE INVESTIGATIONS OF Ag NANOCLUSTERS ON AMORPHOUS CARBON

Overview

This chapter will present, discuss, and summarise the methods and results of Ag nanocluster investigations through AC-STEM. Analysis will include size estimation through HAADF Intensity and single atom calibration, and Isomer structure determination. These results are summarised at the end of this chapter as well as in Paper II: Influence of air exposure on structural isomers of silver nanoparticles.

5.1 Analysis Methods

This work analyses both size and structure of produced nanoparticles using both visual, as well as data extraction and manipulation techniques. Analysis of captured HAADF-STEM images was performed using the image processing software ImageJ/Fiji, and existing simulation atlas's and data was recorded in MS Excel.

5.1.1 Cluster Size Analysis

Cluster size analysis was performed in a two step process, involving first the calibration of the Single Atom Intensity (SAI) for a dataset (HAADF-STEM Image), before larger clusters were analysed and size calculated from the SAI. Images were first prepared by applying an FFT bandpass filter with minimums and maximums at *2 px* and *400 px* respectively to filter out unwanted artifacts. This also had the effect of clarifying the image as well as the boundaries of the particles in the image, thus making the concentric ring method easier to perform [117]. To obtain the necessary information in each process, a concentric ring method was employed to obtain Area and Raw-Integrated-Density values for particles found in datasets as illustrated below in Figure 5.1, where the Raw-Integrated Density is the sum of all pixel values in a segmented area [118].

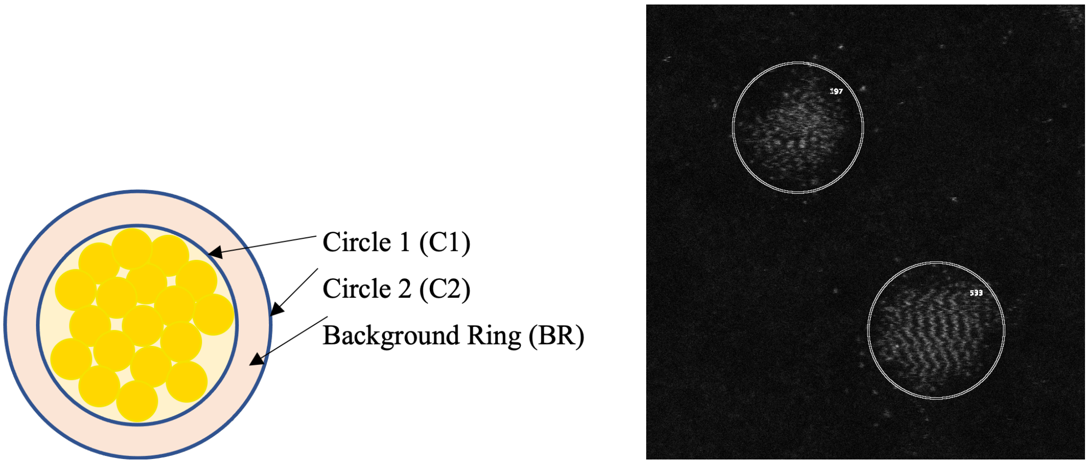

(a) (b)

Figure 5.1: Examples of the concentric ring method used to obtain Area and Raw Integrated Density values of particles found in STEM images. Circle 1 is drawn tight to the particles boundaries, whilst circle 2 is of a slightly larger diameter around the particles. a) Schematic Diagram, b) Example use in HAADF-STEM image of Ag nanoclusters.

This process was an adapted version of that previously used by Young et al. to determine particle intensities and involved first determining the background intensity and area of a particle to find the background intensity per unit area. Once found this could be subtracted to identify the true HAADF intensity of the atoms within a particle. This process is detailed in Equations (5.1) to (5.5).

$$Background\ Intensity = C2\ Raw\ Integrated\ Density - C1\ Raw\ Integrated\ Density \tag{5.1}$$

$$Background\ Area = C2\ Area - C1\ Area \tag{5.2}$$

$$Background\ Intensity\ per\ Unit\ Area = \frac{Background\ Intensity}{Background\ Area} \tag{5.3}$$

$$C1\ Background\ Intensity = Background\ Intensity\ per\ Unit\ Area \times C1\ Area \tag{5.4}$$

$$Particle\ Intensity = C1\ Raw\ Integrated\ Density - C1\ Background\ Intensity \tag{5.5}$$

To speed up analysis, this process was evolved into macros which could obtain the required data at a significantly faster rate. This also allowed for an increase in sample size when estimating the Single Atom Intensity, as will be detailed in the next section. An example of macro identified atoms and nanoclusters is shown below in Figure 5.2.

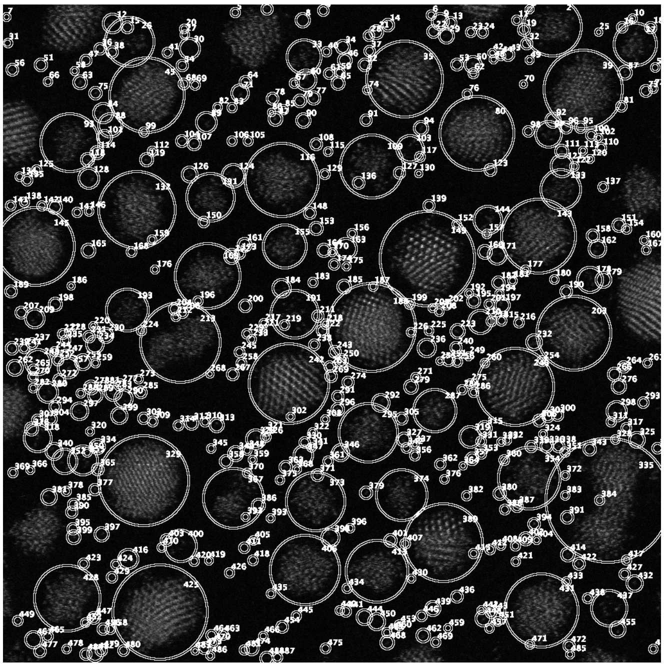

Figure 5.2: Example illustration of Au nanoclusters and atoms that has been analysed and sorted by developed macro scripts.

Single Atom Intensity Calibration

The first stage in cluster size approximation was to determine and calibrate the single atom intensity for the dataset being analysed. To do this single atom like-sized particles were isolated and measured using the threshold and measure features of the image processing software. The results returned were often in the high hundreds or thousands and most being irrelevant therefore, the results were filtered down to include only those particles with an area between $0.01nm^2$ and $0.1nm^2$. The unit of measure for area in the image processing software is pixels and hence it was necessary to convert these values to $pixels^2$ (px^2). This value varied however depending on the magnification used, as such the corresponding pixel to nm scale had to be accounted for in the conversion. The equation for this conversion is shown below in Equation (5.6).

$$Area(px^2) = \frac{Area(nm^2)}{Scale^2(\frac{nm}{px})} \tag{5.6}$$

As these values were magnification dependent, a lookup table was created which could be applied globally to all datasets. This lookup table is shown below in Table 5.1.

Table 5.1: Single atom sized particles with areas between $0.01nm^2$ and $0.1nm^2$ equivalent pixel segregation bounds per magnification lookup table.

Magnification	**Scale** ($\frac{nm}{px}$)	**Lower Pixel Area Boundary** ($0.01nm^2$)	**Upper Pixel Area Boundary** ($0.1nm^2$)
3 Mx	0.0628038	2.535 (3)	25.352 (25)
4 Mx	0.0472543	4.478 (5)	44.783 (45)
5 Mx	0.0379246	6.952 (7)	69.527 (69)
8 Mx	0.0236675	17.852 (18)	178.523 (178)
10 Mx	0.0189151	27.950 (28)	279.500 (279)
15 Mx	0.0125786	63.202 (64)	632.026 (632)

Once a number of single atom like particles had been identified, the particle intensities could be calculated using the concentric ring method described above in Figure 5.1. At first, this analysis used a sample size of 10 single-atom-like particles where the concentric ring method previously described was applied to approximate an average single atom intensity. Initially, the single atom intensity was calculated using the returned *Integrated Density* value. However, the calculation using the *Raw Integrated Density* was quickly adopted after it was noted this value was more accurate. Following the first round of nanocluster size approximation, it was noticed that estimated nanocluster sizes and diameters did not correspond with previous works. Using the analysis by Young et al. as a template, nanocluster atom vs diameter plots were compared and a trend was noticed. The trend indicated that the atom count for clusters of a set diameter was smaller than previously found. In the context of this analysis this meant that current single atom intensity calibration was incorrect indicating the current value was higher than it should be. It was suggested that the current single atom intensity approximations did not only come from too small a sample, but also in fact included a mix of monomers, dimers, and trimers, which appeared as one particle on HAADF-STEM images. To filter out and determine the correct monomer intensity from mixed particles, potential single atoms were re-analysed using Fiji/ImageJ macro scripts where a larger sample size could be obtained as described in the next section. After obtaining intensities for all single atom like particles, the last stage was to plot the values in a histogram and identify the first Gaussian peak, corresponding to the monomer value. The average value for the most densely populated bin in this peak was then taken to be the calibrated single atom intensity for the dataset. This step is demonstrated below in Figure 5.3.

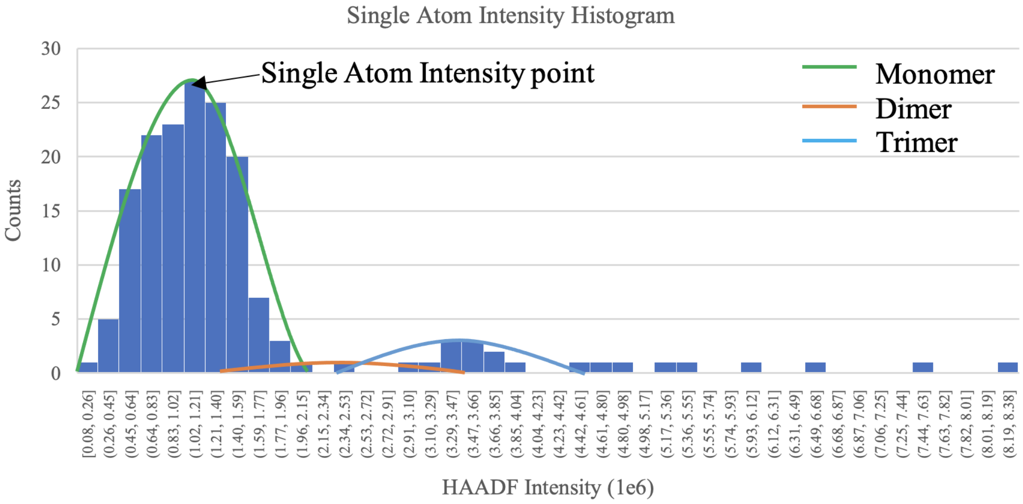

Figure 5.3: Example Single Atom Intensity Histogram from HAADF 8Mx 0028 STEM image. Demonstration of the identification of three Gaussian peaks is shown. The first peak, shown in green, denotes the monomer intensity distribution, second peak in orange denotes the dimer intensity distribution, and the timer intensity distribution is denoted in blue.

Cluster Size Approximation

Once the single atom intensity had been obtained, the approximation of nanocluster sizes could begin. Once again the concentric ring method shown in Figure 5.1 and detailed further in Equations (5.1) to (5.5), was used to determine particle intensities for each observable cluster. The number of atoms in each cluster could then be approximated using the calibrated SAI as shown in Equation (5.7).

$$Cluster\ Size = \frac{Cluster\ Intensity}{Single\ Atom\ Intensity\ for\ Dataset} \tag{5.7}$$

5.1.2 Cluster Structure Analysis

Cluster structure analysis was undertaken by two means; Quasi-structure investigations, and Isomer structure determination. Quasi-structure investigations involved the use of measured cluster properties to approximate the 2D or 3D structure of clusters whereas, Isomer structure determination utilised visual comparison of clusters with an existing simulation atlas to determine isomeric structures.

Quasi-Structure Determination

To ascertain the quasi-structure of clusters', their approximated number of atoms and equivalent circular diameter were used. To obtain the equivalent circular diameter of a cluster, the area recorded for the ring/circle 'C1' was used and diameter estimated using the Equation (5.8) shown below.

$$Equivalent\ Circular\ Diameter\ (ECD) = \sqrt{\frac{Area \times 4}{\pi}} = 2 \times \sqrt{\frac{Area}{\pi}} \tag{5.8}$$

The equivalent circular diameters of clusters were then plotted against their corresponding number of atoms with trendlines for various shapes, both 3D and 2D, to best approximate their quasi-structure. The trendlines for the comparing shapes could be obtained using the relationship shown in Equation (5.9) where the volume of an atom is given using Equation (5.10).

$$\begin{gathered} Number\ of\ Atoms\ (N_{Atoms}) = \frac{Volume\ of\ Shape}{Volume\ of\ Atom} \\ Where\ the\ ECD\ is\ made\ the\ subject\ of\ the\ equation \end{gathered} \tag{5.9}$$

$$\begin{gathered} Volume\ of\ Au\ Unit\ Cell\ is\ 0.408^3 nm^3 = 0.068 nm^3 \\ 4\ Atoms\ per\ Unit\ Cell \\ Volume\ of\ Single\ Au\ Atom\ is\ \frac{0.068}{4} = 0.017 nm^3 \end{gathered} \tag{5.10}$$

3D Structures

Gas phase grown and soft deposited clusters are known to be quasi-spherical in nature however, clusters grown through aggregation and self-assembly of atoms on a surface can taken many different 3D structures [119, 120]. In this work two 3D structures are explored; Quasi-Spherical and Quasi-Hemispherical. Using the formulae for the volumes of a sphere and hemisphere, the trendlines for these structures could be obtained from Equations (5.11) and (5.12) respectively.

$$ECD = 2 \times \sqrt[3]{\frac{0.017 \times N_{Atoms}}{\frac{4}{3} \times \pi}} = 0.319 \times \sqrt[3]{N_{Atoms}} \tag{5.11}$$

$$ECD = 2 \times \sqrt[3]{\frac{0.017 \times N_{Atoms}}{\frac{2}{3} \times \pi}} = 0.402 \times \sqrt[3]{N_{Atoms}} \tag{5.12}$$

2D Structures

Further to 3D structures, it was noticed during analysis that there appeared to be quasi-2D structures and as such as trendline was also established for comparison by modelling the structure of a monolayer raft. Using the formulae for a cylinder with a height equivalent to the diameter of an Au atom (0.34nm) and Equations (5.9) and (5.10), the following relationship could be established for a monolayer raft with N atoms.

$$ECD = 2 \times \sqrt{\frac{0.017 \times N_{Atoms}}{0.34 \times \pi}} = 0.252 \times \sqrt{N_{Atoms}} \tag{5.13}$$

Isomer Structure Determination

The determination of the structural isomer of clusters' was performed through visual comparison with an existing simulation atlas of Au nanoclusters upto a size of 2057 atoms provided by Dr James McCormack in the Nanomaterials Lab at Swansea University. An example excerpt of this atlas is shown below in Figure 5.4.

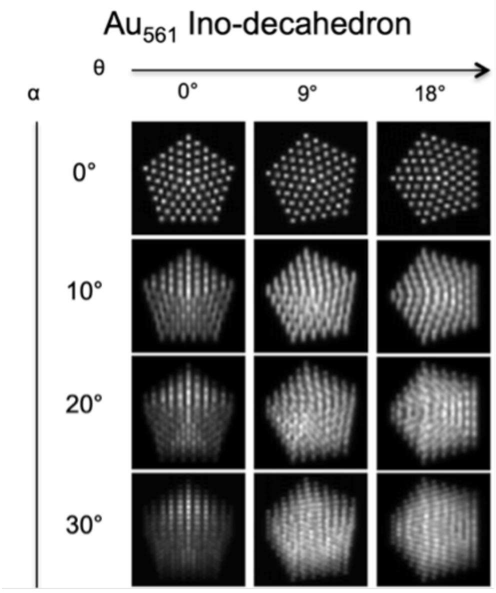

Figure 5.4: Example excerpt of atlas used to identify isomer structures and orientations. This example excerpt is of an Au_{561} Ino-Decahedral cluster at various orientations. The full atlas contains images of Ino-Decahedral, Cuboctahedral, and Icosahedral Au clusters' at numerous orientations for sizes: 13, 55, 147, 309, 561, & 2057 atoms.

Segmented clusters were visually compared with atlas entries with the closest size to that which was approximated. Following comparison, clusters were sorted into one of four categories: Unidentified/Amorphous (U/A), Ino-Decahedral (Dh), Icosahedral (Ih), Face-Centred Cubic (FCC), representing the four main structures under investigation. Where possible the specific orientation of a cluster was also noted. Clusters' that could could not be matched to either Dh, Ih, or FCC were assigned to the U/A category.

5.2 Silver Nanoclusters

In this section of the chapter, the results of analysis into the size and isomeric structures of Silver (Ag) nanoclusters produced by matrix assembly and ion sputtering, will be presented and discussed. This will include a brief introduction into the synthesis method used followed by the results of size and isomer analysis, which will be divided between Single Atom Intensity, Cluster Size Distribution, and Cluster Isomer Distribution investigations.

5.2.1 Argon Matrix Assembly

Synthesis of Silver (Ag) nanoclusters analysed in this thesis was performed using the Argon-Matrix assembly method (MACS), previously detailed in Section 2.1.2, by Jerome Vernieres where the apparatus is shown below in Figure 5.5a. Here this apparatus was composed of two main sections; the main deposition chamber where cluster growth and depostion takes place, and the load-lock chamber used for easy insertion and removal of samples without the need for full system venting [20–22, 121, 122]. In this analysis, Silver (Ag) atoms were thermally evaporated towards a cryo-cooled (15K) copper block (cold-finger) in the presence of Argon (Ar) [121, 122]. The cryo-cooled nature of the copper block causes it to act as a substrate for which the argon gas condenses, this in addition to the presence of the evaporated Ag atoms induces a Ar/Ag matrix to grow where the respective rates of Ar gas and Ag atoms can be used to control the concentration (Metal loading) of the matrix [20–22, 121, 122]. This stage of the synthesis process is illustrated in Figure 5.5b. Upon growing the desired thickness, the matrix was then sputtered with a high energy Ar ion beam thus stirring and sputtering the grown matrix. This resulted in a produced beam of nanoclusters directed towards the deposition substrate, and soft-landed on the substrate as a result of production at cryo temperatures. In this work the substrate was amorphous-carbon coated TEM grids [121, 122]. This stage of the synthesis process is demonstrated in Figure 5.5c.

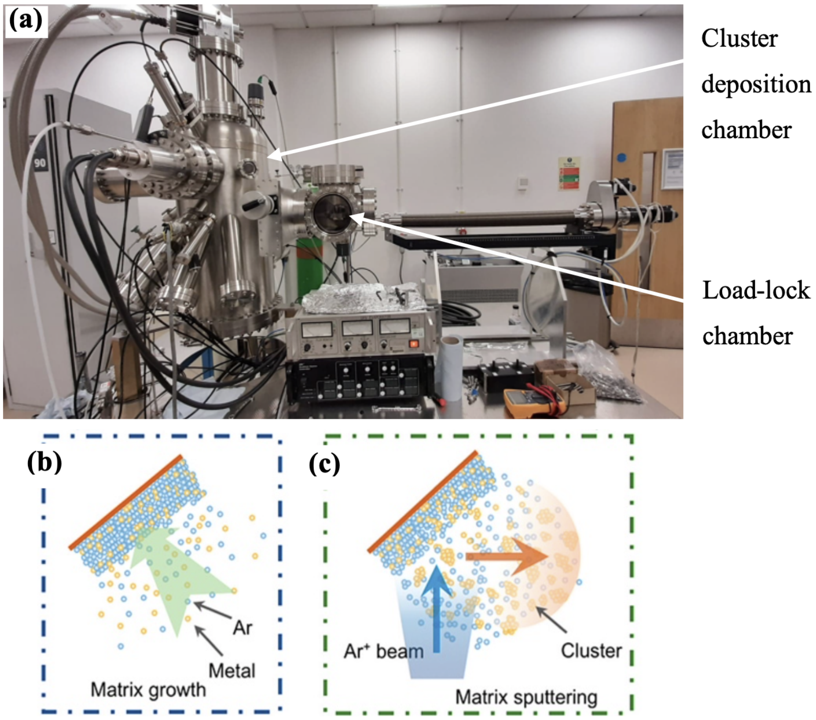

Figure 5.5: Photograph of the device used and deposition method described for Au cluster synthesis. a) MACS setup, b) Matrix growth stage; A matrix of Argon and an evaporated metal is formed on a cryo-cooled copper support. c) Matrix sputtering stage; The grown matrix is then sputtered by Ar^{+} beam causing stirring of the matrix and clusters to be ejected and deposited onto the sample surface. Reproduced from R.E.Palmer, R.Cai, J.Vernieres [20], and E.Watchorn-Rokutan [122].

In this analysis, two samples were produced for analysis under AC-STEM; one low-coverage sample, and one high-coverage sample. In these samples, both samples contained the same metal loading percentage and Ar ion beam voltage, and only the Ar ion beam sputtering current and sputter/deposition time were adjusted. For the low-coverage sample, an Ar ion beam current of *5 mA* was used with a sputter/deposition duration of *10 seconds*. In the high-coverage sample, an Ar ion beam current *15 mA* was used with a sputter/deposition duration of *60 seconds*. The increased nanocluster concentration on the high coverage sample was therefore not only assured by a lengthier deposition time, but also a higher sputtering current thus inducing a higher sputtering rate. The synthesis parameters are summarised below in Table 5.2.

Table 5.2: Table of parameters used in the synthesis of Silver (Ag) nanoclusters via the Matrix-Assembly method.

	Low Coverage Sample	**High Coverage Sample**
Metal Loading (wt%)	5 %	5 %
Ar+ Ion Beam Current	5 mA	15 mA
Ar+ Beam Energy	500 V	500 V
Deposition Time	10 secs	60 secs

5.2.2 Size and Structure Analysis

To perform size and structural analysis on deposited Ag nanoclusters, the produced samples required imaging under HAADF-STEM. The samples in this work were imaged by Dr Thomas Slater at the Electron Physical Sciences Imaging Centre at Diamond Light Source using the JEOL ARM300CF Electron Microscope as detailed in Section 2.2.5 [122]. Imaging was carried out in STEM mode using the High-Angle Annular Dark-Field detector. Data was obtained at six magnifications: 3 Mx, 4 Mx, 5 Mx, 8 Mx, 10 Mx, and 15 Mx, resulting in a broad range of images from which various levels of size and structural analysis could be performed as illustrated below in Figure 5.6. In total 31 datasets were collected for analysis: 14 from the low-coverage sample, and 17 from the high coverage sample. The details of such analysis are presented below.

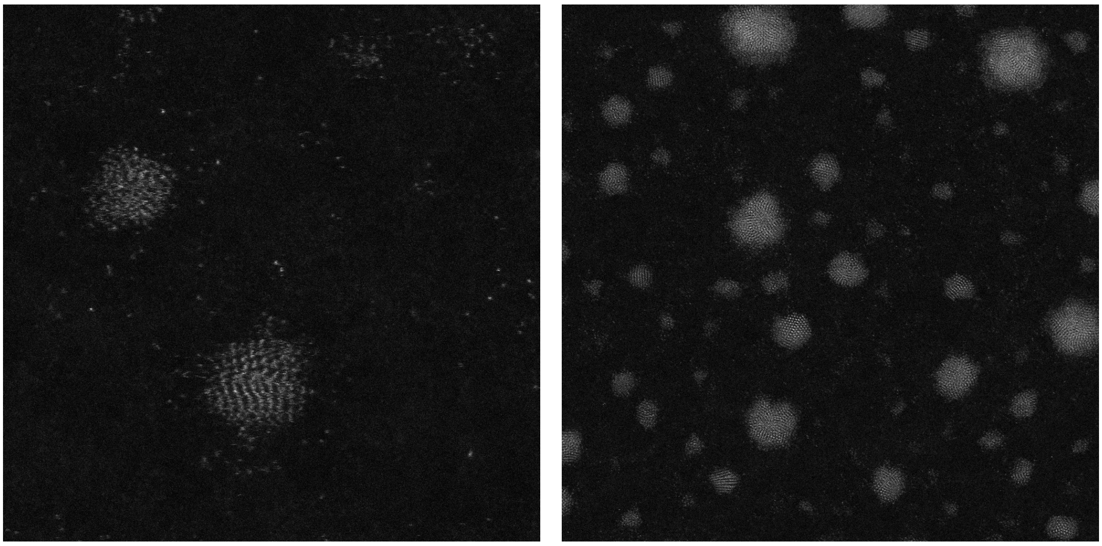

(a) (b)

Figure 5.6: Example HAADF-STEM images of Ag nanoclusters for a) Ag3 (Low-coverage) at 15Mx, and b) Ag9 (High-coverage) at 4Mx, produced by Matrix assembly by Erica Watchorn-Rokutan and imaged by Dr Thomas Slater.

Single Atom Intensities

As previously described, the first stage in the size analysis of nanoclusters in obtained HAADF-STEM images was to correctly calibrate the HAADF intensity for a single atom within datasets. This would be necessary for the correct determination of the number of atoms in nanoclusters. Using the earlier detailed concentric ring method and automated macro scripts, multiple reference points were taken from each image as potential single atoms for analysis. Particle HAADF intensities were calculated and plotted on histograms where single atom intensities could be distinguished from dimers and trimers, as demonstrated in Figure 5.3. A summary of the relative statistics per magnification in each sample set is shown below in Table 5.3, where "*Number of Single-Atom Intensity Datapoints*" refers to the number of images at a given magnification.

Table 5.3: Statistical analysis of calibrated Ag single atom intensities against magnification showing mean, standard deviation, and relative standard deviation.

Ag3 Low-Coverage Sample

Magnification	Number of Single-Atom Intensity Datapoints	Mean Single-Atom Intensity	Standard Deviation	Relative Standard Deviation
5 Mx	8	2.73E+05	1.33E+04	4.87%
8 Mx	1	4.71E+05	0	0%
15 Mx	8	1.43E+06	1.83E+05	12.82%

Ag9 High-Coverage Sample

Magnification	Number of Single-Atom Intensity Datapoints	Mean Single-Atom Intensity	Standard Deviation	Relative Standard Deviation
3 Mx	5	1.15E+05	1.26E+04	10.94%
4 Mx	1	2.04E+05	0	0%
8 Mx	5	5.27E+05	5.65E+04	10.73%
10 Mx	2	7.82E+05	1.56E+04	1.99%

Table 5.3 demonstrated how the mean single atom intensity increases with magnification as expected with no discernible pattern in standard deviations. Furthermore, the appearance of perceivably high standard deviations here, can be corrected here through the knowledge that each dataset was obtained under marginally different imaging conditions therefore altering the single atom intensity per datapoint. This allows for the criteria for a high standard deviation to be shifted to a much higher relative value. Plotting of the individual single atom intensity values per magnification

graphically, further allows for the accuracy of single atom intensity values to be visualised. In plotting of intensity values in this way, a quadratic trend in HAADF intensity should be visible with increasing magnification. This can clearly be seen in Figure 5.7 where the plotting of a 2nd order polynomial fit yields a high R^2 value for both samples in the individual plot as well as the mean value plot. Here the R^2 value can be used as a measure of goodness of fit of the data and thus its accuracy. In Figure 5.7a it can be seen that the R^2 values were *0.9472* and *0.9829* for samples Ag3 and Ag9 respectively, and in Figure 5.7b it can be seen that the R^2 values were *1* and *0.9984* for samples Ag3 and Ag9 respectively. The presence of R^2 values above *0.9* strongly indicates that the measured intensities for single atoms in datapoints are highly accurate when compared to the expected value based on other datapoints, providing confirmation that the correct value for single atom intensity is being used. From Figure 5.7a it could also be noticed that individual datapoint values were seen to be more and more varied as the magnification increases. This is particularly noticeable at *15 Mx* where the relative standard deviation was shown to be 12.82%. This suggested that in the case of determining the single atom intensity values, higher magnification is not always best, particularly as this limits the number of obtainable reference points and analysis sensitivity becomes more pronounced.

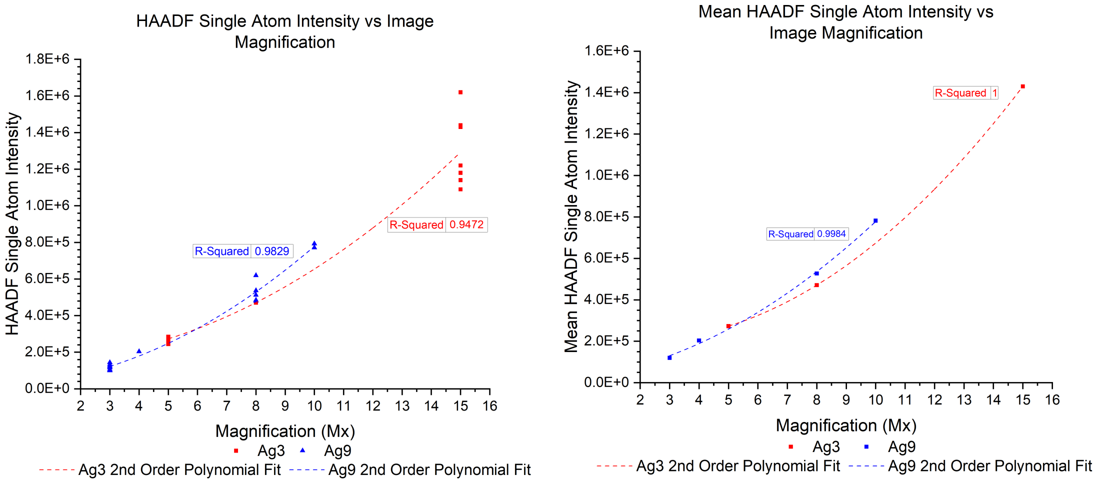

(a) (b)

Figure 5.7: Plots of HAADF single atom intensities vs magnifications per sample set for a) Individual datasets, b) Mean HAADF single atom intensity per magnification.

On review of the number of obtainable reference points in datasets as a function of magnification, a pattern could be identified. It could be seen that on running the *Cluster Intensity* macros, the number of possible single atom like particle reference points was dependent on the magnification used. This fits logically where analysis of a smaller area would lead to less particles being visible. In the context of effective analysis however, in order to obtain the most accurate mean single atom intensity for a magnification, it was advantageous to collect as many reference points as possible for accuracy. In Figure 5.8 it could be seen that the highest number of reference points occur at the *8 Mx* and *10 Mx* magnifications. It could therefore be advised that for samples produced in this way and when using this method for nanocluster size determination, images are best captured at the *8 Mx* and *10 Mx* magnifications for highest accuracy in calibration.

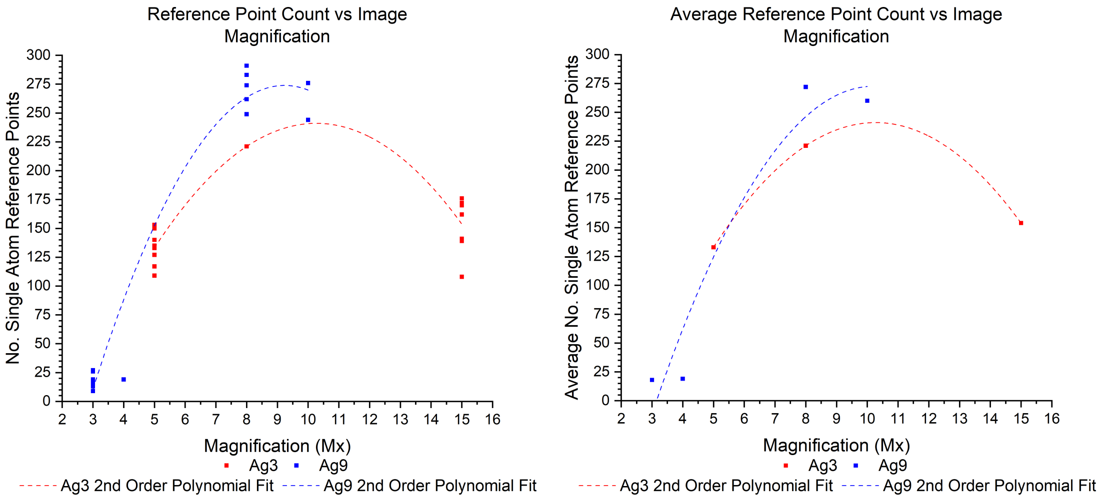

(a) (b)

Figure 5.8: Plots of single atom like particle reference points vs magnifications per sample set for a) Individual datasets, b) Average number of reference points per magnification.

Cluster Size Distribution

Once correct single atom intensities had been determined for each HAADF-STEM image, it was then possible to begin approximation of larger nanocluster atomic sizes. Using the same approach employed towards single atoms, the concentric ring method previously illustrated in Figure 5.1 and Equation (5.7) as well as described in Section 5.1.1, was used on nanoclusters to estimate the number of atoms in their composition. Through the concentric ring method, this began with determination of particle and background intensities using the *RawIntDens* value from which the true nanocluster *RawIntDens* value could be extracted. Once the true nanocluster *Raw Integrated Density* value was found, nanocluster size could be estimated through division by the calibrated corresponding single atom intensity value for the respective dataset, as demonstrated in Equation (5.7). Upon completion of all nanocluster size estimations, analysis of Matrix-Assembly produced nanoclusters could begin via the plotting of nanocluster size results in a histogram. Plotting in this way allowed for not only the range of produced sizes to be seen, but also the identification of distribution peaks as well as common metastable nanocluster sizes. The size distribution is demonstrated and for each sample set in this analysis is shown below in Figures 5.9 and 5.10.

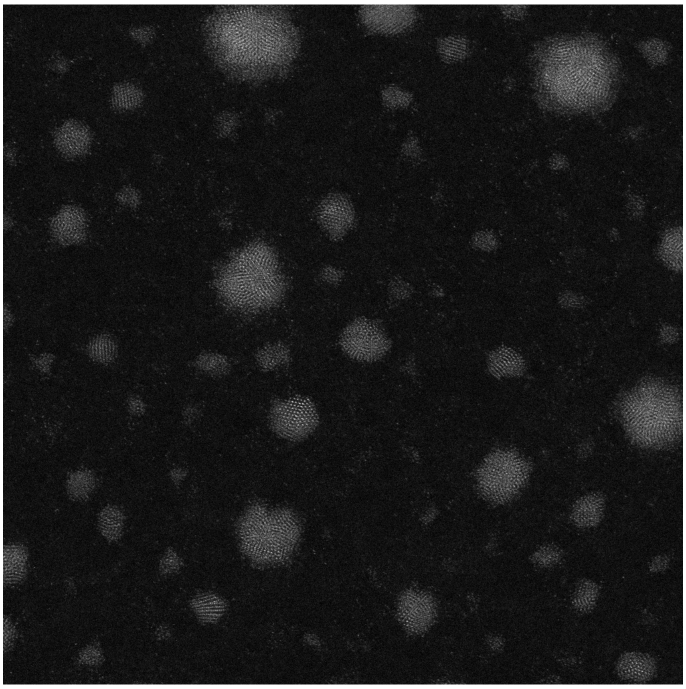

Figure 5.9: Example illustration of clusters size distribution from high coverage (Ag9) HAADF-STEM image.

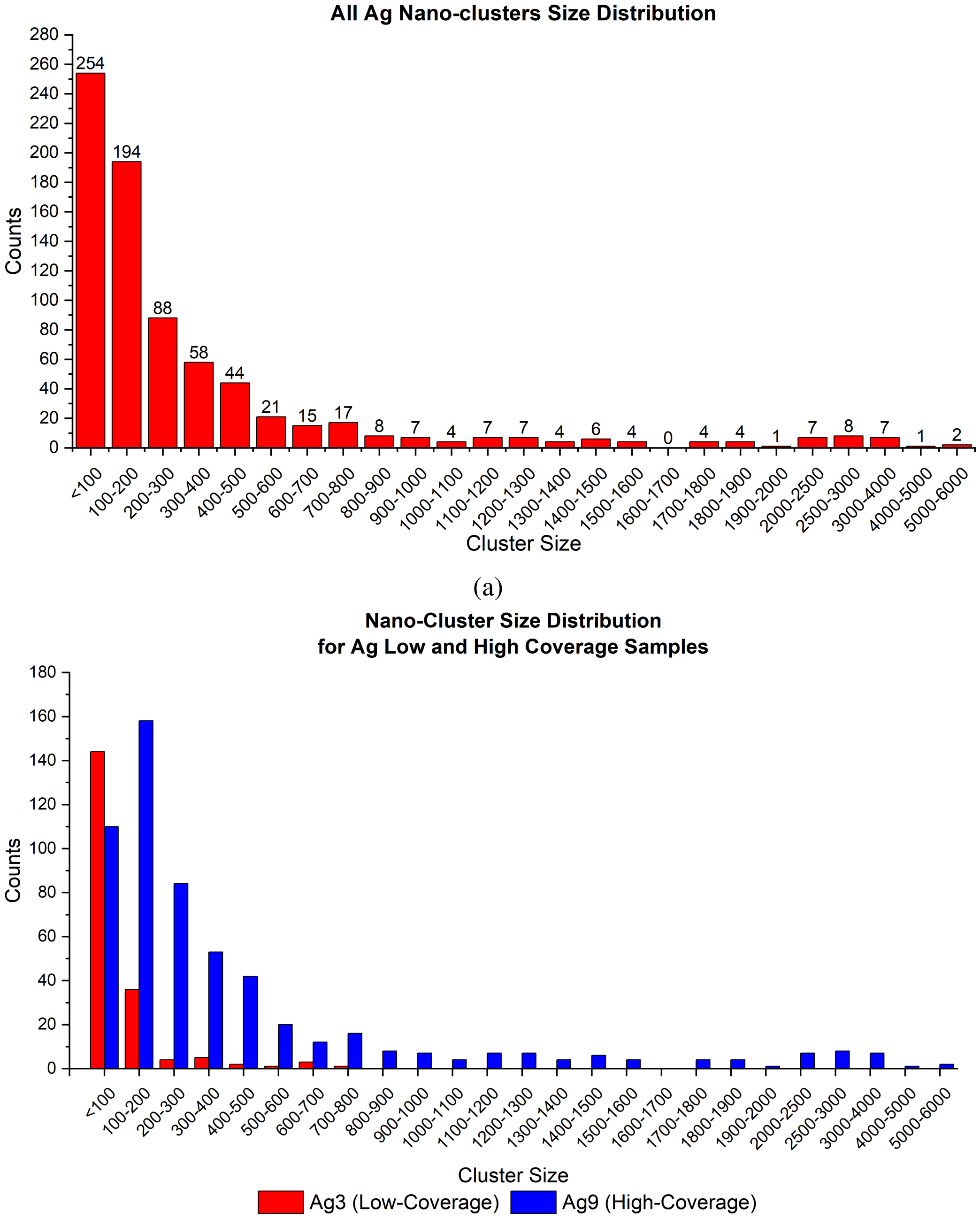

(a)

(b)

Figure 5.10: Summary plot of the size distribution for all analysed Ag nanoclusters from captured HAADF-STEM images displayed as a) A sum of all nanoclusters, b) A function of the sample set.

Preliminary investigations of the size of produced nanoclusters as a whole showed an immediate trend in the size distribution as well as posing some interesting questions on the nature of cluster growth based on the pattern of the distributions shown. As Figure 5.10a demonstrates, the quantity of clusters was shown to decrease significantly as the cluster size increased. This was particularly rapid in the area below *300* atoms in size where counts dropped from *254* and *194* to *88* for the *¡100*, *100-200*, and *200-*

300 size rnages respectively. Overall analysis showed how 90% of grown clusters were found at sizes below *800* atoms, 70% of all clusters could be found at sizes below *300* atoms, and 33% below *100* atoms in size. This initially suggests that cluster production through the use of the Matrix Assembly method, primarily results in the production on nanoclusters in the sub-200 atom size range. Above *800* atoms, there were numerous appearances of larger clusters up to *6000* atoms in size however, these were rare occurrences with counts below *10* in number. The presence of an increased cluster count in the *1-100* and *100-200* size regime, and knowledge that clusters were deposited at cryo energies suggested that the majority of deposited particles were at sizes in the range of *10's* to *200* atoms. As a result, this also suggests that growth of larger clusters primarily occurs as a result of nucleation from depositing particles into larger nanoclusters. This would become more evident in the individual sample analysis where different deposition conditions were used and the effect of deposition rate and time could easily be seen.

Analysis of the low coverage sample as shown in red in Figure 5.10b which was sputtered at low current for a short period *(10 secs)*, demonstrated a similar trend to that of the overall analysis though on a smaller scale. Here the range in cluster sizes was shown to be up to *800* atoms in size with the majority of clusters being below *100* atoms in size. The short period and low power sputtering here made it clear to see that the majority of particles were *sub-100* atoms in size. It could therefore be strongly argued that the primary size of nanocluster produced through Matrix-Assembly is in the range of *10's* atoms up to *100* atoms in size. This was supported by the low flux that would be present as a result of the low sputtering current, this combined with the short deposition period which would leave little time for nucleation from depositing particles in combination with the further low likelihood due to a low sample coverage. The sharp decrease in cluster counts above *100* atoms in size further supports this where continued growth would require a higher cluster presence, this could only be achieved from an increase in sputtering current, sputtering time, or a combination of both. This is demonstrated in the higher coverage sample. Minor peaks were visually distinguishable however at larger sizes, specifically in the *300-400* atom and *600-700* atom range. The first of these minor peaks corresponds with the metastable magic number of *309* atoms suggesting that this peak was the result of metastable nanocluster formation. The second peak however did not align with any magic number previously mentioned. The closest magic number to this peak would be *561* atoms in size. With the difference here being approximately *100* atoms, this peak location suggested that the nanoclusters here may have only just surpassed the *561* atom metastable atom cluster size and found a state of partial metastability. Here the added atoms could be a result of continued nucleation from depositing particles as well as possible aggregation of smaller *sub-100* atom nanoclusters.

The higher coverage sample as shown in blue in Figure 5.10b, which was sputtered at a higher current and longer duration *(60 secs)*, demonstrated a different trend than the low coverage sample. Here the increased flux and exposure time did indeed result in a wider size distribution. In this sample the size distribution was shown to range up to *6000* atoms, the majority of this however, was still shown to be at the smaller end of this size scale. In this sample the first peak had in fact shifted to the *100-200* atom regime suggesting that the increased sputtering current and time, yielding a higher coverage, may lead to a greater degree of surface aggregation from adjacent clusters as they grow. Here this peak was also found to correspond with the known metastable nanocluster size of *141* atoms. The high flux and quick nucleation in such a deposition would explain the nature of the size distribution, particularly at smaller sizes. With the expected size of deposited clusters being on the *10's* of atoms scale, aggregation of adjacent clusters could be argued to be the main reason behind the appearance of clusters on the *1000's* of atoms scale where nucleation from depositing clusters would have less of an impact than aggregation from clusters containing *100's* of atoms. This is once again supported by the significantly lower count of clusters at larger sizes where once aggregation has occurred, a vacant space remains which is not quickly refilled. As with the lower coverage sample, minor peaks could also be seen at higher nanocluster sizes, specifically; *700-800, 900-1000, 1100-1300, 1400-1500,* and *1700-1900* atoms. It was only two of these peaks however that aligned with known magic numbers; *923*, and *1415*, and could therefore be suggested to be metastability locations. The remaining three peaks however were found to be approximately in the middle of magic number locations and hence the locations of these peaks offer some confusion. In this case it could be argued that the nanoclusters here had found a state of partial metastability, perhaps influenced by the nature of the nanoclusters orientation on the surface as well as a number of surrounding nanoclusters close enough to allow further aggregation to a fully metastable size.

On review, results have clearly demonstrated the growth mechanism of clusters produced through Matrix-Assembly where the primary size of pre-deposited nanocluster is shown to be in the sub-100nm range. The effects of deposition flux and time were also clearly demonstrated here where it was shown how an increase in both, yielded a proportionate response in cluster size and count. To understand the effect each parameter has respectively, this experiment could be repeated again with an extra two condition sets; low current high deposition time, and high current low deposition time. Repeating this experiment in this way would allow for a better understanding of the effect of each parameter when applied to this Matrix-Assembly method further enhancing production knowledge and the ability to tune the results of this method to produce nanoclusters of specific sizes.

Cluster Isomer Distribution

The second stage of analysis of produced nanoclusters involved categorisation by structural isomer where possible. Here identified nanoclusters were visually compared with an existing simulation atlas for Face-Centered-Cubic (FCC), Decahedral (Dh), and Icosahedral (Ih) nanocluster isomers, as illustrated in Figure 5.11b. Where categorisation was not possible, nanoclusters were marked as Unidentifiable/Amorphous (U/A). From this, isomer distributions could be determined and patterns could be established when combined with sizing information. The results of this analysis are described below.

Review of Ag samples as a whole demonstrated how one particular isomer structure was dominant above the others, excluding those that are unidentifiable or amorphous. As demonstrated in Figure 5.11c, the Icosahedral structure was found to be preferred making up approximately 1/3 of all nanoclusters. Furthermore, Figure 5.11a shows how this isomer was not isolated to a particular size range but was in fact present throughout all found sizes with similar population densities. The exception to this was below 200 atoms in size where Icosahedral was found to be particularly favourable. Above this, between 200-400 atoms in size, isomeric structures were shown to be closely competitive with the FCC structure initially showing to be dominant. This has been previously demonstrated by Mottet et al. where Ih, Dh, and FCC isomer energies are theoretically shown to be highly competitive below 300 atoms. Above this it is only Dh and FCC which remain competitive [123]. In this work, above 400 atoms however, FCC structure popularity quickly diminished in favour of Icosahedra. The Icosahedral structure remained the preferred structure throughout the larger sizes with the occasional competition from Decahedral structures. This was contrary to theoretical simulations. Overall, it could be seen that the main population of FCC structures were seen in the range of 100 to 500 atoms with a central peak between 200 and 300 atoms. Decahedral similarly observes its main population in the range of 1 to 700 atoms with a smoothed peak between 200 and 500 atoms which could possibly be two hidden gaussian peaks located at 200-300 atoms and 400-500 atoms. For the Icosahedral isomer structure a dominant presence was observed throughout the analysed size range, particularly in the sub 200 atom range as previously stated, contrary to theoretical work [123]. One possible explanation for this could be in the modelling difference of the nanoclusters between theoretical and practical. In particular, where simulations often assume a symmetrical structure, in practice structures are often asymmetrical. What remained interesting in this analysis was that the locations of these central peaks above 200 atoms all existed just before identified magic numbers and hence metastable structures. This suggested that these particular nanoclusters have found metastability through other means with one solution being the exposure to air and natural oxidisation which could also account for the dominant Icosahedral isomer of these nanoclusters, for which Ag is a natural FCC orientated material. This is supported in previous works where Icosahera stabilisation is observed in Ag nanoclusters that had adsorbed methanethiol producing ligands containing carbon, sulphur, and hydrogen [124].

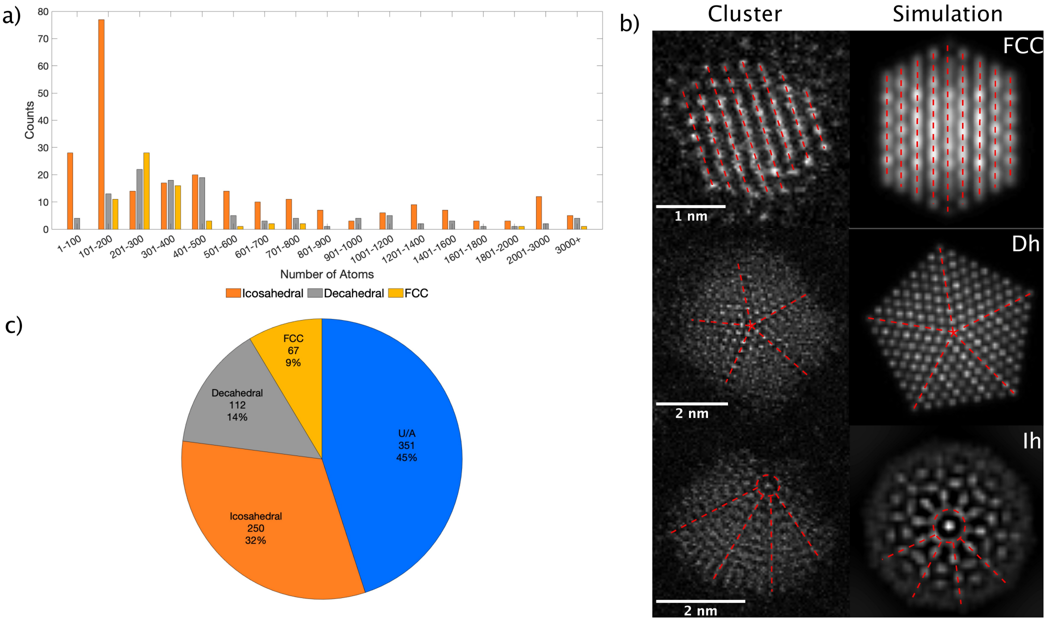

Figure 5.11: Size distribution and statistical analysis of the isomer proportions for Silver nanoparticles exposed to air on amorphous carbon. a) Number of clusters as a function of size in the range of 1-3000 atoms, split into the different isomer structures observed. b) HAADF-STEM images of three different morphologies and their corresponding assignments using the Simulation Atlas method; Face-centred cubic (FCC), decahedral (Dh), and icosahedral (Ih) with 309, 1233, and 835 atoms, respectively. Dotted red lines and red circles area as a guide for the eye. c) Statistics for silver cluster symmetries averaged over the whole size range of (a). The U/A assignments correspond to unidentified or amorphous (glassy) structures [125].

Effects of growth conditions could further be determined by breaking down this analysis to look at individual samples where deposition time and flux where different. As already shown, the change in conditions had a strong effect on maximum size of grown nanoclusters. Here the effect of structure was analysed for each sample to determine the influence of flux and sputter time on end nanocluster structures.

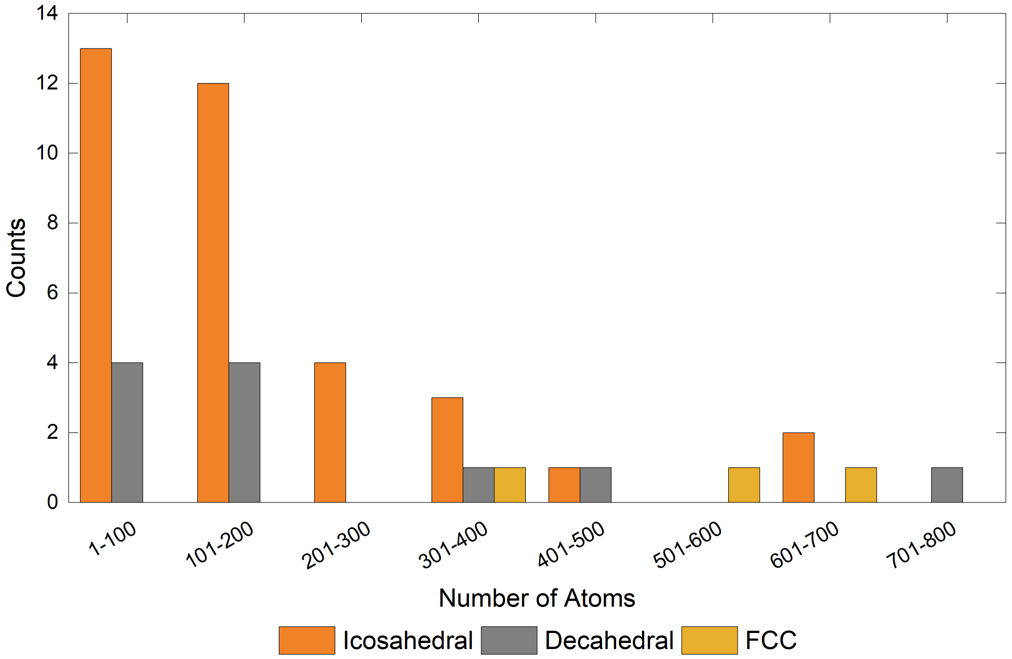

Figure 5.12: Size distribution for identifiable isomers; Icosahedral (Ih), Decahedral (Dh), and Face-centred cubic (FCC), in the Ag3 low coverage sample in the range of 1-800 atoms.

The identifiable isomer distribution for the lower coverage sample (Ag3) can be seen above in Figure 5.12. Upon first inspection it could be noticed that only a small portion of identified nanoclusters could be further structurally identified. For this sample 75% of identified nanoclusters were unable to be linked to a single isomer and hence were catergorised as unidentified/amorphous (U/A). Immediately, this suggested a link between the rate of particle/nanocluster deposition (flux) and the ability of formed nanoclusters to settle into stable isomers. The ability to form metastable isomers is usually a size related factor, however evidence here leads to suggest that amorphous or glassy nanoclusters are more common in low flux, low sputter time conditions. Of the identifiable nanoclusters in this sample, it was once again noticed that the icosahedral isomer was generally preferred. As mentioned previously, theory work showed that below 200 atoms the icosahedral structure is preferred which was reflected here [123]. This continues marginally in the 200-400 size range. Above 400 atoms in size however, the results from analysis of this sample suggested competition between all three isomer types. This once again contradicts theoretical studies where only decahedral and FCC were shown to be competitive in larger nanoclusters [123]. Further detailed analysis and experimentation is require to draw solid conclusions on these patterns.

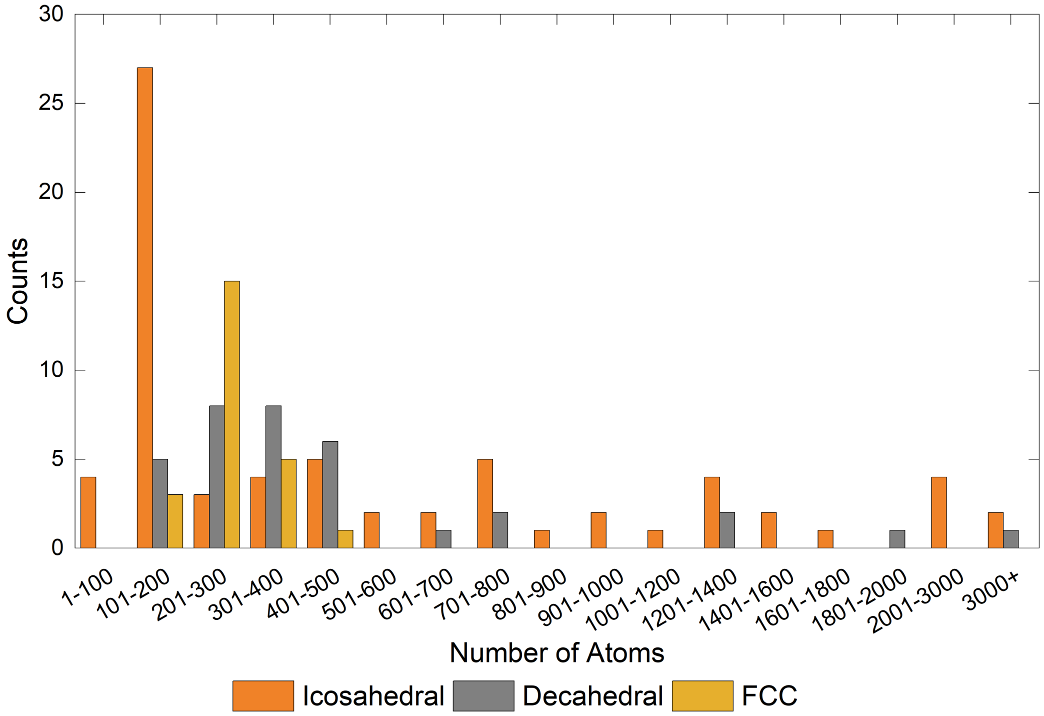

Figure 5.13: Size distribution for identifiable isomers; Icosahedral (Ih), Decahedral (Dh), and Face-centred cubic (FCC), in the Ag9 high coverage sample in the range of 1-3000+ atoms where clusters above 3000 atoms in size have been binned together.

In comparison, results from the higher coverage sample yielded a higher sample size, with only 35% of all nanoclusters in this sample being unidentifiable. This further supported the earlier hypothesis that particle/nanocluster flux and deposition time influence the ability of deposited nanoclusters to form metastable structures. As in the low coverage sample, the icosahedra isomer type was shown to be the most preferred here as demonstrated in Figure 5.13. This was particular above 500 atoms where, aside from the occasional decahedral structure, icosahedra were shown to be the only isomer structure present. This was in direct contradiction to theoretical work where in this size range the competing isomers should be Dh and FCC. Below 200 atoms in size, as in the low coverage sample, icosahedra were shown to be very dominant. Theory here did support this finding where the icosahedral structure has been shown to have the lowest energy in this size range [123]. Between 200 and 500 atoms in size, a great deal of competition between all three isomers was demonstrated where initially decahedral and FCC were shown to be particularly preferred. Overall in this region it appeared the decahedral isomer structure was energetically preferred and this was supported by theory where the energies of the three isomers at these sizes were shown to be very close with decahedral having the lowest energy [123].

The continued preference of icosahedral structures at larger sizes was difficult to explain with a number of possible factors potentially influencing this. One potential answer could be the growth mechanism used where single atoms and nanoclusters were sputtered from an argon matrix and hence not an example of true free cluster growth. A more likely explanation for this trait however, would be the nature of Ag itself and its tendency to oxidise very easily. As discussed in *Paper II, Vernieres et al.*, the nanoclusters produced here were not protected from air exposure prior to imaging and hence these nanoclusters can be considered contaminated. It was therefore suggested that the exposure to air and hence oxidisation of Ag as well as adsorption of sulphur molecules has destabilised these Ag nanoclusters leading to the prevalence of the icosahedral isomer structure.

5.3 Summary

Nanoclusters synthesised through matrix-assembly and imaged using AC-STEM by Dr Thomas Slater at Diamond Light Source, have been analysed here using image processing software. Silver (Ag) nanoclusters produced by Erica Watchorn-Rokutan using a matrix-assembly method have been investigated to understand and characterise their atomic size as well as isomeric structures. A concentric ring method was employed, initially through manual analysis before evolving into a more automated macro, to measure the area and HAADF intensity of nanoparticles. Single atoms were analysed to provide a calibration point for size estimation of larger nanoclusters where atomic size was determined through division of nanocluster HAADF intensity by the calibrated single atom HAADF intensity. The isomeric structure of nanoclusters was determined through visual comparison with an existing simulation atlas where results were categorised as either Icosahedral (Ih), Decahedral (Dh), Face-Centred-Cubic (FCC), or Unidentifiable/Amorphous (U/A).

Silver (Ag) nanoclusters were analysed from two samples; low-coverage, and high-coverage, synthesised by varying the sputter current and deposition time. Atomic sizing of the nanoclusters was performed as previously mentioned using a concentric ring method. Sizes were shown to vary significantly between low and high-coverage samples with low-coverage sizes limited to *800* atoms and high-coverage nanoclusters up to sizes of *6000* atoms. For the low-coverage sample, the majority of nanoclusters were shown to exist below *100* atoms with a quick decrease in cluster counts above this value. Gaussian distribution peaks could be noticed at *300-400* and *600-700* atoms in size with the former corresponding to the metastable magic number of *309* atoms. The high proportion of nanoclusters in the sub-100 atom range however, corresponded to the reduced particle flux thus restricting the rate of particle growth and ultimately the maximum size of nanoclusters. The higher coverage sample, which was exposed to a higher particle flux and longer deposition time, in contrast demonstrated not only a high number of nanoclusters in general but also a larger maximum nanocluster size. As with the lower coverage sample, the majority of nanoclusters here could be found at smaller sizes however, here a Gaussian distribution is seen with a centre in the *100-200* size regime corresponding to the *141* atom magic number. Above this a number of minor Gaussian peaks were further distinguishable although only two could be related to known magic number sizes at *923* and *1415* atoms. The remaining peaks were noticeably located in the middle of magic numbers. The presence of increased counts in sub-100 atom sizes further suggested that the primary size of sputtered and pre-deposited cluster from the matrix-assembly method was in the order of *10's* atoms. The known exposure to air suggested a potential level of partial stability at these sizes offered by O2 and S contaminants. From these results it was clear that the sputtered particle flux had a strong influence on final nanocluster size however, further investigation by controlling the sputter current and deposition time singularly could yield further insight into the direct contribution of each parameter.

Visual inspection of grown Ag nanoclusters also allowed for understanding of isomer popularity in these sample sets. Overall, analysis demonstrated that of the identifiable isomers structures the icosahedral structure was found to be the most preferred with approximately one third of all nanoclusters settling in this state. This population was not found to be isolated to a single size range either with it being found across all sizes. Below *500* atoms the decahedral and FCC isomer structures were also shown to be closely competitive boasting a strong appearance. Above this size however, the decahedral and FCC isomer structures were shown to quickly diminish in favour of icosahedra. This was found to be in contradiction to previous theoretical work where a dominance of Dh and FCC should be expected [123]. The highly oxidising nature of Ag and exposure to atmosphere was believed to offer a solution to this however, where it was suggested that O2 and S contamination was thought to contribute to the settling of nanoclusters in a icosahedral structure. Specific and comparative analysis between the two samples further identified the effects of particle flux on the metastability of nanocluster isomers. It was shown that increased sputter flux yielded a higher population of identifiable nanoclusters with the percentage of U/A nanoclusters dropping from 75% to 35% between the low-coverage and high-coverage samples respectively. In both samples icosahedra were shown to be the more energetically favourable overall however, the dominance between individual samples was seen to be quite different. In the low-coverage sample it could be seen that the icosahedral isomer structure is highly preferred particularly at lower sizes with the Dh and FCC isomer structure only making the occasional appearance. In contrast the high-coverage sample demonstrated a more diverse appearance from all three isomers. The icosahedral isomer structure could be seen to be present across the majority of the size range and was particularly popular in the *100-200* atom size range corresponding to the *141* atom magic number. Between *200* and *500* atoms however, the Dh and FCC isomer structures were shown to be more dominant and fairly competitive. Above this however only icosahedra are seen with only the rare appearance of decahedral nanoclusters once again in contradiction of theoretical studies [123]. This again suggested an external influence causing the dominance of icosahedra where atmospheric exposure was thought to be the main contributor. This was supported by previous work where exposure to similar contaminants had resulted in icosahera stabilised nanoclusters.

Chapter 6

ATOMIC STRUCTURE INVESTIGATIONS OF Au NANOCLUSTERS ON AMORPHOUS CARBON

Overview

This chapter will present, discuss, and summarise the methods and results of Au nanocluster investigations through AC-STEM. Analysis will include size estimation through HAADF Intensity and single atom calibration, Quasi-Shape and Isomer structure determination. These results are summarised at the end of this chapter as well as in Paper III: Characterization of the Morphology of Surface-Assembled Au nanoclusters on Amorphous Carbon, and Paper IV: Stabilization of 2D Raft Structures of Au nanoclusters with up to 60 Atoms by a Carbon Support.

6.1 Gold Nanoclusters

In this section of the chapter, the results of analysis into the size and structures of Gold (Au) nanoclusters produced by thin film sputtering and surface aggregation, will be presented and discussed. This will include a brief introduction into the synthesis method used followed by the results of size and structure analysis, which will be divided between Single Atom Intensity, 3D Cluster, and 2D Raft investigations.

6.1.1 Thermal/E-Beam Evaporation and Ion Sputtering

Deposition and growth of Au nanoclusters investigated in this thesis was performed by Dr James McCormack using the Mini Matrix Assembly Cluster Source (miniMACS), operated as a sputter deposition source. In this method of operation, a gold film was first grown on a copper support via Thermal/E-Beam evaporation forming a bulk layer of gold on the support. Once the bulk gold thin film was deposited, an argon ion beam was directed towards the thin film at an approximate 10° angle relative to the support. The resulting interaction sputtered the grown gold film ejecting thermally energised gold atoms towards a sample substrate, in this case being Holey-Carbon TEM grids. As a result of the energetic nature of the of the ejected gold atoms, once deposited onto the amorphous carbon surface, the atoms diffuse across the surface and aggregate with other deposited gold atoms growing to form nanostructures such as nanoclusters. As it will be shown in the following sections, it was believed that the main method for nanostructure growth from this process was the Vollmer-Weber method as described in Section 2.1.3. This synthesis method is illustrated below in Figure 6.1.

In this method, samples were produced at three argon ion beam accelerating voltages; 2 kV, 3 kV, and 4 kV, where the increase in accelerating voltage increased the argon ion energy and therefore the Au sputtered atom flux. As a result of this method for nanoparticle synthesis, the size of the grown nanostructures could not be controlled. Nanostructure size was instead influenced by a number of parameters such as accelerating energy and surface-interaction therefore, as will be demonstrated, sizes of deposited and grown nanostructures varied greatly.

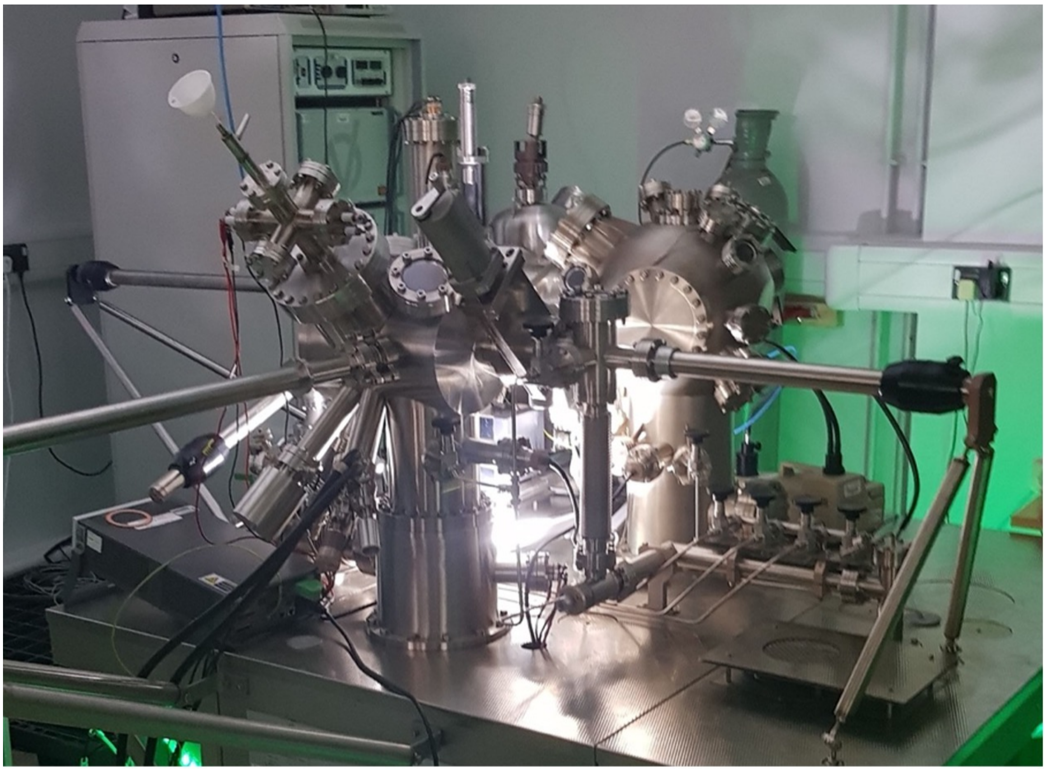

(a)

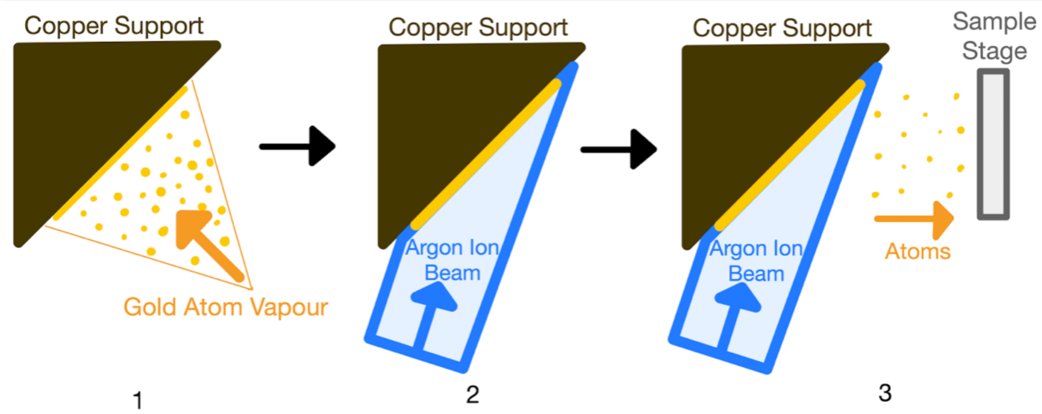

(b)

Figure 6.1: Photograph of the device used and deposition method described for Au cluster synthesis. a) MiniMACS setup, b) Three stage representation of the deposition method used in this work, after [126]. Inside the miniMACS a copper support is coated with gold atoms produced by thermal evaporation. The thin film grown is then sputtered by Ar^+ beam causing energetic atoms to be directed and deposited onto the sample surface.

6.1.2 Size and Structure Analysis

In order to perform analysis and further characterise grown Au nanostructures, produced samples first needed to be imaged under HAADF-STEM. The samples in this thesis were imaged by Dr Thomas Slater at the Electron Physical Sciences Imaging Centre at Diamond Light Source using the JEOL ARM300CF Electron Microscope as detailed in Section 2.2.5. Imaging was carried out in STEM mode using a HAADF detector (58 mrad inner angle, 215 mrad outer angle) at and accelerating voltage of 300 kV and beam current of 25 pA. Data was obtained at four magnifications: 5 Mx, 8 Mx, 10 Mx, and 15 Mx, producing a variety of images from which analysis could be performed as exampled below in Figure 6.2. In total 19 datasets were obtained for analysis, the details and results from such analysis is presented below.

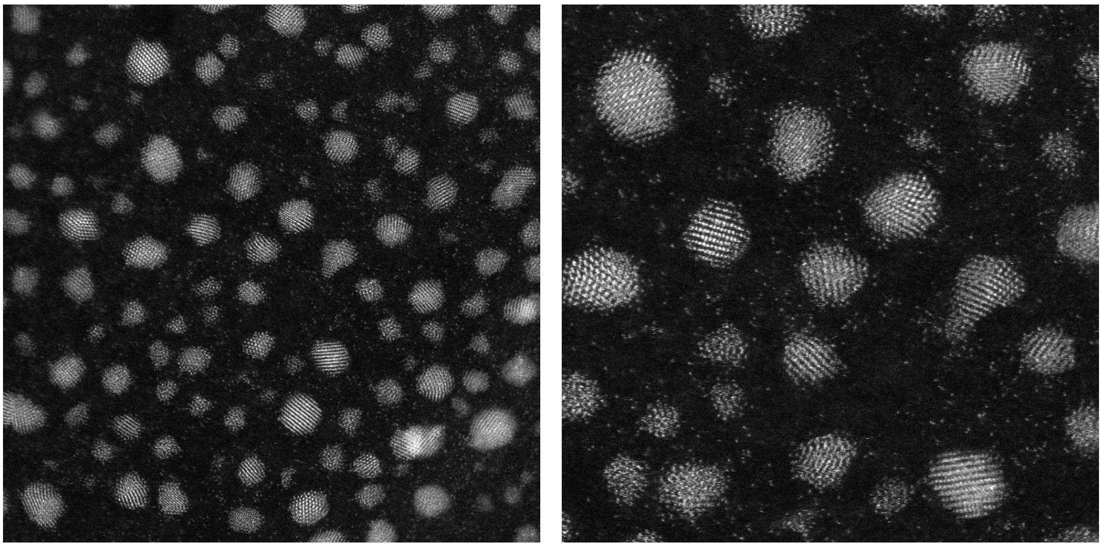

(a) (b)

Figure 6.2: Example HAADF-STEM images of Au nanoclusters at a) 5Mx, and b) 10Mx, produced by thermal evaporation and ion sputtering by Dr James McCormack and imaged by Dr Thomas Slater.

Single Atom Intensities

As detailed in the previous chapter, the first stage in analysis of obtained HAADF-STEM images was to determine the correct intensity of single atoms within each of the datasets. Correct single atom intensity calibration was necessary for accurate approximation of corresponding nanocluster sizes. This was carried out using the concentric ring method, initially through manual analysis before evolving into an automated script whereby a larger sample size could be analysed for better accuracy, as previously mentioned. A comparison of the two approaches is demonstrated below where, the mean, standard deviation, and relative standard deviations have been calculated for method comparison in Table 6.1. Furthermore, the individual dataset approximated single atom intensities from each approach have been plotted in Figure 6.3.

Table 6.1: Statistical analysis of calibrated Au single atom intensities against magnification showing mean, standard deviation, and relative standard deviation.

	10 Point Sample Size			**Multi-Point Sample Size**		
Magnification	**Mean Single-Atom Intensity**	**Standard Deviation**	**Relative Standard Deviation**	**Mean Single-Atom Intensity**	**Standard Deviation**	**Relative Standard Deviation**
5 Mx	9.54E+05	4.50E+05	47.15%	6.63E+05	8.34E+04	12.57%
8 Mx	1.18E+06	9.10E+04	7.69%	9.84E+05	1.15E+05	11.71%
10 Mx	1.59E+06	1.69E+05	10.67%	1.16E+06	1.08E+05	9.38%
15 Mx	2.29E+06	-	-	1.92E+06	-	-

From Table 6.1, on comparing the values from each approach it could be seen immediately that the mean single atom intensity for each magnification had dropped in the *Multi-Point* approach. This indicated that in general, previously estimated single atom intensities were incorrect and were calculated from a mix of monomers, dimers, and trimers, indistinguishable within a small sample size, thus resulting in a higher calibrated single atom intensity. Furthermore, it could be seen that use of the *Multi-Point* method had decreased the standard deviations between datasets at two magnifications as a results of an increased sample size. This was particularly pronounced in the 5 Mx datasets where the relative standard deviation had decreased from 47% to 12%. In the 8 Mx datasets the relative standard deviation was shown to increase slightly, indicating the new calculated single atom intensities were more dispersed than found in the previous method. This however, was not an indication that the new value for single atom intensity was incorrect but more a reflection of fluctuation in imaging conditions between each dataset.

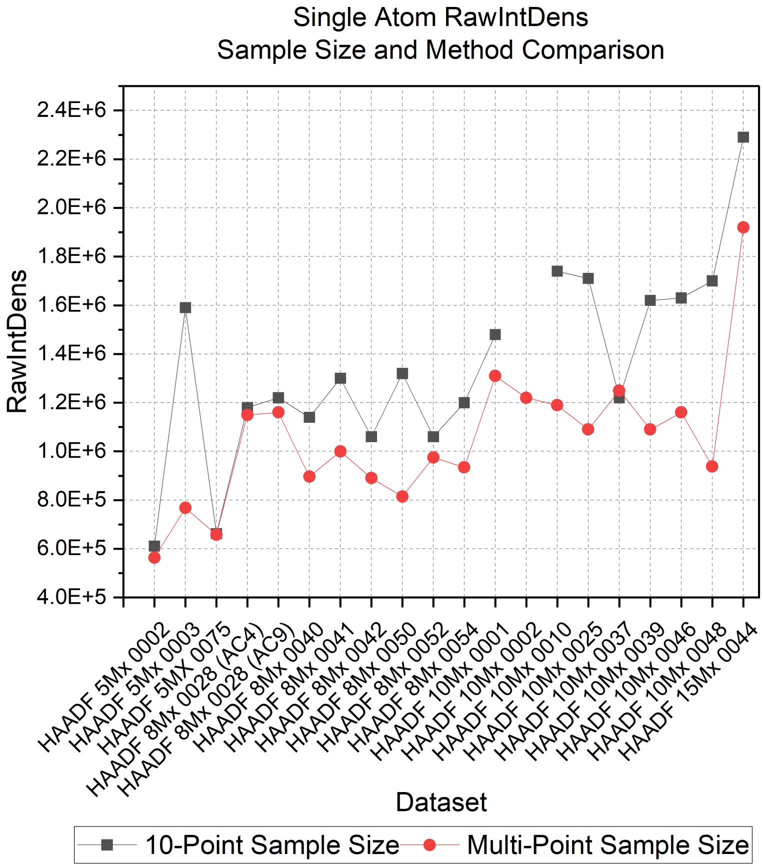

Figure 6.3: Dataset vs RawIntDens plot for single atom intensities obtained through sample sizes of 10 vs sample size in order of 100s (Multi-Point).

In Figure 6.3, it could be seen that the increased sample size and monomer/dimer/trimer intensity filtering in histograms had produced a general decrease in single atom intensity across all datasets, further illustrating the results showed in Table 6.1. It could be seen that the degree of change in calibrated single atom intensity between each approach, varied heavily across the datasets with some demonstrating similar values and others showing high degrees of change. This furthermore indicated how selected datasets had previously been calibrated using a mixture of monomer, dimer, and trimers, thus resulting in incorrect calibration. This therefore, emphasises the importance of sampling a large portion of data for calibration in this method. On re-calculation of nanocluster sizes using the revised single atom intensities from the multi-point method, and comparison with previous work by Young et al., nanocluster atom counts vs diameters were found to be more in line with previous results. Plotting of the mean intensity values against image magnification with fit analysis using a 2^{nd} order polynomial, as seen below in Figure 6.4, demonstrated the accuracy of these results.

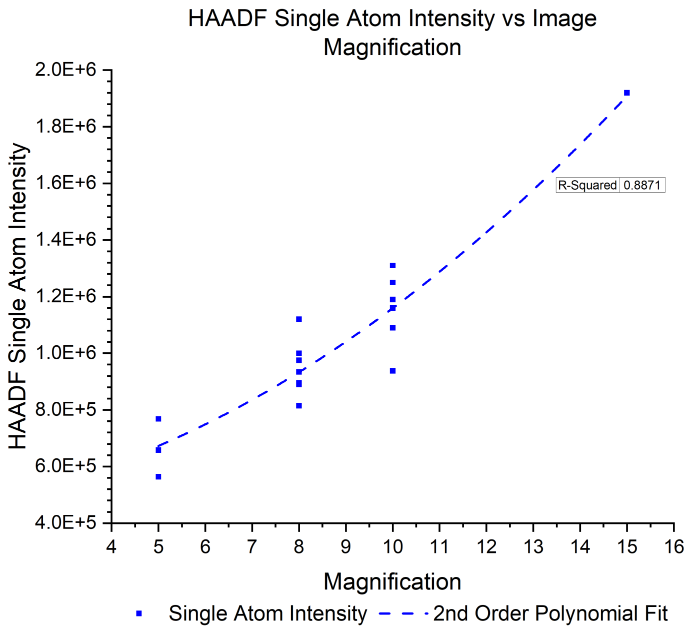

Figure 6.4: Mean HAADF intensities vs magnifications plot for Au single atoms across datasets demonstrating calibration accuracy.

Here, the variation in single atom intensity approximations from the multi-point method can be effectively compared with the curve of best fit. Figure 6.4 demonstrates how the calculated single atom intensities align well with the expected 2^{nd} order polynomial fit from increasing magnification. The calibrated curve of best fit demonstrates an R^2 value of *0.8871* showing a high degree of accuracy.

Cluster Size Distribution

Upon successful calibration of single atom intensities for each acquired HAADF-STEM image, estimation of larger nanocluster sizes could be performed. Using the concentric ring method described in Figure 5.1 and Equation (5.7), the approximate number of atoms in each measured cluster could be identified. As in the single atom intensity analysis, intensity calculations were performed using the *RawIntDens* value resulting in a single *Raw Integrated Density* value from which the nanocluster size could be derived. Once final calculation of nanocluster sizes was performed, analysis of cluster sizes obtained via ion sputtering and surface aggregation could be carried out through plotting of results in a histogram. As with the Silver nanoclusters, plotting in this way allowed for a more effective analysis and visualisation of size distribution. The size distribution observed for all clusters in this analysis is illustrated below in Figure 6.5.

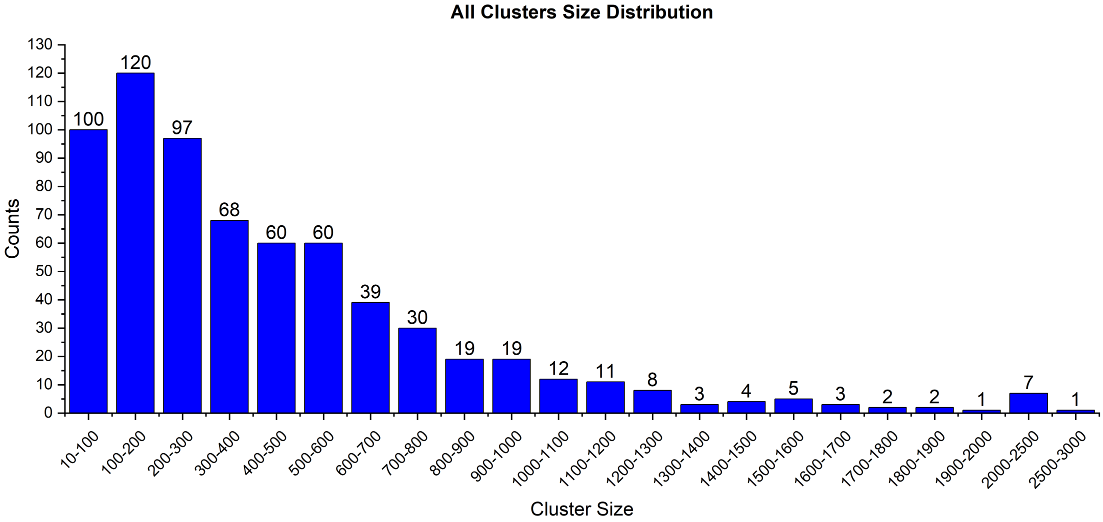

Figure 6.5: Summary plot of the size distribution for all analysed Au nanoclusters from captured HAADF-STEM images.

Initial size analysis of all identified clusters demonstrated an immediate trend and limitation in grown cluster sizes. As shown in Figure 6.5, it could be seen that as the size of clusters increased, their frequency decreased. Reviewing the distribution of these cluster sizes revealed how 90% of grown clusters could be found at sizes below 1000 atoms, with 75% below 600 atoms, and approximately 50% below 300 atoms in size. Within this distribution, a number of gaussian peaks can be seen indicating common stability sizes for grown nanoclusters. Here peaks are noticeable at 100-200, 500-600, 900-1000, 1500-1600, and 2000-2500 atoms. The locations of these peaks reasonably coincide with known the metastable nanoclusters sizes 147, 561, 923, 1415, and 2054 [34, 35]. The increased concentration of formed nanoclusters at smaller sizes can partially be explained by the knowledge that the size of deposited particles are in the order of a few atoms however, a number of additional factors also influence nanocluster growth including; surface orientation, deposited adatom/adparticle concentrations and energies, as well as incoming sputtered atom flux. In the general context of all analysed nanoclusters, surface structure, and existing adatom/adparticle concentrations will be discussed.

For clarification, the terms “adatom” and “adparticle” refer to an atom or particle with sufficient energy to move across a substrates’ surface (Diffuse) however, has not gained enough energy to escape the surface in sputtering [127]. As previously described, in this work nanoclusters were synthesised through deposition of thermally energised, and thus soft landed, Au atoms on an amorphous carbon substrate. The energetic nature of these adatoms and adparticles meant that upon deposition, surface diffusion occurs where collision and interaction with other adatoms and adparticles leads to the formation and growth of atomic-clusters [128, 129]. The efficiency of the diffusion process however, was highly dependent on the substrate surface characteristics such as; surface orientation and defect concentration. This in turn determined how easy it was for atoms to diffuse across the surface and thus collide and grow into atomic clusters [128, 129]. The amorphous nature of the substrate in this study meant there was a higher probability of surface defects and differences in orientation which could impact diffusion. This effect could also be seen to be mitigated by the high atomic size difference between the surface material; Carbon, and the deposition material; Gold. In order for nanocluster growth to occur, the process required the repeated collision of adatoms and adparticles to form nanoclusters. Initially, for single atoms and small clusters this probability of collision could be seen as high as the density of atoms and small particles was also high, thus the distance between an atoms nearest neighbour was quite small. However, as atoms and particles on the surface continue to coalesce into single particles the density of single particles begins to decrease therefore decreasing the probability of collisions and thus making it harder for nanoclusters of larger sizes to grow. This is reflected in Figure 6.5, which demonstrates how as the nanocluster size increases, their frequency decreases.

In this study, depositions were carried out at three sputtering voltages (2 kV, 3 kV, 4 kV). By further grouping nanoclusters by their sputtering voltage, further investigation into the effect of sputtering energy and sputtered atom flux on the end sizes of grown nanoclusters. Example HAADF-STEM images of nanoclusters sputtered at 2kV, 3kV, and 4kV are shown below in Figure 6.6a-c respectively to demonstrate size variations. The size distribution plots of analysed nanoclusters as a property of their sputtering energy is illustrated below in Figure 6.7.

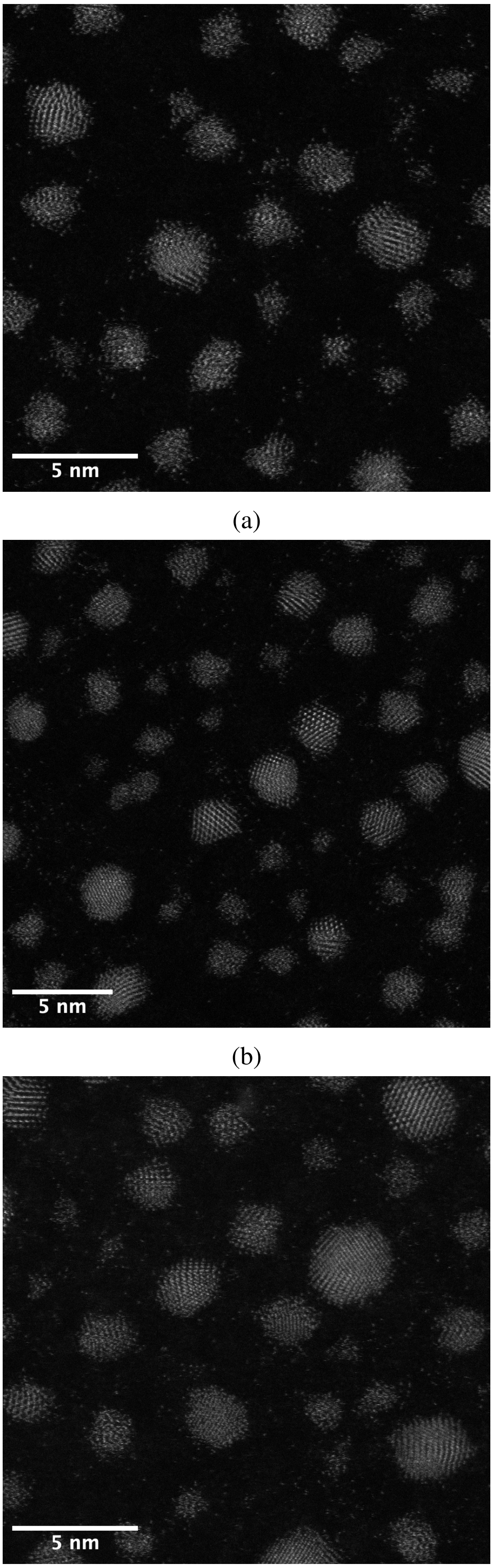

(a)

(b)

(c)

Figure 6.6: HAADF-STEM images from a) 2kV, b) 3kV, and c) 4kV samples.

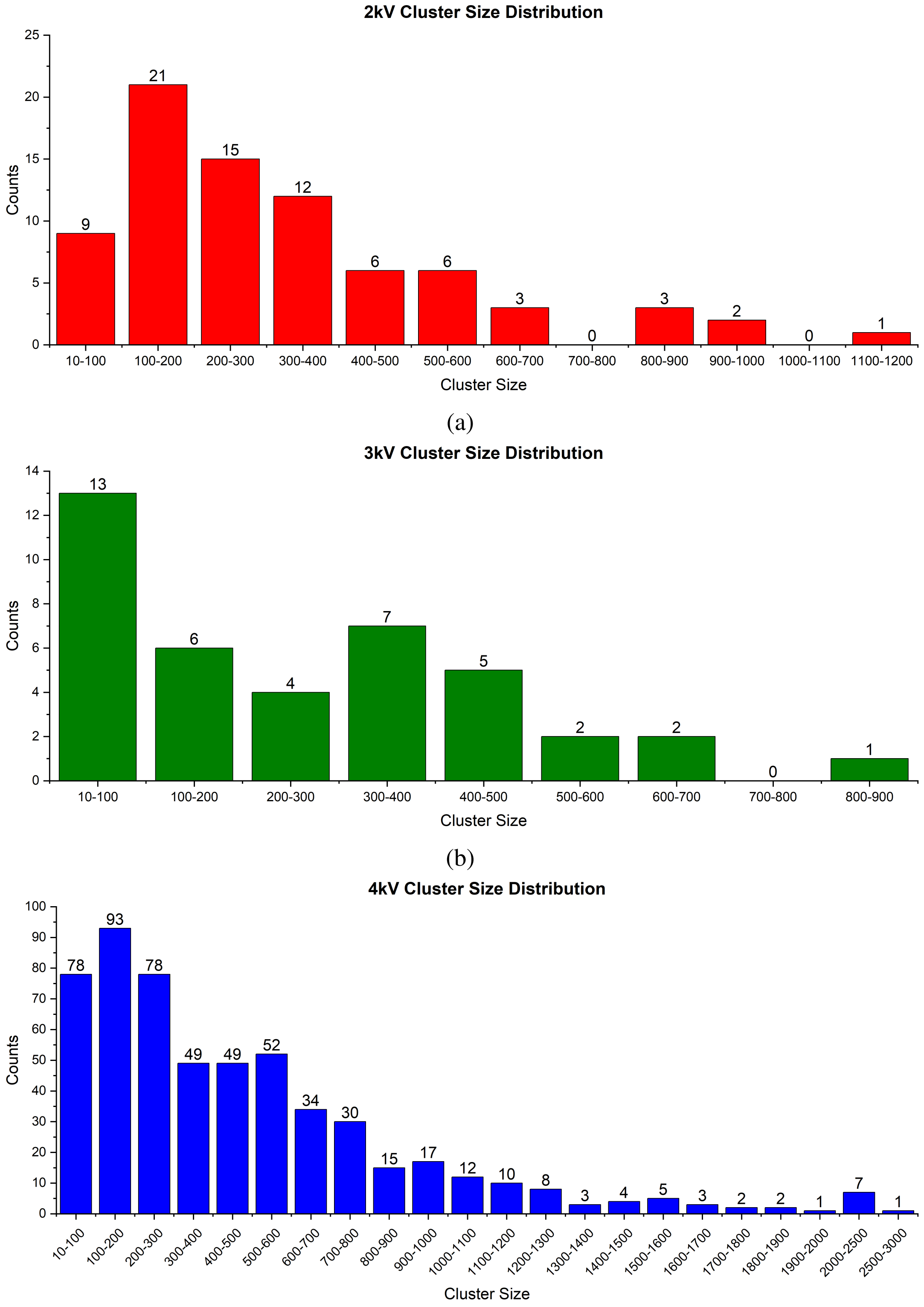

(a)

(b)

(c)

Figure 6.7: Au cluster size distribution plots for varied sputter voltages. a) Cluster size distribution for sputtering at 2 kV, b) Cluster size distribution for sputtering at 3 kV, c) Cluster size distribution for sputtering at 4 kV.

On first inspection it could be seen that a significant difference in maximum nanocluster size was displayed between argon ion accelerating voltages, with sizes up to 1200 and 900 atoms found in 2 kV and 3 kV images respectively, and up to 3000 atoms found in 4 kV images. From the increase in maximum cluster size found in 4 kV images, it could be reasonably suggested that the maximum achievable size of nanocluster growth is proportional to the sputtering voltage used and thus the sputtering ion energy. This could be supported by the known relationship between sputter voltage and sputtered atom flux whereby a higher sputtering voltage results in a higher sputtering rate and thus a higher sputtered atom flux. As a result, atoms would be deposited in quicker succession allowing for larger structures to be formed from both surface diffusion as well as nucleation from depositing atoms. The maximum found cluster size per sputtering voltage was not demonstrated to be linear however, with maximum values at 2 kV and 3 kV found to be similar whilst maximum nanocluster sizes at 4 kV was shown to be up to 3 times as large. This trend was more reflective of an exponential relationship between sputter voltage and maximum nanocluster size. Furthermore, the similar maxima at 2 kV and 3 kV suggested that below a certain value the change in sputter voltage has a minimal effect on nanocluster growth however, above a critical value, the sputter voltage could be said to quickly influence nanocluster size. Therefore reflecting an exponential relationship. It must be kept in mind however that the number of images taken for each sputtering voltage varied with 3 images at 2 kV, 1 image at 3 kV, and 15 images at 4 kV. To confirm this hypothesis and relationship, it would be beneficial to recreate these samples under a broader range of sputtering voltages and capture a similar quantity of images for analysis at each sputtering voltage.

At each sputter voltage, distinct Gaussian peaks could also be identified with, in some cases, hidden peaks also able to be seen. In Figure 6.7a, two distinct Gaussian peaks could be identified at *100-200 atoms* and *800-900 atoms*, as well as a subtle peak at *500-600 atoms*. The positions of these peaks approximately aligned with certain magic numbers as previously described, specifically at this sputtering voltage this includes sizes *147, 561, 923* [34–38]. Whilst no distinct peaks were noticeable at nanocluster sizes *13, 55, 309*, results do show the presence of nanoclusters within these size ranges. This suggests that 2kV sputtering voltage, specific nanocluster sizes are more favourable than others. In contrast, review of results displayed in Figure 6.7b demonstrated only two distinct Gaussian peaks. In this sample these were located at *10-100 atoms* and *300-400 atoms*. Once again these peak locations aligned with existing known magic numbers however, unlike the previous 2 kV sample these were located at sizes *13, 55, 309* for a 3 kV sputtering voltage [34–38]. Similarly, no distinct peaks could be found at sizes corresponding to *147,and 561*, however a presence of nanoclusters can be seen within these size ranges. This further suggests that certain nanocluster sizes are favourable depending on the sputtering voltage used and thus the sputtered atom flux. Lastly, in Figure 6.7c a number of distinct Gaussian peaks could be identified, and as with the increased nanocluster size, there were an increased number of peak locations. At 4 kV, distinct sputtering peaks could be seen at *100-200 atoms*, *500-600 atoms*, *900-1000 atoms*, *1500-1600 atoms*, and *2000-2500 atoms*. As before, these peak locations were shown to roughly correspond to previously found magic numbers for metastable Au nanoclusters. In the context of these results this includes; *147, 561, 923, 1415, 2057*, with increased deviation in larger cluster sizes [34–38]. Here the increased sputtered atom flux clearly demonstrates an increase in growth rate with nanoclusters demonstrated up top 3000 atoms. Once again specific metastable nanoclusters sizes have been demonstrated here with peaks not visible for sizes corresponding to *13, 55, and 309* atoms. This presence of select peaks, particularly in the smaller size range further support the idea that stabilisation of nanoclusters at specific sizes, could be sputtered atom flux dependent.

Across all sputtering voltages, the locations of Gaussian peaks were shown to vary however, these results demonstrated that specific peak locations were more common than others. For example, results showed how Gaussian peak locations at *147, 561, 923* atoms were only present in 2 kV and 4 kV samples whilst *13, 55, 309* atoms were only present in the 3 kV sample. With the only varying factor being the sputtering voltage and thus the sputtered atom flux, this further suggested that nanoclusters of certain sizes are favourable under certain sputtering voltages. As a result of this, further investigation may lead to show that high proportions nanoclusters can grow at specific sizes based on the tuning of the sputtering voltage in this method of nanocluster synthesis. Given the increased appearance of peaks at *147, 561, 923* atoms, further research using an increased sample size may also go on to show how certain metastable nanocluster sizes are more favourable than others. This could potentially lead to the ability to grow nanoclusters of specific sizes using this method corresponding to process conditions.

Cluster Structure Investigations

Once the correct atomic size of identified nanoclusters was calculated, the next step was to investigate the structure of each nanocluster. This was performed through two approaches; firstly, using their *Equivalent Circular Diameter (ECD)* derived from their area, and the volume of a single Gold atom as described in Section 5.1.2 and Equations (5.8) to (5.13). To understand the likely quasi-structure of analysed nanoclusters, atomic size vs equivalent circular diameter plots were created containing each nanocluster. In addition, these plots contained calculated trendlines for possible geometric structures allowing for identification of a nanoclusters likely quasi-structure as well as understanding of goodness of fit. The quasi-structure distributions for nanoclusters at each sputtering voltage are shown below in Figure 6.8. As it can be seen, the geometric shapes of identified nanoclusters greatly varied between numerous different three-dimensional as well as two-dimensional structures as discussed below.

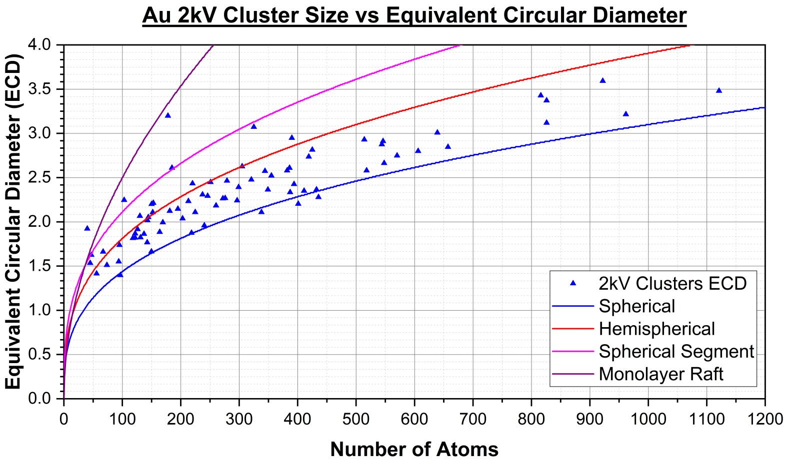

(a)

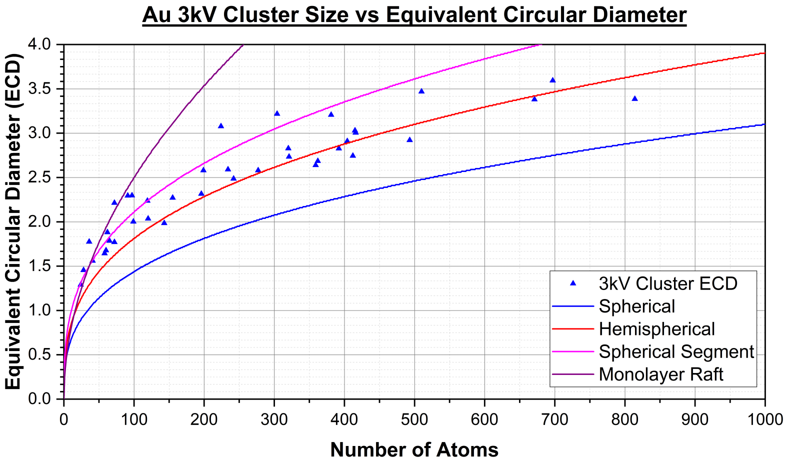

(b)

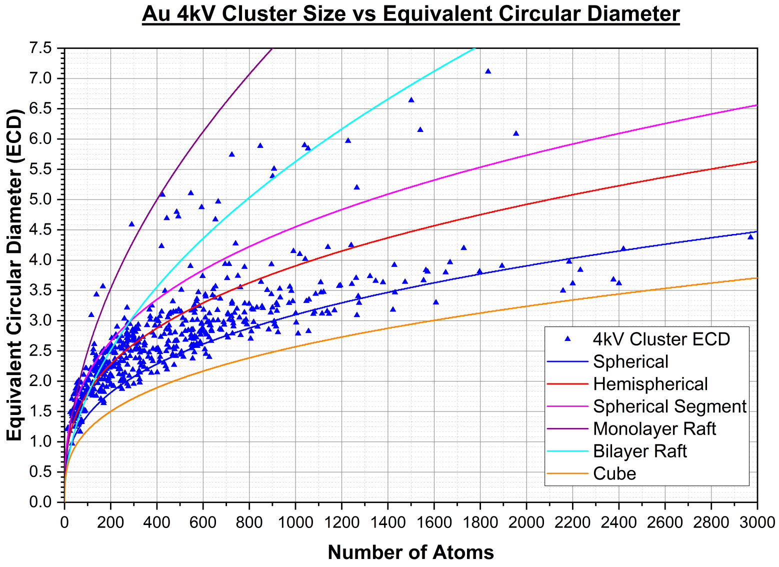

(c)

Figure 6.8: Au Cluster Size vs Equivalent Circular Diameter (ECD) plots for varied sputter voltages. a) Cluster Size vs ECD plot for sputtering at 2 kV, b) Cluster Size vs ECD plot for sputtering at 3 kV, c) Cluster Size vs ECD plot for sputtering at 4 kV.

3D Clusters

Analysis of nanocluster sizes vs equivalent-circular-diameters and comparison with known 3D geometric shape trends demonstrated a number of different viable 3D structures for grown nanoclusters. Predominantly these consisted of variations of spherical structures where the Vollmer-Weber growth mode would be preferred. In theory, metastable nanoclusters should settle as quasi-spherical structures however, as previously shown, a large proportion of analysed nanoclusters were found to be at non-magic number sizes suggesting some instability. Furthermore, as these nanoclusters were formed through surface aggregation and diffusion, interaction with the carbon substrate must also be taken into account [119]. As a result, structures resembling hemispheres and spherical segments were also found.

In Figure 6.8a, it could be seen that all three of these 3D structures were demonstrated however, the majority were shown to be between quasi-hemispherical and quasi-spherical in nature. Results showed that as nanoclusters grow in size they have a tendency to become more stable and hence reflect a quasi-spherical structure. This follows the previously described "Surface Area to Volume" ratio whereby as a nanoclusters size increases surface area to volume ratio decreases making it less affected by interaction with surfaces. The presence of a distribution between the hemispherical and spherical trendlines suggested however that there is some aspect of surface bonding occurring. This suggested that here nanocluster structures were a hybrid of a hemisphere and sphere. Below *350* atoms in size it could also be seen that there were a few nanoclusters which reflect a spherical segment structure where the base radius was larger than the nanocluster height. The presence of this structure suggested the occurrence of uneven growth and insufficient energy to initiate self-assembly. Through this method, nanocluster growth occurred through two approaches. Firstly, from the top by deposition of incoming atoms, and secondly from the side by surface diffusion. In order for spherical segment structured nanoclusters to occur, it suggested that the flux of surface diffused atoms was greater than that of depositing sputtered atoms specific to that deposition area. Such a difference in flux's seemed unlikely which may explain the rarity of these structures. However, another structure type found may offer some further insight into the formation of spherical segments, as will be detailed in the following section.

Unusually, Figure 6.8b demonstrated a lack of quasi-spherical structures despite having an increased sputtering voltage and thus sputter flux. Structures here were shown to be of a mix of spherical segment and quasi-hemispherical geometries. Once again however, a tendency towards a quasi-spherical nature was shown as the atom count in nanoclusters was increased. This reinforced the idea that the likelihood of metastable quasi-spherical structure formation increases with the size of grown nanoclusters. The anomaly of missing quasi-spherical structures still remained however. Unlike the *2 kV* samples, a slight increase in the presence of spherical segment structures was also shown here with an additional size presence increase up to *500* atoms. This delayed transition between structure types was indicative of increases in sputter voltages and hence sputter flux where, the increased atom presence generally increases the sizes for all structures. The majority of nanoclusters here however, were seen to be of the quasi-hemispherical nature with this appearing to be the stable geometric structure here. Unfortunately, the small sample size limits conclusive investigation and hence further investigation would be required to determine the reason for quasi-hemispherical stability at this sputtering voltage.

At the highest sputtering voltage, *4 kV*, a number of 3D geometries were demonstrated as seen in Figure 6.8c. Results showed the previously seen; spherical-segment, quasi-hemispherical, and quasi-spherical, as well as a new geometry, quasi-cuboidal, which was demonstrated at the larger sizes. Below *400* atoms in size, a great variation in structure was shown between the three spherical structure variants however, a strong proportion of nanoclusters in this region were shown to align with the spherical-segment and quasi-hemispherical geometries. Here this suggested that during the early stages of nanocluster growth the hemispherical structure was preferred. Above *400* atoms it was possible to notice the appearance of trends for each of these three structural motifs. Between the sizes of *400* and *800* atoms it could be seen that a small portion of nanoclusters to resemble the spherical-segment geometry however, no nanoclusters were seen above *800* atoms for this structure. At around the *700* atom mark it could also be seen that there was a possible trend for spherical-segment structures switching to quasi-hemispherical, once again suggesting a staged growth mechanism. Quasi-hemispherical structures could be observed up to a size of *1300* atoms both from transitioned nanoclusters and those that have remained quasi-hemispherical through out growth. Like the spherical-segment structure, a transition point from quasi-hemispherical to quasi-spherical could be seen however, this was seen at a much lower size of *800* to *900* atoms compared to the maximum size observed. The closeness to the transition point for spherical-segment to quasi-hemispherical suggested that this size region could possibly be a general structural transition size, particularly given the location of the metastable magic number of *923* atoms. Further investigation is however required.

Quasi-spherical structures were observable up to a size of *3000* atoms, once again from structural transitioned nanoclusters as well as those that have remained quasi-spherical from initial growth. Here the nanoclusters reflecting a quasi-spherical structure were shown to be quite imperfect with many nanoclusters being slightly distanced from the quasi-spherical trendline. This suggested a high degree of distortion as a result of an increased sputtering voltage of *4 kV* and hence increased flux, in comparison to lower sputtering voltages. This further suggested that the increased flux may be counter productive in terms of structural stability where imperfect geometries may reflect the inability to form a metastable structural isomer. Above *2000* atoms, a small trend was noticed where it appears another structural transition point was occurring towards a quasi-cuboidal geometry. This appeared highly unusual where stable grown nanoclusters are in most cases quasi-spherical. Further investigation here would be required however, if occurring, understanding the presence of a quasi-cuboidal nanocluster would be very interesting to analyse.

The increased presence of nanoclusters in the *4kV* sample also allows for the inference of a possible growth timeline for deposited single atoms to larger nanoclusters. As the data has shown, possible transition points can be seen whereby growing nanoclusters rearrange into different geometric structures. In the context of 3D structures this can be seen where as a nanoclusters size increases, structures transition from *Spherical-Segment* to *Hemispherical* to *Quasi-Spherical*. This provides an potential insight into the insitu growth of nanoclusters through this production method where early stages of growth reflect a Stranski-Krastanov growth mode before transitioning to a Vollmer-Weber growth mode. This can be supported by the discovery of 2D structures at smaller sizes, as will be described in the following section.

2D Rafts

In addition to the presence of multi-layered 3D nanoclusters, a small number of 2D nanoclusters were also discovered in the form of Monolayer and Bilayer Rafts. Distinguishable by their uniform HAADF intensity when compared with 3D nanoclusters where a more gaussian distributed intensity was seen across nanoclusters, as demonstrated below in Figure 6.9 and Figure 6.10. These structures represented an unexpected and interesting development in the understanding of nanocluster growth through surface diffusion. Demonstrated mostly in the sub-100 atom region, 2D rafts are an example of where surface diffusion of Au ad-atoms has occurred to form a small ‘sheet’ however, the Au-C binding energy is greater than the energy required for self-assembly thus retaining the raft like structure. The lack of energy to initiate self-assembly results in the loose structure formation as demonstrated in Figure 6.10a-c. Supporting analysis by Dr Thomas Slater has demonstrated a pair distribution function peak at approximately *2.5Å* which suggests the stability of these 2D structures can be attributed to surface interaction and lattice matching where the unit cell size is *2.46Å* for graphite [130–132]. Unlike the usual Voller-Weber growth mode of nanoclusters, the presence of these structures provide an example of early stage Stranski-Krastanov growth mode as demonstrated in Figure 2.4.

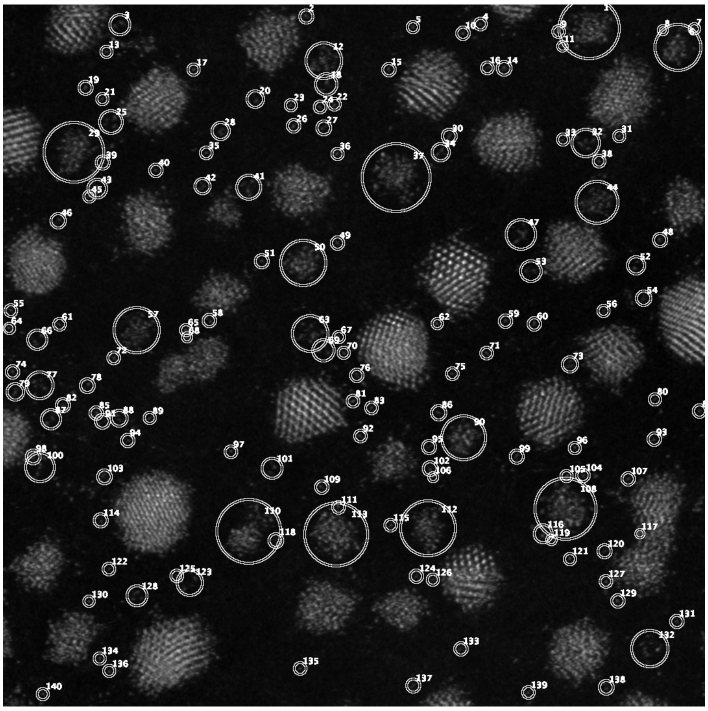

Figure 6.9: HAADF-STEM image identifying the presence of Au 2D structures made through sputtering onto an amorphous carbon support.

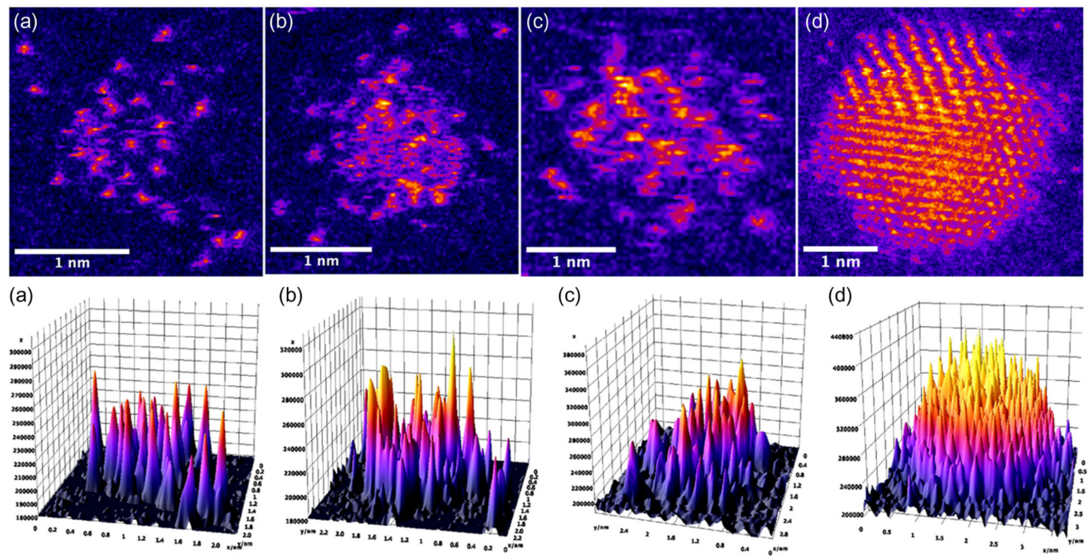

Figure 6.10: HAADF-STEM images and 3D surface plots of Au 2D and 3D structures made through sputtering onto an amorphous carbon support. a-c) 2D Rafts, d) 3D Cluster.

The contrast between raft like structures and that of 3D nanoclusters was somewhat realisable from direct observation of HAADF-STEM images where the similarity in HAADF intensities at single atom points distinguishes a similar height. However to best identify these structures, surface plots were often required to better confirm the uniform atomic height as shown in Figure 6.10a-d. As it could be seen raft structures were categorised by their majority uniform monolayer atomic height, where pixel intensities were similar to that of calibrated single atom intensities. This was in comparison to 3D nanoclusters where a clear multi-layer structure is demonstrated with highly varied pxiel intensities. The use of surface plots was a vital tool for distinguishing monolayer rafts from early 3D nanocluster structures. The finding of rafts in this growth mechanism also suggested a potential new growth timeline for certain nanoclusters. Earlier it was demonstrated that there was a small presence of 3D spherical segment clusters however, combined with the identification of 2D raft structures, a staged growth mechanism could be suggested. In this mechanism nanoclusters would begin as 2D rafts before transitioning to 3D spherical segments and then onto quasi-hemispherical and quasi-spherical structures. The evidence of this was somewhat visible in Figure 6.10b-c where existing monolayer rafts contained the beginnings of secondary and tertiary layer growth leading towards a spherical-segment structure. This suggested a majority Vollmer-Weber method of growth with stages of

Stranski-Krastanov growth in 2D raft to 3D cluster evolution [28]. DFT simulations by Dr Theodoros Pavloudis demonstrated evidence to support where data showed high competition between 2D and 3D structures below 100 atoms in size before the prevalence of 3D structures at larger sizes [132]. Whilst further investigation is needed, such a theory could lead to further understanding of surface aggregation nanocluster growth from a single atom to quasi-spherical nanoclusters.

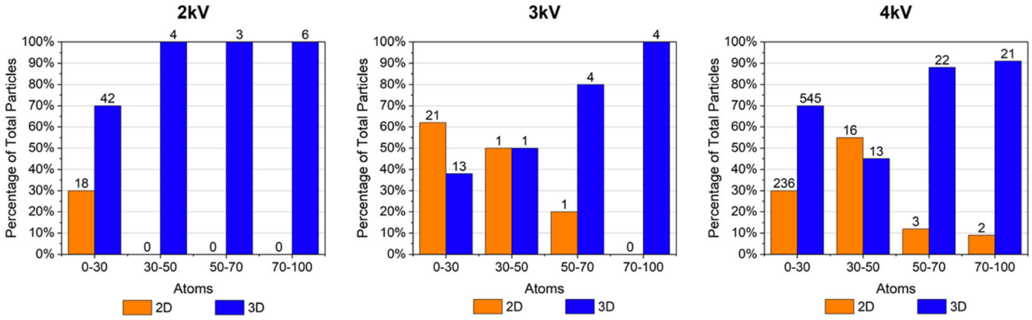

Figure 6.11: Plots of 2D vs 3D raft/nanocluster populations for three sputtering voltages in the 0-100 atom range.

Additional analysis of 2D vs 3D populations below 100 atoms in size across sputtering voltages further helped to understand the growth characteristics of the these 2D rafts. As shown in Figure 6.11, a size relationship was demonstrated between the sputtering voltage and maximum raft size. Like 3D nanoclusters, the maximum size of found 2D rafts was shown to be proportional to the sputter voltage used and therefore the sputtered atom flux. This could be explained in the same way that size increases in 3D nanoclusters where the increased flux of incoming atoms increased the growth rate, and single atom density and thus the maximum achievable size. In Figure 6.11 it could be seen that for *2 kV* and *3 kV*, a linear proportion difference was demonstrated whereby, the population of larger rafts decreased as size increased. Like in 3D nanoclusters, this can a reflection of the density of sputtered atoms per unit area. However, at *4 kV* a shifted single peak was demonstrated. Located between *30-50* atoms, this peak could suggest a metastability point for raft structures within this size range, much similar to the preference of specific metastable nanoclusters sizes in 3D analysis. It is worth noting that this peak was located just below the metastable spherical nanocluster magic number at 55 atoms, this suggested however that the surface interaction perhaps delays the 3D transition and self-assembly below 100 atoms and suggested in some cases raft structures may be preferred [132].

Cluster Isomer Distribution

Once quasi-structure of grown Au nanoclusters had been determined, the next stage was to identify the structural isomer of nanoclusters where possible. In this study, nanoclusters were visually compared with an existing simulation atlas and categorised as either Face-Centered-Cubic (FCC), Decahedral (Dh), Icosahedral (Ih), or Unidentified/Amorphous (U/A) where identification was not possible. From the results of this investigation, structural patterns could be established when combined with size investigation findings. The results of this analysis are described below.

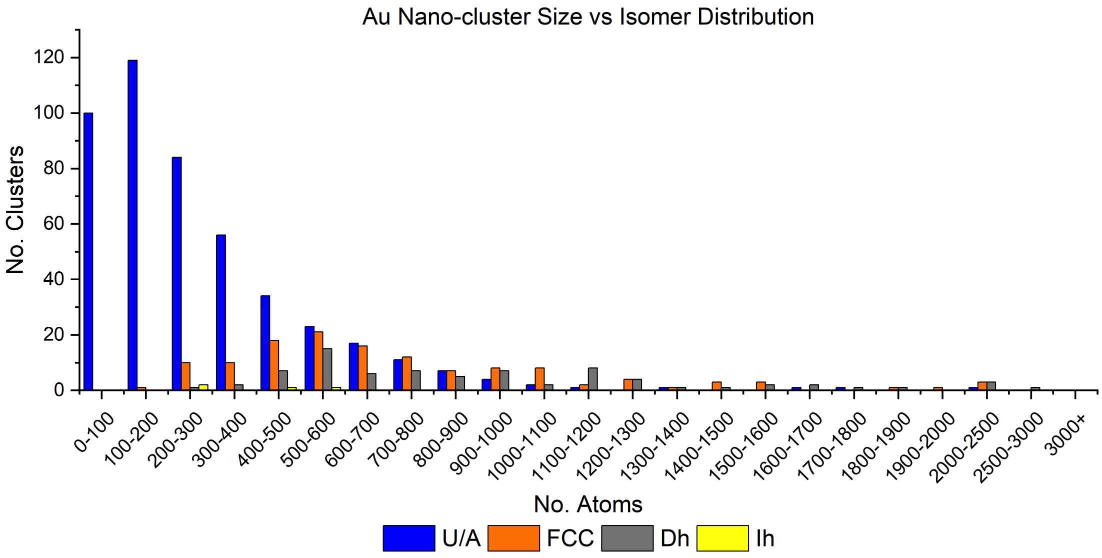

(a)

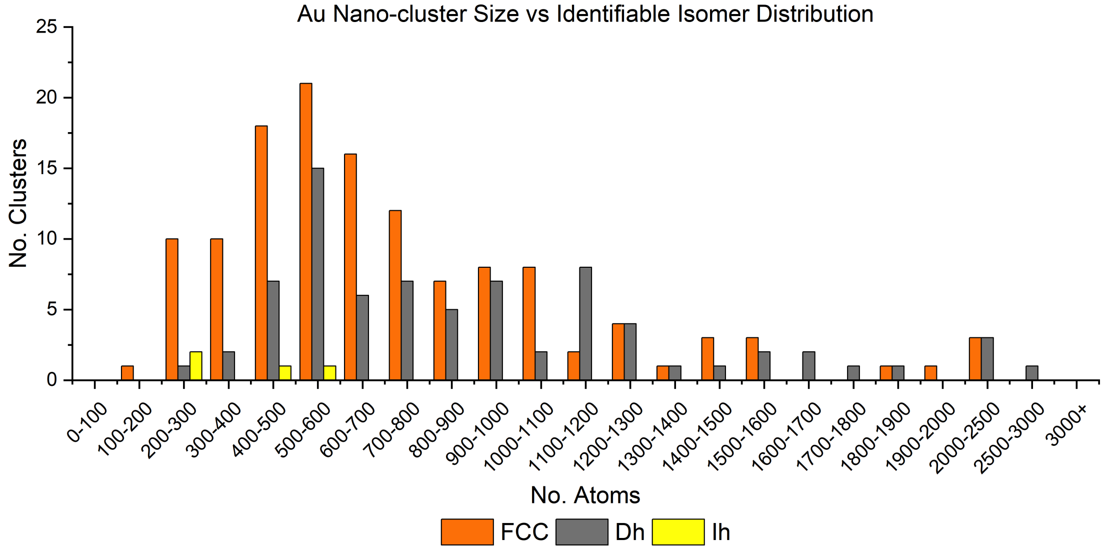

(b)

Figure 6.12: Plots of Au nanocluster size vs isomer distribution, a) including and b) excluding U/A nanoclusters.

As shown above in Figure 6.12, the settled isomer for nanoclusters was strongly dependent on the size of the nanocluster in question. Figure 6.12a demonstrated how below *200* atoms, nanoclusters were almost always amorphous in nature suggesting an element of surface interaction was taking place preventing self-assembly into a stable isomer. Between *200* and *1100* atoms however, the predominance of glassy structures gradually decreased and metastable isomeric nanoclusters began to appear indicating this may be the transition point where nanoclusters were able to overcome the surface binding energy and self-assemble. For Gold as shown in Figure 6.12b, the majority of these nanoclusters formed into either FCC or Dh nanostructures which have previously been shown to be very competitive in energies [123, 133]. However, a small number were shown exhibit an icosahedral structure at the sizes *200-300* and *400-600* atoms. This was particularly unusual where previous work by Mottet et al. has demonstrated the theoretical energy for icosahedral structures is at least *0.06 eV* higher than that of FCC and Dh isomers [123]. Such a presence was unusual and suggested a mechanism of instability perhaps caused by interaction with the carbon support. The most dominant isomers above *200* atoms however, were shown to be Dh and FCC which reflected previous works where the energy difference between these two isomers could be less than *0.04 eV* indicating a high degree of competition [123, 133]. In the *200-800* atom range the FCC isomer type was initially shown to be the more dominant of these two isomers. As the size of the nanoclusters increased however, the two isomers demonstrated greater competition with an equal distribution being shown reflecting theoretical and experimental works [123, 133]. Above *1600* atoms the decahedral isomer structure was shown to prevail as the more dominant with the presence of FCC structures becoming slightly rarer. This was in conflict with theoretical work where the bulk FCC structure should prevail as nanocluster size increased, being energetically favourable [123]. One possible explanation for this could be the assumed symmetrical nature of simulated nanoclusters in comparison to the often asymmetrical and imperfect nature of actual nanoclusters with the interaction between the nanocluster and the substrate to also consider.

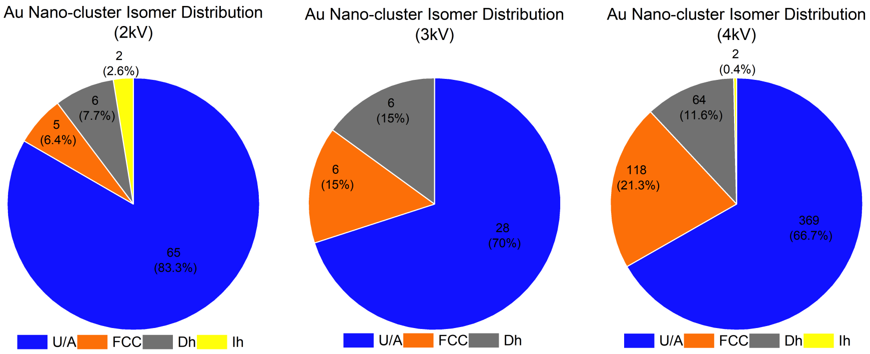

Figure 6.13: Plots of Au nanocluster isomer distributions per sputtering voltage as a percentage of the total population across all sizes.

The sputtering voltage employed was also shown to influence the popularity of different isomers as illustrated above in Figure 6.13. Worth noting, sputtered atoms do not retain any of their sputtered energy and hence a change in sputtering energy has no effect on the energy of the particle on deposition. Between these voltages the only change would be the particle flux, therefore it should be said that the particle flux was the contributing factor towards isomer popularity. At all sputtering voltages it could be seen that the unidentifiable/amorphous structure type was the most dominant due to the higher number of nanoclusters at lower sizes. Of the identifiable isomers however, some patterns could be identified between the particle flux and popularities. For example, it was noticed that the icosahedral isomer structure was only present at the *2 kV* and *4 kV* sputtering voltages however, the low number of identified icosahedral nanoclusters made it difficult establish a reliable pattern between particle flux and this isomer structure. A relationship between the Dh and FCC isomer structures however, could be seen. As previously mentioned, theoretical work has shown that energetically the Dh and FCC isomer structures are very competitive in the size range of these nanoclusters [123, 133]. This was reflected in Figure 6.13 at *2 kV* and *3 kV* sputtering voltages where nanocluster counts for these two isomers were shown to be very close, if not equal. At *4 kV* however, the FCC isomer structure was shown to be favourable over the Dh isomer structure where nanocluster counts for FCC were almost double that of Dh. This suggested a possible relationship between the dominance of certain isomers and the sputtered atom flux during deposition, aggregation, and nanocluster growth. The establishment of a relationship here through further controlled study across similar size ranges, would potentially allow for the synthesis of isomer tuned Au nanoclusters which could be expanded to included additional metals.

6.2 Summary

Gold (Au) nanoclusters from three samples using 2 kV, 3 kV, and 4 kV sputtering voltages were imaged at various magnifications and analysed using the concentric ring method, as previously described in Section 5.1.1, to determine their atomic size. Results overall demonstrated a wide range of nanocluster sizes varying from *1* to *3000* atoms with the majority found to below *1000* atoms. At the *2 kV* sputtering voltage, nanocluster sizes were seen up to *1200* atoms with the majority found below *600* atoms. Here an initial peak was seen in the *100-200* atom size range followed by smaller peaks at *500-600* and *800-900* atoms, which roughly aligned with the *141*, *561*, and *923* atom metastable magic numbers. A similar size range could be seen in the *3 kV* sample where nanoclusters were found up to *900* atoms however, the peak locations here were quite different. In the *3 kV* sample, peaks were identifiable only at the *10-100* and *300-400* size ranges. These did however still correspond to known metastable magic numbers at *13*, *55*, and *309* indicating the presence of metastable nanoclusters. In contrast, the *4 kV* sample demonstrated a size range roughly triple that of the lower sputtering voltages with sizes up to *3000* atoms being seen. Here a number of Gaussian peaks were demonstrated across the entire size range. These were seen at the *100-200*, *500-600*, *900-1000*, *1500-1600*, and *2000-2500* size ranges, which aligned with the metastable magic numbers *141*, *561*, *923*, *1415*, and *2057*. As seen before, sputtered atom flux was shown to contribute heavily here to the size of grown nanoclusters with the *4 kV* sample demonstrating the highest sample range. Grown nanoclusters were also seen to illustrate some degree of metastability in growth with the presence of numerous Gaussian peaks often centred around known metastable nanocluster sizes.

Further processing of measured data also allowed for the estimation of nanocluster structure geometries through comparison with calculated structure trendlines. Analysis indicated multiple 3D geometries as well as the unexpected presence of 2D raft like structures. Nanoclusters demonstrating a 3D structure were shown to take either a quasi-spherical, quasi-hemispherical, spherical segment, or quasi-cuboidal geometry with examples being found across all size ranges. 2D nanostructures known as “Rafts” however, were only found at smaller sizes with the majority discovered below *100* atoms in size. Quasi-structure analysis was conducted for each sputtering voltage and results were compared to determine any patterns. At *2 kV*, results showed the majority of nanoclusters exhibited a quasi-hemispherical to quasi-spherical geometric structure with a trend towards quasi-spherical as nanocluster size increased. Here only a few 2D structures were identified in comparison to 3D structures. In comparison, at *3 kV*, 3D structures were found to be of the spherical segment geometry transitioning to quasi-hemispherical as particle size increased. Interestingly no quasi-spherical structures were observed here. As in the *2 kV* sample, a small population of 2D raft structures were observed at this sputtering voltage with a slightly higher population that those found at the lower sputtering voltage. This increased presence of 2D structures aligned with the expected increase in nanostructure count due to the increase sputtered atom flux. Unfortunately however, the limited sample size here limited the establishment of solid patterns. The *4 kV* sample however benefited from a large sample size allowing for clear patterns to be seen. Here a more diverse variety of geometries have been observed. At this sputtering energy, the previously observed 3D geometries were seen as well as a new, quasi-cuboidal, geometry illustrated at sizes above *2000* atoms. Furthermore, transition zones were also noticed between different 3D geometries where results suggested a 3D staged growth through; spherical segment to quasi-hemispherical to quasi-spherical. As before an increased number of 2D structures were also observed at this sputtering voltage corresponding to the increased sputtered atom flux. Once again the majority of these structures were found below 100 atoms however, a rare few were seen at larger sizes. Nanocluster growth trends were also more distinguishable at this sputtering voltage where the presence of 2D structures and a larger sample size hinted at a pattern for nanocluster growth where structures begin as 2D rafts at lower sizes before transitioning to 3D structures in stages as previously mentioned.

Additional structure investigations were also carried out through visual inspection of Au nanoclusters to further determine the isomer structures of produced nanoclusters. Results from comparison with an existing simulation atlas showed a dominance of two identifiable isomers; decahedral and face-centered-cubic, with close competition demonstrated between both. Initially nanoclusters were shown to be mostly glassy and unidentifiable however, above 200 atoms, structures become identifiable with the FCC isomer being primarily dominant. Dh was seen to have a delayed presence in comparison to FCC however, from 800-1600 atoms the Dh and FCC isomers were shown to be highly competitive. This was found to be in line with previous theoretical work where an energy difference of *0.04 eV* was calculated [123, 133]. A rare appearance of icosahedral structures were also shown in this size range. Above 1600 atoms however, Dh was shown to prevail as the more dominant isomer structure which was in disagreement with theory, suggesting additional factors such as surface interaction were causing decahedral stability. Comparison between sputtering voltages also demonstrated a potential relationship between isomer popularity and general metastability. It was found that as the sputter voltage increased, the proportion of identifiable isomers to unidentifiable structures increased, suggesting that a higher flux was required for the formation of stable isomers. Furthermore, at the *4 kV* sputtering voltage a difference in ratio between the FCC and Dh isomers was shown where FCC was seen to be favourable. This is in comparison to the *2 kV* and *3 kV* sputter voltage samples where an equal distribution is demonstrated between both isomers. This could suggest a potential relationship between the dominance of structural isomers and the sputtered atom flux used.

Analysis of nanoclusters synthesised from two different methods has demonstrated numerous results and trends in both size and structure. For both Ag and Au nanoclusters potential relationships have been identified between synthesis conditions and end sizes and structures. Such findings open the possibility for further research through a number of different avenues specific to the characteristic being investigated. Such continuation however, could be fruitful in determining the potential for both size and geometric/isomer tuned nanoclusters which may in turn prove useful in applications like catalysis and nanoelectronics.

Chapter 7

CONCLUSION AND FUTURE WORK

Overview

This chapter will look to summarise an conclude the work presented in this thesis. This will include the synthesis of Carbon Nanotubes in addition to Silver and Gold nanoclusters, as well as the analysis performed through both TEM and STEM imaging, and post-processing using image processing software. Furthermore, potential future work will be explored in the context of results achieved in nanocluster investigations.

7.1 Conclusion

The production and understanding of both current and new nanostructures is vital to continued development in technological and industrial applications. The wide-variety of structural and compositional combinations offer opportunity's to apply tailored improvements to new and existing systems, on the nanoscale. In this thesis, the objective was to build a strong knowledge on a selection of PVD synthesis and analysis techniques for nanostructures, focussing on nanoclusters. Though which a positive contribution to the field could be made. Here, the regeneration of an existing cluster source has been detailed as a promising platform for future work, carbon nanotubes and metal nanoclusters have been investigated using Transmission Electron Microscopy and image processing techniques, to understand the relationships between synthesis methods and resulting sizes and structures. In particular, carbon nanotubes synthesised through catalytic chemical vapour deposition, and nanoclusters produced through matrix assembly as well as surface aggregation, were analysed in this thesis.

In chapter 3, the regeneration of a Caesium Sputtering Negative Ion Cluster Source was detailed whereby, thermally ionised Caesium is used to sputter a negatively charged target producing a beam of negatively charged ions and small clusters. A breakdown of the cluster source was given where the operation of the system could be described in stages. As part of the regeneration, two aspects of digitisation of the source were undertaken including; the production of a CAD model to aid in the restoration of the system and provide a basis for future upgrades. Furthermore, a SIMION model of the source and ion optics stages was created to allow for simulated responses of Einzel lens biases to be visualised. In these aspects of digitisation, efficiency in regeneration and operation of the cluster source was greatly improved and, provided a visual understanding of how the clusters system operates. This in turn led to the design and installation of an upgraded load lock stage through CAD modelling. The new load lock greatly improved the operational efficiency of the system and opened the cluster source to the possibility of use with a larger range of samples. Performance evaluation of the regenerated cluster source through the use of mass and clusters spectrums taken at two points within the system. Results showed the successful production of Silver nano clusters up to to 3 atoms in size, where the primary signal was found for single atoms. Structures containing 2 and 3 atoms were shown to have oxidised indicating partial oxygen contamination in the system. In addition, smaller carbon cluster were also demonstrated on numerous occasions, once again as a product of contamination within the system. Comparisons with previous work demonstrated similar results indicating the successful operation of the clusters source however, indicating further work is necessary to bring the system back to it previous operational level.

In chapter 4, Multi-walled carbon nanotubes were grown by Ali Hedayati and Jainabi Sallah-Conteh through the use of a Catalytic Chemical Vapour Deposition (CCVD) method in a two-zoned horizontal liquid injection reactor (LIR). In this method, a Ferrocene and Polystyrene infused Anhydrous Toluene solution was used to grow the carbon nanotubes where the Polystyrene concentration was varied. Grown cabron nanotubes were then imaged under HRTEM and investigations were undertaken to review both the surface and core structures. In surface investigations, multiple trends were discovered linking the concentration of Polystyrene to the uniformity of the carbon nanotube lengths and diameters. Analysis showed that with an increase in Polystyrene dosage, came an increase in length uniformity across analysed carbon nanotubes. However, for carbon nanotube diameters this was only seen up to a critical concentration where-after diameter uniformity would decrease. Relationship between lengths and diameters was also shown to become more linear with increasing Polystyrene dosage, again up until a critical concentration. Furthermore, visual inspection of carbon nanotubes dosed with 4 wt% Polystyrene were seen to consist of an amorphous carbon shell suggesting this could be related to the high dosage of Polystyrene. Core structure investigations showed that Polystyrene concentrations were independent of the number of walls in carbon nanotubes. Furthermore, wall count ranges were not seen to correlate with changing carbon nanotube diameters where this was accounted for in differing central core sizes corresponding to catalyst particle size. FFT investigations confirmed however, that the interlayer spacings matched that of stacked graphene sheets as expected. Overall, work presented here successfully demonstrated the recycling of polystyrene into the production of carbon nanotubes.

In chapters 5 and 6, Ag nanoclusters produced by Erica Watchorn-Rokutan using a Matrix-Assembly method and Au nanoclusters produced by Dr James McCormack using a thermal evaporation and ion sputtering method, were imaged under AC-

STEM by Dr Thomas Slater and analysed using image processing software. Here a concentric-ring method was used to analyse single atoms and nanoclusters to determine their atomic size in addition to visual inspection to ascertain their isomeric structure. In Ag nanoclusters investigations, a low-coverage and high-coverage sample was analysed. Results showed that the maximum achievable size of nanoclusters was highly dependent on the sputtered particle flux and deposition time where sizes in the low-coverage sample were limited to 800 atoms compared to 6000 atoms in the high-coverage sample. In both samples it was seen that the major peaks occurred at lower sizes, sub-100 atoms and 100-200 atom for low-coverage and high-coverage samples respectively. Numerous minor peaks were seen however, very few were located at corresponding magic number locations. This suggested that nanoclusters at non-magic number locations had found stability through other means. Due to the high oxidising nature of Ag, it was thought that the presence of Oxygen and Sulphur from atmospheric contamination provided such stability. Further structural investigation also uncovered some interesting results where the Icosahedral isomer structure was unexpectedly found to be preferred across all sizes, and particularly at larger sizes. Decahedral and Cuboctahedral isomer structures were found to be highly competitive however, these structures were only found below 500 atoms in size. Once again, the dominance of the Icosahedra structure was thought to be a result of Oxygen and Sulphur contamination where otherwise Decahedra and Cuboctahedra should be seen as dominant. Investigations also demonstrated the relationship of sputtered particle flux to the populations of identifiable isomers where it was seen that a higher flux yielded a higher number of structurally identifiable nanoclusters. Furthermore, a higher concentration of Decahedra and Cuboctahedra were seen in the higher flux sample, suggesting these isomer structures prefer a higher deposition rate.

Investigation of Au nanoclusters at 2 kV, 3 kV, and 4 kV sputtering voltages were undertaken to analyse their size, isomeric structure, as well as quasi-geometries. Size investigations revealed an overall size range of 1-3000 atoms however, maximum size ranges were seen to be a function of the sputtering voltage used where a higher flux generally yielded a larger size range. Analysis showed sizes up to 1200 atoms for 2 kV, 900 atoms for 3 kV, whilst at 4 kV the maximum size quickly increased to 3000 atoms. Throughout all samples, sizing peaks were noticed surrounding metastable magic numbers however, not all occurrences were common to all samples. At 2 kV, peaks could be found corresponding to the *141, 561,* and *923*, whilst at 3 kV peaks were only identifiable at lower sizes of *13, 55,* and *309.* In contrast, at 4 kV many peaks were noticed across the size range corresponding to magic numbers from *141* to *2057*, excluding *309.* Continued investigation of structural isomers also unveiled interesting results. Overall the Decahedral and Cuboctahedral structures were seen to be dominant with Icosahedra making an occasional appearance. These two isomers were also seen to be highly competitive in mid-range sizes (800-1600 atoms). Below 800 atoms, Cuboctahedra were seen to be highly preferred with Decahedra becoming more prominent above 400 atoms. In comparison, above 1600 atoms, Decahedra were seen to be the preferred structural isomer with Cuboctahedra only making the occasional appearance. Additional investigation also revealed a potential relationship between the dominance of isomers and the employed sputtering voltage. Here, initial investigations showed how the popularity of Cuboctahedra increased at 4 kV, whilst remaining competitive at 2 kV and 3 kV. For Au nanoclusters, additional analysis was also performed on the quasi-geometries of grown nanoclusters where it was discovered that both 3D and 2D nanoclusters were present. 3D geometries were found to consist of: spherical segment, quasi-hemispherical, and quasi-spherical geometries. Further analysis of these geometries in comparison to the nanocluster size suggests a potential staged-growth mechanism where nanoclusters transition from spherical segments to quasi-hemispherical to quasi-spherical structrues as they grow. Furthermore, the presence of 2D structures were discovered at smaller sizes, specifically below 100 atoms. These structures exhibited a loosely bonded monolayer structure and were hence termed *'2D Rafts'*, and presented an interesting new development in the analysis of surface assembled nanoclusters. Like 3D nanoclusters, the maximum size of grown 2D rafts were shown to be influenced by the sputtering voltage and thus the flux where a higher flux yielded large rafts.

The synthesis conditions vs end size and structure studies presented in this thesis provided a variety contributions into the growth mechanisms of two different nanostructures and their dependences on their synthesis conditions. This has improved the existing understanding of theses nanostructures as well as new nanostructures such as the 2D rafts, providing numerous avenues for further research into the production of specific and tuned nanomaterials and structures. Furthermore, the recommissioning of a Caesium Sputtering Negative Ion Cluster Source has provided a basis for which the work presented here can continue, focussing on smaller nanoclusters.

7.2 Future Work

Investigations performed in this thesis have unveiled numerous trends in the sizes and structures of carbon nanotubes and nanoclusters, many of which offer exciting prospects for further investigation. In particular is the topic of nanoclusters where the work demonstrated has outlined many avenues for future work, as will be detailed here.

7.2.1 AC-STEM Imaging of Nanoclusters

The examination of nanoclusters performed in this thesis has revealed a variety of different patterns and relationships between synthesis conditions and end produced nanoclusters. In the end produced nanoclusters with different variations in sizes and structure could lead to a number of different characteristics and in turn lead to various potential applications. The investigation into Ag nanoclusters produced through Matrix assembly and Ion beam sputtering, yielded a number of differences in results depending on synthesis conditions. Here Ion beam sputtering was conducted at a low power and sputtering time for the low coverage sample, and a high power and sputtering time for the high coverage sample. This led to differing nanocluster size ranges between samples, as a function of two variables. To better understand the effects of both sputtering power and time, future could be conducted to include low-power and large sputtering time, as well as high-power and low sputtering time. From here, a better understanding could then be achieved into exactly how this synthesis method works to produce certain variations of nanoclusters. In addition, in this study it was also determined that the contamination of nanoclusters with air, specifically Oxygen and Sulphur, led to the stabilisation of Ag nanoclusters at unexpected sizes and the high population of the Icosahedral isomer structure. To better confirm this, a controlled study could be undertaken to compare the effects of Ag nanoclusters produced using the Matrix assembly method when exposed to air and when protected from air. Furthermore, Oxygen and Sulphur contamination could be initially confirmed through the use of STEM-EDS analysis and elemental mapping to confirm if the grown nanoclusters do in fact possess Oxygen and Sulphur shells.

Work on the analysis of Au nanoclusters also revealed a number of potential trends between synthesis conditions and resulting nanoclusters. Investigations performed in this work showed a potential pattern between sputtering voltage and grown nanocluster size maxima. This however, could not be confirmed in this work due to limited data for nanoclusters at the 2 kV and 3 kV sputtering voltages in comparison to the 4 kV sputtering voltage. To confirm this, further imaging of these specific samples should be carried out to better support these findings. In addition to this, the sample range could be increased to see if a strong pattern can be established, i.e. use of higher and/or lower sputtering voltages. Another pattern seen as a function of the sputtering voltage was the popularities of specific isomers. Once again, expansion of existing data as well production of samples higher and lower sputtering voltages could provide further insight into the dependence of isomer formation on the sputtered particle flux. In this study, an initial pattern could also be seen in the growth methods of nanoclusters via surface aggregation. Here it was noticed that certain 3D structures transitioned at certain nanocluster sizes. Further study in this through the use STEM could lead valuable new discoveries into the exact mechanisms of surface aggregation growth. Such continued studies could lead to further understanding of nanocluster growth and the production of size and structure specific clusters from this method. Additionally, in this study, the presence of a new 2D structure was also realised *‘2D Rafts’*. This previously unnoticed structure was thought to be attributed to the lack of energy required detach from the substrate and initiate self-assembly. To fully understand this, more detailed investigation is required with a larger sample size which could be achieved with continued research. Further research such as this could provide more detailed insight into the exact dynamics of surface aggregation and self-assembly of nanoclusters. This can be beneficial in terms of both scientific knowledge as well the potential applications of these 2D structures.

Bibliography

[1] Shiza Malik, Khalid Muhammad, and Yasir Waheed. Nanotechnology: A Revolution in Modern Industry. *Molecules*, 28(2):661, jan 2023. ISSN 1420-3049. doi: 10.3390/molecules28020661. URL `https://www.mdpi.com/1420-3049/28/2/661`.

[2] National Nanotechnology Initiative. Applications of Nanotechnology. URL `https://www.nano.gov/about-nanotechnology/applications-nanotechnology`.

[3] Ibtisam Abbasi. The Role of Nanotechnology in Modern Industry, 2024. URL `https://www.azonano.com/article.aspx?ArticleID=6820`.

[4] IBM. Nanotechnology, 2024. URL `https://www.ibm.com/history/nanotechnology`.

[5] Günter Schmid, Monika Bäumle, Marcus Geerkens, Ingo Heim, Christoph Osemann, and Thomas Sawitowski. Current and future applications of nanoclusters. *Chemical Society Reviews*, 28(3):179–185, 1999. ISSN 03060012. doi: 10.1039/a801153b. URL `https://xlink.rsc.org/?DOI=a801153b`.

[6] The Editors of Encyclopaedia Britannica. Moore's Law, 2024.

[7] Mustafa Badaroglu. More Moore. In *2021 IEEE International Roadmap for Devices and Systems Outbriefs*, pages 01–38. IEEE, nov 2021. ISBN 978-1-6654-8638-5. doi: 10.1109/IRDS54852.2021.00010. URL `https://ieeexplore.ieee.org/document/9827527/`.

[8] Richard E. Palmer. Welcome to Clusterworld. *New Scientist*, 1997. ISSN 02624079.

[9] Hyungjun Park, Dong Jun Shin, and Junhua Yu. Categorization of Quantum Dots, Clusters, Nanoclusters, and Nanodots. *Journal of Chemical Education*, 98 (3):703–709, mar 2021. ISSN 0021-9584. doi: 10.1021/acs.jchemed.0c01403. URL `https://pubs.acs.org/doi/10.1021/acs.jchemed.0c01403`.

[10] Muhammad Ovais, Abida Raza, Shagufta Naz, Nazar Ul Islam, Ali Talha Khalil, Shaukat Ali, Muhammad Adeeb Khan, and Zabta Khan Shinwari. Current state and prospects of the phytosynthesized colloidal gold nanoparticles and their applications in cancer theranostics. *Applied Microbiology and Biotechnology*, 101(9):3551–3565, may 2017. ISSN 0175-7598. doi: 10.1007/s00253-017-8250-4.

[11] D. Depla, S. Mahieu, and J.E. Greene. Sputter Deposition Processes. In *Handbook of Deposition Technologies for Films and Coatings*, pages 253–296. Elsevier, 2010. doi: 10.1016/B978-0-8155-2031-3.00005-3. URL `https://linkinghub.elsevier.com/retrieve/pii/B9780815520313000053`.

[12] Angstrom Engineering. Ion Beam Sputter Deposition, . URL `https://angstromengineering.com/tech/ion-beam-processing/ion-beam-sputter-deposition/`.

[13] Oxford Instruments. Ion Beam Deposition. URL `https://plasma.oxinst.com/technology/ion-beam-deposition`.

[14] Humaira Ghazal and Nadeem Sohail. Sputtering Deposition. In *Thin Films - Deposition Methods and Applications*. IntechOpen, mar 2023. doi: 10.5772/intechopen.107353. URL `https://www.intechopen.com/chapters/84564`.

[15] Nature Portfolio. Plasma Physics. URL `https://www.nature.com/subjects/plasma-physics`.

[16] Norm (Semicore Equipment Inc) Hardy. What is Thin Film Deposition By Thermal Evaporation?, 2013. URL `http://www.semicore.com/news/71-thin-film-deposition-thermal-evaporation`.

[17] Almas Bashir, Tahir Iqbal Awan, Aqsa Tehseen, Muhammad Bilal Tahir, and Mohsin Ijaz. Interfaces and surfaces. In *Chemistry of Nanomaterials*, pages 51–87. Elsevier, 2020. doi: 10.1016/B978-0-12-818908-5.00003-2. URL `https://linkinghub.elsevier.com/retrieve/pii/B9780128189085000032`.

[18] Moorfield. Thermal Evaporation, 2018. URL `https://www.moorfield.co.uk/knowledge-base/thermal-evaporation/`.

[19] Angstrom Engineering. THERMAL EVAPORATION: OVERVIEW, . URL `https://angstromengineering.com/tech/resistive-thermal-evaporation/`.

[20] Richard E. Palmer, Rongsheng Cai, and Jerome Vernieres. Synthesis without Solvents: The Cluster (Nanoparticle) Beam Route to Catalysts and Sensors.

Accounts of Chemical Research, 51(9):2296–2304, sep 2018. ISSN 15204898. doi: 10.1021/acs.accounts.8b00287.

[21] Rongsheng Cai, Nan Jian, Shane Murphy, Karl Bauer, and Richard E. Palmer. A new method to prepare colloids of size-controlled clusters from a matrix assembly cluster source. *APL Materials*, 5(5), may 2017. ISSN 2166532X. doi: 10.1063/1.4977204.

[22] R. E. Palmer, L. Cao, and F. Yin. Note: Proof of principle of a new type of cluster beam source with potential for scale-up, apr 2016. ISSN 10897623.

[23] Wolfgang Harbich. Collision of Clusters with Surfaces: Deposition, Surface Modification and Scattering. pages 107–150. 2000. doi: 10.1007/978-3-642-57169-5_4. URL `http://link.springer.com/10.1007/978-3-642-57169-5_4`.

[24] J.D. Pelletier, M.H. Shapiro, and T.A. Tombrello. Molecular dynamics simulations of low-energy cluster deposition on metallic targets. *Nuclear Instruments and Methods in Physics Research Section B: Beam Interactions with Materials and Atoms*, 67(1-4):296–300, apr 1992. ISSN 0168583X. doi: 10.1016/0168-583X(92)95820-H. URL `https://linkinghub.elsevier.com/retrieve/pii/0168583X9295820H`.

[25] Vladimir N. Popok, Ingo Barke, Eleanor E.B. Campbell, and Karl-Heinz Meiwes-Broer. Cluster–surface interaction: From soft landing to implantation. *Surface Science Reports*, 66(10):347–377, oct 2011. ISSN 01675729. doi: 10.1016/j.surfrep.2011.05.002. URL `https://linkinghub.elsevier.com/retrieve/pii/S0167572911000318`.

[26] Daniel Mangfält. *Fundamental processes in thin film growth: The origin of compressive stress and the dynamics of the early growth stages*. Linköping University Electronic Press, apr 2014. ISBN 9789175193526. doi: 10.3384/diss.diva-105791. URL `http://urn.kb.se/resolve?urn=urn:nbn:se:liu:diva-105791`.

[27] Karl-Heinz Meiwes-Broer. *Metal Clusters at Surfaces*. Springer Series in Cluster Physics. Springer Berlin Heidelberg, Berlin, Heidelberg, 2000. ISBN 978-3-642-63064-4. doi: 10.1007/978-3-642-57169-5.

[28] K. Oura, M. Katayama, A. V. Zotov, V. G. Lifshits, and A. A. Saranin. Growth of thin films, 2003.

[29] W. D. Knight, Keith Clemenger, Walt A. de Heer, Winston A. Saunders, M. Y. Chou, and Marvin L. Cohen. Electronic Shell Structure and Abundances of Sodium Clusters. *Physical Review Letters*, 52(24):2141–2143, jun 1984. ISSN 0031-9007. doi: 10.1103/PhysRevLett.52.2141. URL `https://link.aps.org/doi/10.1103/PhysRevLett.52.2141`.

[30] Gabriel F. S. Fernandes, Francisco B. C. Machado, and Luiz F. A. Ferrão. Identification of Magic Numbers in Homonuclear Clusters: The ε 3 Stability Ranking Function. *The Journal of Physical Chemistry A*, 124(2):454–463, jan 2020. ISSN 1089-5639. doi: 10.1021/acs.jpca.9b11264. URL `https://pubs.acs.org/doi/10.1021/acs.jpca.9b11264`.

[31] Puru Jena and Qiang Sun. Super Atomic Clusters: Design Rules and Potential for Building Blocks of Materials. *Chemical Reviews*, 118(11):5755–5870, jun 2018. ISSN 0009-2665. doi: 10.1021/acs.chemrev.7b00524. URL `https://pubs.acs.org/doi/10.1021/acs.chemrev.7b00524`.

[32] Alexander Belyaev and Douglas Ross. The Nuclear Shell Model. In *The Basics of Nuclear and Particle Physics*, chapter 5, pages 53–66. Springer Cham, 1 edition, 2021. doi: 10.1007/978-3-030-80116-8_4. URL `https://link.springer.com/10.1007/978-3-030-80116-8_4`.

[33] R Nave. Shell Model of Nucleus. URL `http://hyperphysics.phy-astr.gsu.edu/hbase/Nuclear/shell.html`.

[34] J. A. Barker. Microcluster II: The Geometries of Soft-Sphere Packings. *Le Journal de Physique Colloques*, 38(C2):C2–37–C2–45, jul 1977. ISSN 0449-1947. doi: 10.1051/jphyscol:1977208. URL `http://www.edpsciences.org/10.1051/jphyscol:1977208`.

[35] G.S. Anagnostatos. Magic numbers in small clusters of rare-gas and alkali atoms. *Physics Letters A*, 124(1-2):85–89, sep 1987. ISSN 03759601. doi: 10.1016/0375-9601(87)90378-1. URL `https://linkinghub.elsevier.com/retrieve/pii/0375960187903781`.

[36] Introduction to Nanoparticles and Nanostructures, 2018. URL `https://nanohub.org/resources/22260/download/NACK_U3_Maeder_Nanoparticles_Nanostructures.pdf`.

[37] Mathieu Leocmach and Hajime Tanaka. Roles of icosahedral and crystal-like order in the hard spheres glass transition. *Nature Communications*, 3(1):974, jul 2012. ISSN 2041-1723. doi: 10.1038/ncomms1974. URL `https://www.nature.com/articles/ncomms1974`.

[38] An Pang Tsai. Icosahedral clusters, icosaheral order and stability of quasicrystals—a view of metallurgy. *Science and Technology of Advanced Materials*, 9(1):013008, jan 2008. ISSN 1468-6996. doi: 10.1088/1468-6996/9/1/013008. URL `https://www.tandfonline.com/doi/full/10.1088/1468-6996/9/1/013008`.

[39] John Kitchin. Building atomic clusters in ase, 2014. URL `https://kitchingroup.cheme.cmu.edu/blog/2014/12/22/Building-atomic-clusters-in-ase/`.

[40] Francesca Baletto and Riccardo Ferrando. Structural properties of nanoclusters: Energetic, thermodynamic, and kinetic effects. *Reviews of Modern Physics*, 77 (1):371–423, may 2005. ISSN 0034-6861. doi: 10.1103/RevModPhys.77.371. URL `https://link.aps.org/doi/10.1103/RevModPhys.77.371`.

[41] Lu Cao. *Deposition of Size-Selected Nanoclusters*. PhD thesis, University of Birmingham, 2015.

[42] Libretexts. Closest packed structures, Jan 2023. URL `https://chem.libretexts.org/Bookshelves/Physical_and_Theoretical_Chemistry_Textbook_Maps/Supplemental_Modules_(Physical_and_Theoretical_Chemistry)/Physical_Properties_of_Matter/States_of_Matter/Properties_of_Solids/Crystal_Lattice/Closest_Pack_Structures`.

[43] L. J. de Jongh. Metal-cluster compounds: Model systems for nanosized metal particles. *Applied Organometallic Chemistry*, 12(6):393–399, jun 1998. ISSN 0268-2605. doi: 10.1002/(SICI)1099-0739(199806)12:6⟨393::AID-AOC744⟩3.0.CO;2-W. URL `https://onlinelibrary.wiley.com/doi/10.1002/(SICI)1099-0739(199806)12:6%3C393::AID-AOC744%3E3.0.CO;2-W`.

[44] Ana Proykova. *Modelling of Nanoclusters at Finite Temperatures*, pages pp.113–140. 12 2006. ISBN (ISBN-13: 978-954-580-265-2).

[45] Sagar Aryal. Electron Microscope: Principle, Types, Uses, Labeled Diagram, 2024. URL `https://microbenotes.com/electron-microscope-principle-types-components-applications-advantages-limitations/`.

[46] U.S. Department of Veterans Affairs. What Is an Electron Microscope (EM) and How Does It Work?, 2010. URL `https://www.va.gov/DIAGNOSTICEM/What_Is_Electron_Microscopy_and_How_Does_It_Work.asp`.

[47] Faith Mokobi and Sagar Aryal. Transmission Electron Microscope (TEM)-Definition, Principle, Images, 2022. URL `https://microbenotes.com/transmission-electron-microscope-tem/`.

[48] Manoj Rajankunte Mahadeshwara. Transmission electron microscopy, 2022. URL `https://www.tribonet.org/wiki/transmission-electron-microscopy/`.

[49] University of Warwick. Transmission Electron Microscopy (TEM). URL `https://warwick.ac.uk/fac/sci/physics/current/postgraduate/regs/mpagswarwick/ex5/techniques/structural/tem/`.

[50] David B. Williams and C. Barry Carter. *Transmission Electron Microscopy*. Springer US, Boston, MA, 2009. ISBN 978-0-387-76500-6. doi: 10.1007/978-0-387-76501-3. URL `http://link.springer.com/10.1007/978-0-387-76501-3`.

[51] nanoScience Instruments. Transmission Electron Microscopy, 2023. URL `https://www.nanoscience.com/techniques/transmission-electron-microscopy/`.

[52] Xiaoxing Ke, Carla Bittencourt, and Gustaaf Van Tendeloo. Possibilities and limitations of advanced transmission electron microscopy for carbon-based nanomaterials. *Beilstein Journal of Nanotechnology*, 6:1541–1557, jul 2015. ISSN 2190-4286. doi: 10.3762/bjnano.6.158. URL `https://www.beilstein-journals.org/bjnano/articles/6/158`.

[53] Yougui Liao. Damage of Materials due to Electron Irradiation. In *Practical Electron Microscopy and Database*. 2006. URL `https://www.globalsino.com/EM/page4543.html`.

[54] Yougui Liao. Low Dose TEM/STEM Imaging. In *Practical Electron Microscopy and Database*. 2006. URL `https://www.globalsino.com/EM/page1416.html`.

[55] ThermoFisher Scientific. Transmission Electron Microscopy vs Scanning Electron Microscopy, . URL `https://www.thermofisher.com/uk/en/home/materials-science/learning-center/applications/sem-tem-difference.html`.

[56] ThermoFisher Scientific. An Introduction to Electron Microscopy - TEM, . URL `https://www.fei.com/introduction-to-electron-microscopy/tem/#gsc.tab=0`.

[57] Yougui Liao. Objective Lens in TEMs/STEMs. In *Practical Electron Microscopy and Database*. 2 edition, 2006. URL `https://www.globalsino.com/EM/page3765.html`.

[58] Yougui Liao. Intermediate/Diffraction lens. In *Practical Electron Microscopy and Database*. 2 edition, 2006. URL `https://www.globalsino.com/EM/page1985.html`.

[59] JEOL Ltd. fluorescent screen. URL `https://www.jeol.com/words/emterms/20121023.023759.php#gsc.tab=0`.

[60] Yougui Liao. Viewing Screen/Fluorescent Screen. In *Practical Electron Microscopy and Database*. 2 edition, 2006. URL `https://www.globalsino.com/EM/page3247.html#:$\sim$:text=Thefluorescentscreenplatein,raysgeneratedintheTEM`.

[61] Yougui Liao. Charge-couple device (CCD). In *Practical Electron Microscopy and Database*. 2 edition, 2006. URL `https://www.globalsino.com/EM/page4909.html`.

[62] Bobby Gaston and Han Le. TEM: Bright field versus dark field, 2022. URL `https://chem.libretexts.org/Courses/Franklin_and_Marshall_College/Introduction_to_Materials_Characterization__CHM_412_Collaborative_Text/Electron_and_Probe_Microscopy/TEM%3A_Bright_field_versus_dark_field`.

[63] Yougui Liao. Bright-field (BF) Imaging in TEM. In *Practical Electron Microscopy and Database*. 2 edition, 2006. URL `https://www.globalsino.com/EM/page3358.html`.

[64] Yougui Liao. Dark-Field (DF) Imaging in TEM. In *Practical Electron Microscopy and Database*. 2 edition, 2006. URL `https://www.globalsino.com/EM/page3354.html`.

[65] Yougui Liao. Electron DIffraction. In *Practical Electron Microscopy and Database*. 2 edition, 2006. URL `https://www.globalsino.com/EM/page4107.html`.

[66] Yougui Liao. Power Spectra of Bright-field (BF) TEM Micrographs. In *Practical Electron Microscopy and Database*. 2 edition, 2006. URL `https://www.globalsino.com/EM/page4188.html`.

[67] ThermoFisher Scientific. An Introduction to Electron Microscopy - STEM, . URL `https://www.fei.com/introduction-to-electron-microscopy/stem/#gsc.tab=0`.

[68] nanoScience Instruments. Scanning Transmission Electron Microscopy, 2024. URL `https://www.nanoscience.com/techniques/scanning-transmission-electron-microscopy/#stem-v-tem`.

[69] Yougui Liao. Comparison between BF (Bright Field), ADF (Annular Dark Field) and HAADF (High Angle Annular Dark Field) STEM Images. In *Practical Electron Microscopy and Database*. 2 edition, 2006. URL `https://www.globalsino.com/EM/page4635.html`.

[70] Yougui Liao. Annular Dark-Field (ADF) Scanning Transmission Electron Microscopy (STEM). In *Practical Electron Microscopy and Database*. 2 edition, 2006. URL `https://www.globalsino.com/EM/page2799.html`.

[71] Yougui Liao. High-Angle Annular Dark-Field (HAADF) Imaging. In *Practical Electron Microscopy and Database*. 2 edition, 2006. URL `https://www.globalsino.com/EM/page3994.html`.

[72] Raghaw S. Rai and Swaminathan Subramanian. Role of transmission electron microscopy in the semiconductor industry for process development and failure analysis. *Progress in Crystal Growth and Characterization of Materials*, 55(3-4):63–97, sep 2009. ISSN 09608974. doi: 10.1016/j.pcrysgrow.2009.09.002. URL `https://linkinghub.elsevier.com/retrieve/pii/S0960897409000163`.

[73] Yougui Liao. Aberration and its Correction in STEM Mode. In *Practical Electron Microscopy and Database*. 2 edition, 2006. URL `https://www.globalsino.com/EM/page4111.html`.

[74] Yougui Liao. Advantages of EMs with Aberration Correctors. In *Practical Electron Microscopy and Database*. 2 edition, 2006. URL `https://www.globalsino.com/EM/page4382.html`.

[75] Yougui Liao. Quadrupole-Octupole Corrector for Cs Corrections. In *Practical Electron Microscopy and Database*. 2 edition, 2006. URL `https://www.globalsino.com/EM/page3653.html`.

[76] Toray Research Center Inc. spherical aberration corrected Scanning Transmission Electron Microscope:Cs-corrected STEM. URL `https://www.toray-research.co.jp/en/technicaldata/techniques/Cs_STEM.html`.

[77] JEOL. JEM-ARM200F ACCELARM Atomic Resolution Analytical Electron Microscope: Realizing an unprecedented STEM (HAADF) resolution of 0.08 nm. URL `https://www.jeol.com/products/scientific/tem/JEM-ARM200F_ACCELARM.php`.

[78] Crispin Hetherington. Aberration correction for TEM. *Materials Today*, 7(12): 50–55, dec 2004. ISSN 13697021. doi: 10.1016/S1369-7021(04)00571-1. URL `https://linkinghub.elsevier.com/retrieve/pii/S1369702104005711`.

[79] EAG Laboratories. A Picture is Worth a Thousand Words – TEM, STEM and AC-STEM.

[80] Advanced Imaging of Materials - Swansea University. FEI Talos F200X TEM. URL `https://www.swansea.ac.uk/engineering/aim/equipment/em/fei-talos/`.

[81] Johnson Matthey. JEOL ARM200CF High Resolution TEM (ePSIC), 2017. URL `https://www.diamond.ac.uk/industry/Techniques-Available/Physical-Sciences-Electron-Microscopy.html`.

[82] Diamond Light Source. electron Physical Science Imaging Centre (ePSIC). URL `https://www.diamond.ac.uk/Instruments/Imaging-and-Microscopy/ePSIC.html`.

[83] S. G. Hall, M. B. Nielsen, A. W. Robinson, and R. E. Palmer. Compact sputter source for deposition of small size-selected clusters. *Review of Scientific Instruments*, 1997. ISSN 00346748. doi: 10.1063/1.1148293.

[84] G. D. Alton. An axial geometry cesium sputter negative ion source with continuous tungsten surface ionizer. *Nuclear Inst. and Methods in Physics Research, A*, 244(1-2):133–141, 1986. ISSN 01689002. doi: 10.1016/0168-9002(86)90754-0.

[85] Mass Spec Pro. Einzel Lens. URL `http://www.massspecpro.com/technology/ion-optics/einzel-lens-0`.

[86] K. W. Leo, T. Adachi, T. Arai, and K. Takayama. Einzel lens chopper and behavior of the chopped beam in the kek digital accelerator. *Phys. Rev. ST Accel. Beams*, 16:043502, Apr 2013. doi: 10.1103/PhysRevSTAB.16.043502. URL `https://link.aps.org/doi/10.1103/PhysRevSTAB.16.043502`.

[87] Beam Imaging Solutions and Colutron Research Corporation. Model 600-B Velocity Filter User's Manual, 1997.

[88] D.I.S Germany GmbH. Tutorial Wien filter, 2025. URL `https://www.dis-eng.de/wp-content/uploads/sites/11133/2025/01/Tutorial_IBT-002-Wien_Filter.pdf`.

[89] Stefan Richtberg. Velocity-selector (Wien filter), 2021. URL https://virtuelle-experimente.de/en/b-feld/anwendung/geschwindigkeitsfilter.php.

[90] DREEBIT GmbH. Neutral Particle Beam Dump. URL https://www.dreebit.com/en/neutral-beam-dump.html.

[91] Matsusada Precision. Electrostatic Deflection. URL https://www.matsusada.com/application/ps/electrostatic_deflection_of_charged_particle_beams/.

[92] Dattaraj Vildyasagar. How deflection system in CRT work? Explain with diagram, 2024. URL https://vsa.edu.in/how-deflection-system-in-crt-work-explain-with-diagram/#:$\sim$:text=Inthissystem%2Ctheelectron,upofcopperoraluminium.

[93] Adaptas Solutions LLC. SIMION. URL https://simion.com.

[94] Alina Maria Holban, Alexandru Mihai Grumezescu, and Ecaterina Andronescu. Inorganic nanoarchitectonics designed for drug delivery and anti-infective surfaces. In *Surface Chemistry of Nanobiomaterials*, pages 301–327. Elsevier, 2016. doi: 10.1016/B978-0-323-42861-3.00010-8. URL https://linkinghub.elsevier.com/retrieve/pii/B9780323428613000108.

[95] History of Carbon nanotube. URL https://sites.google.com/site/nanomodern/Home/CNT.

[96] Sumio Iijima. Helical microtubules of graphitic carbon. *Nature*, 354(6348): 56–58, nov 1991. ISSN 0028-0836. doi: 10.1038/354056a0. URL http://www.nature.com/articles/354056a0.

[97] Maanoj Kumar Pradhan. Nano Science and Biotechnology, 2021. URL http://www.gcekjr.ac.in/pdf/lectures/2021/7373II_7thSemester_MineralEngineering.pdf.

[98] What-When-How. Carbon Nanotubes: Optical Properties Part 1 (Nanotechnology). URL http://what-when-how.com/nanoscience-and-nanotechnology/carbon-nanotubes-optical-properties-part-1-nanotechnology/.

[99] Vincent Teng. Carbon Nanotube Devices.

[100] M.S. Dresselhaus, Y.M. Lin, O. Rabin, A. Jorio, A.G. Souza Filho, M.A. Pimenta, R. Saito, G. Samsonidze, and G. Dresselhaus. Nanowires and

nanotubes. *Materials Science and Engineering: C*, 23(1-2):129–140, jan 2003. ISSN 09284931. doi: 10.1016/S0928-4931(02)00240-0. URL `https://linkinghub.elsevier.com/retrieve/pii/S0928493102002400`.

[101] Sudha Vengurlekar and Subhash Chandra Chaturvedi. Elevating toward a new innovation: Carbon nanotubes (CNTs). In *Biomedical Applications of Nanoparticles*, chapter 1.2 Multiw, pages 271–294. Elsevier, 2019. doi: 10.1016/B978-0-12-816506-5.00016-4. URL `https://linkinghub.elsevier.com/retrieve/pii/B9780128165065000164`.

[102] Philip G. Collins and Phaedon Avouris. Nanotubes for Electronics. *Scientific American*, 283(6):62–69, dec 2000. ISSN 0036-8733. doi: 10.1038/scientificamerican1200-62. URL `https://www.scientificamerican.com/article/nanotubes-for-electronics`.

[103] Michael Berger. Carbon nanotubes – what they are, how they are made, what they are used for. URL `https://www.nanowerk.com/nanotechnology/introduction/introduction_to_nanotechnology_22.php`.

[104] Alvin Orbaek White, Ali Hedayati, Tim Yick, Varun Shenoy Gangoli, Yubiao Niu, Sean Lethbridge, Ioannis Tsampanakis, Gemma Swan, Léo Pointeaux, Abigail Crane, Rhys Charles, Jainaba Sallah-Conteh, Andrew O. Anderson, Matthew Lloyd Davies, Stuart J. Corr, and Richard E. Palmer. On the use of carbon cables from plastic solvent combinations of polystyrene and toluene in carbon nanotube synthesis. *Nanomaterials*, 12(1):9, dec 2022. ISSN 20794991. doi: 10.3390/nano12010009. URL `https://www.mdpi.com/2079-4991/12/1/9`.

[105] Gibran Esquenazi, Bruce Brinson, and Andrew Barron. Catalytic Growth of Carbon Nanotubes by Direct Liquid Injection CVD Using the Nanocluster [HxPMo12O40âŠ‚H4Mo72Fe30(O2CMe)15O254(H2O)98-y(EtOH)y]. *C*, 4 (1):17, mar 2018. doi: 10.3390/c4010017.

[106] ImageJ Documentation Wiki. FFT, 2019. URL `https://imagejdocu.tudor.lu/gui/process/fft`.

[107] Alexei Matyushov, Zhengtang Luo, and A.T. Charlie Johnson. Growth of Carbon Nanotubes Via Chemical Vapor Deposition. Technical report.

[108] Nishant Tripathi, Prabhash Mishra, Harsh Harsh, and S. S. Islam. Fine-tuning control on CNT diameter distribution, length and density using thermal CVD growth at atmospheric pressure: an in-depth analysis on the role of flow rate

and flow duration of acetylene (C2H2) gas. *Applied Nanoscience*, 5(1):19–28, jan 2015. ISSN 2190-5509. doi: 10.1007/s13204-013-0288-8. URL `http://link.springer.com/10.1007/s13204-013-0288-8`.

[109] Ali Hedayati, Chris Barnett, Gemma Swan, and Alvin Orbaek White. Chemical Recycling of Consumer-Grade Black Plastic into Electrically Conductive Carbon Nanotubes. *C*, 5(2):32, jun 2019. ISSN 2311-5629. doi: 10.3390/c5020032. URL `https://www.mdpi.com/2311-5629/5/2/32`.

[110] Bruce Ratner. The Correlation Coefficient: Definition. URL `http://www.dmstat1.com/res/TheCorrelationCoefficientDefined.html`.

[111] Iraj Hasanzadeh and Mohammad Jafari Eskandari. Direct growth of multiwall carbon nanotube on metal catalyst by chemical vapor deposition: In situ nucleation. *Surface and Coatings Technology*, 381:125109, jan 2020. ISSN 02578972. doi: 10.1016/j.surfcoat.2019.125109. URL `https://linkinghub.elsevier.com/retrieve/pii/S0257897219311004`.

[112] Lizhao Liu, Feng Liu, and Jijun Zhao. Curved carbon nanotubes: From unique geometries to novel properties and peculiar applications. *Nano Research*, 7(5):626–657, may 2014. ISSN 1998-0124. doi: 10.1007/s12274-014-0431-1. URL `http://link.springer.com/10.1007/s12274-014-0431-1`.

[113] F. Schäffel, M. H. Rümmeli, C. Kramberger, U. Queitsch, E. Mohn, R. Kaltofen, T. Pichler, B. Büchner, B. Rellinghaus, and L. Schultz. Tailoring the diameter, density and number of walls of carbon nanotubes through predefined catalyst particles. *physica status solidi (a)*, 205(6):1382–1385, jun 2008. ISSN 18626300. doi: 10.1002/pssa.200778142. URL `https://onlinelibrary.wiley.com/doi/10.1002/pssa.200778142`.

[114] C.-H. Kiang, M. Endo, P. M. Ajayan, G. Dresselhaus, and M. S. Dresselhaus. Size Effects in Carbon Nanotubes. *Physical Review Letters*, 81(9):1869–1872, aug 1998. ISSN 0031-9007. doi: 10.1103/PhysRevLett.81.1869. URL `https://link.aps.org/doi/10.1103/PhysRevLett.81.1869`.

[115] Oxana V. Kharissova and Boris I. Kharisov. Variations of interlayer spacing in carbon nanotubes. *RSC Adv.*, 4(58):30807–30815, 2014. ISSN 2046-2069. doi: 10.1039/C4RA04201H. URL `http://xlink.rsc.org/?DOI=C4RA04201H`.

[116] Dilip K. Singh, P.K. Iyer, and P.K. Giri. Diameter dependence of interwall separation and strain in multiwalled carbon nanotubes probed by X-ray diffraction and Raman scattering studies. *Diamond and Related Materials*, 19(10):1281–1288, oct 2010. ISSN 09259635. doi: 10.1016/j.diamond.2010.06.

003. URL `https://linkinghub.elsevier.com/retrieve/pii/S0925963510002098`.

[117] Joachim Walter. FFT Filter, 2007. URL `https://imagej.nih.gov/ij/plugins/fft-filter.html`.

[118] ImageJ.net. Analyze Menu - Set Measurements. URL `https://imagej.nih.gov/ij/docs/menus/analyze.html`.

[119] N. P. Young, Z. Y. Li, Y. Chen, S. Palomba, M. Di Vece, and R. E. Palmer. Weighing Supported Nanoparticles: Size-Selected Clusters as Mass Standards in Nanometrology. *Physical Review Letters*, 101(24):246103, dec 2008. ISSN 0031-9007. doi: 10.1103/PhysRevLett.101.246103. URL `https://link.aps.org/doi/10.1103/PhysRevLett.101.246103`.

[120] Z. Y. Li, N. P. Young, M. Di Vece, S. Palomba, R. E. Palmer, A. L. Bleloch, B. C. Curley, R. L. Johnston, J. Jiang, and J. Yuan. Three-dimensional atomic-scale structure of size-selected gold nanoclusters. *Nature*, 451(7174):46–48, jan 2008. ISSN 0028-0836. doi: 10.1038/nature06470. URL `https://www.nature.com/articles/nature06470`.

[121] Rongsheng Cai, Francesca Martelli, Jerome Vernieres, Stefania Albonetti, Nikolaos Dimitratos, Chedly Tizaoui, and Richard E. Palmer. Scale-Up of Cluster Beam Deposition to the Gram Scale with the Matrix Assembly Cluster Source for Heterogeneous Catalysis (Catalytic Ozonation of Nitrophenol in Aqueous Solution). *ACS Applied Materials and Interfaces*, 12(22):24877–24882, jun 2020. ISSN 1944-8244. doi: 10.1021/acsami.0c05955. URL `https://pubs.acs.org/doi/10.1021/acsami.0c05955`.

[122] Erica Watchorn-Rokutan. *Investigating the use of gas sensors for breath analysis to detect diseases using cluster-decorated printed graphene*. PhD thesis, Swansea University, 2020.

[123] C. Mottet, J. Goniakowski, F. Baletto, R. Ferrando, and G. Treglia. Modeling free and supported metallic nanoclusters: structure and dynamics. *Phase Transitions*, 77(1-2):101–113, jan 2004. ISSN 0141-1594. doi: 10.1080/1411590310001622473. URL `http://www.tandfonline.com/doi/abs/10.1080/1411590310001622473`.

[124] David Loffreda, Dawn M. Foster, Richard E. Palmer, and Nathalie Tarrat. Importance of Defective and Nonsymmetric Structures in Silver Nanoparticles. *The Journal of Physical Chemistry Letters*, 12(15):3705–3711, apr 2021. ISSN

1948-7185. doi: 10.1021/acs.jpclett.1c00259. URL `https://pubs.acs.org/doi/10.1021/acs.jpclett.1c00259`.

[125] Jerome Vernieres, Nathalie Tarrat, Sean Lethbridge, Erica Watchorn-Rokutan, Thomas Slater, David Loffreda, and Richard E. Palmer. Influence of air exposure on structural isomers of silver nanoparticles. *Communications Chemistry*, 6(1):19, jan 2023. ISSN 2399-3669. doi: 10.1038/s42004-023-00813-9. URL `https://www.nature.com/articles/s42004-023-00813-9`.

[126] V. T. A. Oiko, T. Mathieu, L. Cao, J. Liu, and R. E. Palmer. Note: Production of silver nanoclusters using a Matrix-Assembly Cluster Source with a solid CO 2 matrix. *The Journal of Chemical Physics*, 145(16):166101, oct 2016. ISSN 0021-9606. doi: 10.1063/1.4966213. URL `http://aip.scitation.org/doi/10.1063/1.4966213`.

[127] G. Federici, V. Barabash, R. Doerner, P. Lorenzetto, G. Matthews, and A.R. Raffray. Beryllium as a Plasma Facing Material for Near-Term Fusion Devices. In *Reference Module in Materials Science and Materials Engineering*. Elsevier, 2016. doi: 10.1016/B978-0-12-803581-8.09805-2. URL `https://linkinghub.elsevier.com/retrieve/pii/B9780128035818098052`.

[128] K. Oura, M. Katayama, A. V. Zotov, V. G. Lifshits, and A. A. Saranin. Elementary Processes at Surfaces II. Surface Diffusion. pages 325–356. 2003. doi: 10.1007/978-3-662-05179-5_13. URL `http://link.springer.com/10.1007/978-3-662-05179-5_13`.

[129] Evgeny Shustorovich. *Metal-surface reaction energetics : theory and applications to heterogeneous catalysis, chemisorption, and surface diffusion*. Wiley, 1991.

[130] Z. W. Wang and R. E. Palmer. Direct atomic imaging and dynamical fluctuations of the tetrahedral Au20 cluster. *Nanoscale*, 4(16):4947, 2012. ISSN 2040-3364. doi: 10.1039/c2nr31071f. URL `https://xlink.rsc.org/?DOI=c2nr31071f`.

[131] Z.W. Wang and R. E. Palmer. Experimental Evidence for Fluctuating, Chiral-Type Au 55 Clusters by Direct Atomic Imaging. *Nano Letters*, 12(11):5510–5514, nov 2012. ISSN 1530-6984. doi: 10.1021/nl303429z. URL `https://pubs.acs.org/doi/10.1021/nl303429z`.

[132] Sean Lethbridge, Theodoros Pavloudis, James McCormack, Thomas Slater, Joseph Kioseoglou, and Richard E. Palmer. Stabilization of 2D Raft Structures of Au Nanoclusters with up to 60 Atoms by a Carbon Support. *Small Science*,

4(8), aug 2024. ISSN 2688-4046. doi: 10.1002/smsc.202400093. URL `https://onlinelibrary.wiley.com/doi/10.1002/smsc.202400093`.

[133] D. M. Foster, R. Ferrando, and R. E. Palmer. Experimental determination of the energy difference between competing isomers of deposited, size-selected gold nanoclusters. *Nature Communications*, 9(1), dec 2018. ISSN 20411723. doi: 10.1038/s41467-018-03794-9.

APPENDIX A

A.1 Optimisation of Size and Structure Analysis Process

In the beginning, the size and structure approximation process was performed manually with each particle and cluster being analysed individually. In the context of single atoms, this therefore limited the sample size for single atom intensity determination. Fortunately, the image processing software used possessed the ability to write and record macros. This in combination with a pre-existing base script allowed for the development of macros which could perform size and structure analysis at a much faster pace. The development and evolution of these macros will be described below.

A.1.1 Development of Fiji/ImageJ Macros

Numerous macros were developed over time to expedite the process of analysing HAADF-STEM images of nanoclusters and extract new information. The new macros produced in this thesis however, are based on a pre-existing macro *"Cluster intensity.ijm"* created by previous student *Erica Watchorn-Rokutan* and is demonstrated in Appendix A.1. In this existing macro, the purpose is to highlight particles in the image through thresholds and then return the particle and background intensity values using the same methodology as described in Section 5.1.1. Due to the nature of the size and structure analysis being undertaken in this thesis however, it became necessary to modify and expand on this existing base script to suit the data requirements needed. An illustration of the macro evolution is shown below in Figure A.1 with a summary of the modifications shown in Table A.1.

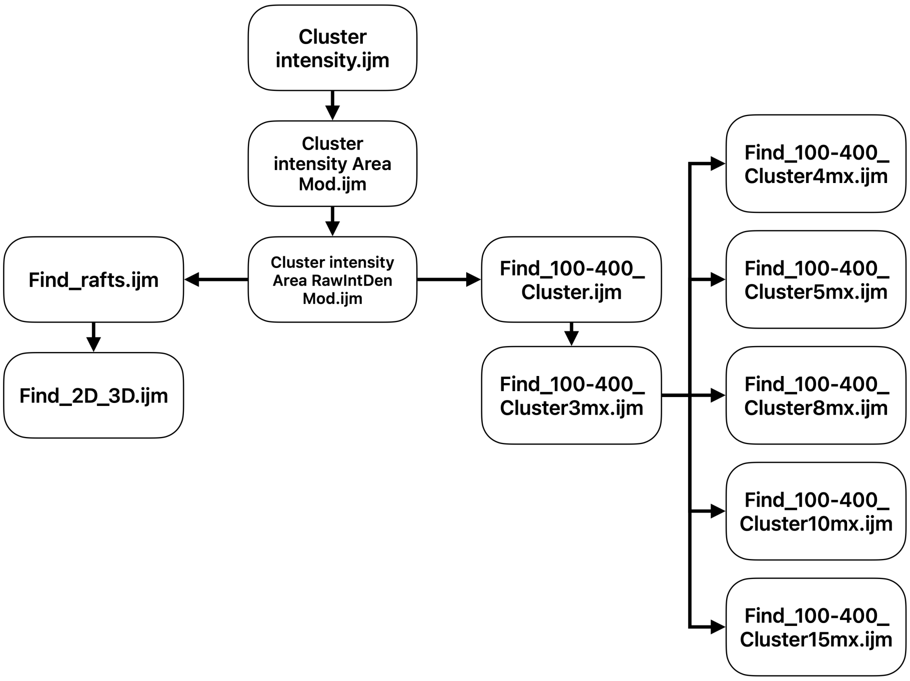

Figure A.1: Flowchart describing the evolution of ImageJ/Fiji macros to optimise the size and structure determination process for nanocluster's.

Table A.1: Summary of the modifications applied to the ImageJ/Fiji macros as they are developed.

Macro Filename	**Modification/Addition**
Cluster intensity.ijm	None - Base code.
Cluster intensity Area Mod.ijm	Line added to print particle area (nm) in results.
Cluster intensity Area RawIntDen Mod.ijm	Code modified to use Raw Integrated Density instead of mean value in intensity calculations. Peak intensity value added as a result variable.
Find_100-400_Cluster.ijm	Code modified to filter for spherical Ag clusters of specific sizes (Template code for expansion). Peak finding removed.
Find_100-400_Cluster3mx.ijm	Code modified to highlight only spherical Ag clusters between certain sizes corresponding to 3Mx magnification. Cluster intensity calculation and printing removed.
Find_100-400_Cluster4mx.ijm	Code modified for sizes corresponding to 4Mx magnification.
Find_100-400_Cluster5mx.ijm	Code modified for sizes corresponding to 5Mx magnification.
Find_100-400_Cluster8mx.ijm	Code modified for sizes corresponding to 8Mx magnification.
Find_100-400_Cluster10mx.ijm	Code modified for sizes corresponding to 10Mx magnification.
Find_100-400_Cluster15mx.ijm	Code modified for sizes corresponding to 15Mx magnification.
Find_rafts.ijm	Code modified to use existing data to analyse particles in images to determine the approximate number of layers and hence whether particles are 'Rafts' or 'Clusters'. Additionally, code added to save image of highlighted particles as png.
Find_2D_3D.ijm	Code modified to only print results of particles of size between 1 and 100 atoms.

Cluster intensity Area Mod

In the first adaptation of the base code, the purpose was to modify the code to simply include an extra parameter in the printed results. This was the area of the inner bounding circle recorded in pixels. As the number of pixels within the bounding circles is an automatically recorded variable, it was therefore only necessary to add a single line of code: *setResult("Area (px)", i, nPixels1);*. In this "Area (px)" represents the new result title, "i" represents the index number of the bounding circle, and "nPixels1" represents the pixel count for that bounding circle. The addition of this variable was essential in filtering out potential single atoms from the full list of particles returned in results, where single atom segregation bounds we established as previous described. The use of this macro with its added result allowed for the analysis of potential single atom like particles in a matter of minutes with a significantly larger sample size increasing reliability in single atom intensity determination.

Cluster intensity Area RawIntDen Mod

In the second adaptation of the base code, the previous code is modified to use the *Raw Intengrated Density (RawIntDen)* value in the intensity calculations, instead of the *Mean* value. The purpose of this is to improve the accuracy of the final particle intensity estimation where the *Raw Intengrated Density* is a more precise value. Unlike the previous version, the RawIntDen is not an automatically recorded value and hence it was therefore necessary to add the following code to retrieve the value for the area being measured: *getValue("RawIntDen")*. This code was used in two locations, the calculation of the inner and outer bounding circle statistics, and were set as the variables *Raw1* and *Raw2* respectively. The existing intensity calculation code was then modified to use new RawIntDen variables instead of the existing mean value variables. In addition, a further variable was added to the result output to print the maximum pixel intensity value measured in the inner bounding circle, this was done using the same principle as previously described for the "Area" modification. The use of this macro allowed for a more accurate determination of single atom intensity which in turn allowed more a more precise estimation of the number of atoms in measured clusters.

Find_ 100-400_ Cluster

In this version of the base code, the *Cluster intensity Area RawIntDen Mod* script is further modified to measure the average diameter of clusters and use this to only analyse those particles with diameters within values corresponding to clusters of sizes 100 to 400 atoms. The diameter is estimated using the sum of the inner bounding circles width and height divided by 2. In this script the minimum and maximum sizes are calculated from Equations (5.11) and (5.12) respectively multiplied by the corresponding image scale. From this the macro would then return only clusters within these sizes significantly minimising analysis time where the objective was to focus on clusters within 100 and 400 atoms in size. This code was not intended for use in analysis but instead act as a template for further additional macros tailored for specific image magnifications.

Find_ 100-400_ ClusterXXmx

In the magnification specific versions of the *Find_ 100-400_ Cluster* macro further modifications are applied to not only tailor the script to the magnification being investigated but also simplify the outputs of the script. This include the addition of a variable where the calculated average diameter is outputted as a results parameter, the fixing of the minimum and maximum size values corresponding to the magnification of the image as shown in Table A.2, and removal of the cluster intensity calculations and corresponding results parameters. The final result of which is a magnification specific script designed to highlight clusters with sizes corresponding to those of 100 to 400 atom particles. This could then be used with previous analysis to add further statistics such as atom numbers and isomer structures. Due the method employed in this script, it was designed to work only with the Ag samples analysed in this thesis.

Table A.2: 100-400 atom sized cluster diameters in pixels scaled according to image magnification.

Magnification	**Scale (px/nm)**	**Minimum Diameter**	**Maximum Diameter**
3 Mx	15.9226	23.56	47.16
4 Mx	21.1621	31.32	62.68
5 Mx	26.3681	39.02	78.10
8 Mx	42.2521	62.53	125.15
10 Mx	52.8678	78.24	156.59
15 Mx	79.5001	117.66	235.47

Find_ rafts

In the *Find_ rafts* iteration of the base code, the *Cluster intensity Area RawIntDen Mod* script is altered to use existing analysis to highlight monolayer raft like structures in HAADF-STEM images. These alterations include the extraction of the image magnification through the *getInfo()* command and using this in a look-up table to extract the correct image scale in pixels/nanometre. Furthermore, the *getNumber()* command is used to record the single atom intensity obtained from previous analysis. This is then used in the existing script code to estimate the number of atoms through division of the calculated cluster intensity by the obtained single atom intensity. Using this and existing data further parameters are then calculated including the area in nanometres, equivalent circular diameter, and number of layers, as shown below in Equations (A.1) to (A.3).

$$Area\ (nm) = \frac{Area\ (px)}{Scale\ (px/nm)^2} \tag{A.1}$$

$$Equivalent\ Circular\ Diameter = \sqrt{\frac{Area\ (nm)}{\pi}} \tag{A.2}$$

$$Number\ of\ Layers = \frac{(\frac{(0.017 \times Number\ of\ Atoms}{\pi \times Equivalent\ Circular\ Diameter^2})}{0.34} \tag{A.3}$$

The outputs of this analysis are then further categorised as either *Rafts* or *Clusters* where a raft is any structure with a number of atoms greater than *10* and number of layers between *0.75* and *1.5*, and a cluster is any structure not meeting all three conditions. The resulting script enables the quick differentiation of rafts and clusters in obtained HAADF-STEM images.

Find_ 2D_ 3D

The final iteration of the base code is a further evolution of the *Find_ rafts* script where the criteria for the size of a raft is modified to limit them to structures under *100* atoms in size. Any structure either greater than *100* atoms in size or having a layer count larger than *1.5*, is categorised as a cluster. Through the use of multiple *if* statements, it became possible to further hastily filter out raft like structures between *1* and *100* atoms where this size range was of particular interest.

A.2 Initial Cluster Intensity Code (Erica Watchorn-Rokutan)

```
run("Set Scale...", "distance=0 known=0 pixel=1 unit=pixel
   ");
getRawStatistics(nPixels, mean, min, max, std, histogram);

originalTitle = getTitle();
run("32-bit");
run("Duplicate...", "title=Original.dm3");
run("Duplicate...", "title=WorkingCopy.dm3");
run("Duplicate...", "title=Filtered1");

b = 50;

selectWindow("Filtered1");
run("Median...", "radius=" +b);
run("Image Calculator...", "image1=WorkingCopy.dm3
   operation=Subtract image2=Filtered1 create");
run("Rename...", "title=Result1");

//New additions
run("Median...", "raius=" +1);
run("Median...", "raius=" +4);

// THresholds to identify clusters.

//setAutoThreshold("MaxEntropy"); //Best
//setAutoThreshold("Mean");
//setAutoThreshold("Minimum");
//setAutoThreshold("Moments");
//setAutoThreshold("Intermodes");
//setAutoThreshold("IsoData");
//setAutoThreshold("MinError");
//does a errode then a dilate to remove some of the noise.
//run("Make Binary");
//run("Close-");
//run("Invert");

// Or manually set threshold

run("Threshold...");
wait(40000);
Dialog.create("Threshold set");
Dialog.show();
run("Make Binary");

// options box for cluster size
macro "Find Clusters [y]"
{
```

```
//"Number smaller than distance between closest two
    clusters but larger than cluster diameter (
   pixels)", 2);
n=2;

// expands cluster areas
run("Options...", "iterations="+n+" count=1 pad edm
   =Overwrite do=Nothing");
run("Dilate");
run("Options...", "iterations=1 count=1 pad edm=
   Overwrite do=Nothing");

run("Clear Results");

// anslyses partciles to find the centre and the
   width and height
run("Set Measurements...", "  centroid bounding
   redirect=None decimal=3");
run("Analyze Particles...", "size=0-Infinity
   circularity=0.00-1.00 show=Nothing display
   exclude");
close();

//selectWindow(originalTitle);
selectWindow("Original.dm3");
W1=1; H1=1;

wait(5000);
// gets the width height and position of each
   cluster and saves them as W,H X and Y making a
   set point for X and Y
for (i=0; i<nResults; i++)
{
        W = getResult("Width", i);
        H = getResult("Height", i);

        //if (W>W1)
        //{
        //      W1=W;
        //}

        //if (H>H1)
        //{
        //      H1=H;
        //}

        // calculates the radius of the inner and
           outer circle. largest of height or width

        if (H>W)
        {
```

```
        r=H/2;
}
else
{
        r=(W/2);
}
ri=r+1;
ro=ri+3;

x = getResult("X", i);
y = getResult("Y", i);
setResult("Ri", i, ri);
setResult("Ro", i, ro);

setKeyDown("shift");
makePoint(x,y);

//Inner Circle
makeOval(x-ri, y-ri, 2*ri, 2*ri);
getRawStatistics(nPixels1, mean1, min1,
   max1, std1, histogram1);

//Outer Circle
makeOval(x-ro, y-ro, 2*ro, 2*ro);
getRawStatistics(nPixels2, mean2, min2,
   max2, std2, histogram2);

//Total intensity of whole Large Area
TA2=nPixels2*mean2;

//Total intensity of Small Area
TA1=nPixels1*mean1;

//Total carbon intensity
Carbon_Anulus_Intensity= TA2-TA1;

//number of carbon pixels
nPixC= nPixels2-nPixels1;

//background intensity per pixel
Background_Pixel_Intensity=
   Carbon_Anulus_Intensity/nPixC;

//total intensity (inner circle) minus
   background
Cluster_Intensity= TA1-(
   Background_Pixel_Intensity*nPixels1);

//total background
//TB=BackgroundCmean*nPixels2;
```

```
                //Result printing
                setResult("Cluster", i, Cluster_Intensity);
                setResult("Background", i,
                   Background_Pixel_Intensity);
                //print(f,originalTitle+"\t"+i+1+"\t"+x1+"\
                   t"+y1+"\t"+BackgroundCmean+"\t"+TA1Bsub)
                   ;
                //PtandTi[i]=TA1Bsub;
                //BackPerPix[i]=BackgroundCmean;
                //draw circles and number them
                setForegroundColor(255, 255, 255);
                setFont("SansSerif", 12, "bold");
                drawString(i+1, x+ri/2, y-ri/2);
                drawOval(x-ri, y-ri, 2*ri, 2*ri);
                drawOval(x-ro, y-ro, 2*ro, 2*ro);
        }

updateResults();
}
```